ATLAS CONF Note

ATLAS-CONF-2020-053

28th October 2020

Interpretations of the combined measurement of Higgs boson production and decay

The ATLAS Collaboration

First combined measurements of the Higgs boson production and decay using up to 139 fb^{-1} of proton–proton collision data at $\sqrt{s}$ = 13 TeV recorded by the ATLAS experiment have recently been performed. This note presents two interpretations of these combined Higgs boson measurements. Measurements targeting Simplified Template Cross Sections in different decay channels are reparameterized in terms of the impact of Standard Model Effective Field Theory (SMEFT) operators and constraints are reported on the corresponding Wilson coefficients. Measurements are furthermore interpreted in several MSSM benchmark scenarios, resulting in constraints on the MSSM parameters $(m_A, \tan\beta)$ that are complementary to those obtained from direct searches for additional Higgs bosons. For all interpretations, no significant deviations from the Standard Model are observed.

1 Introduction

Following the discovery of the Higgs boson (H) [1–6] by the ATLAS [7] and CMS [8] experiments, its properties have been probed in proton–proton (pp) collision data produced by the Large Hadron Collider (LHC) at CERN. The ATLAS collaboration recently presented first results on the combination of Higgs boson production and decay rate measurements with up to 139 fb^{-1} of 13 TeV pp collision data [9], collected during LHC Run 2 in the years 2015 through 2018.

Two interpretations of these measurements are presented here, based on an Effective Field Theory (EFT) framework of the Standard Model (SM), as well as a minimal supersymmetric extension of the Standard Model (MSSM).

Effective field theories provide a model-independent approach, systematically improvable with higher-order perturbative calculations, to parametrise the effects of candidate theories beyond the Standard Model (BSM) that reduce to the Standard Model at low energies. In SM Effective Field Theory (SMEFT), the effects of BSM dynamics at energy scales Λ that are large in comparison to the Higgs vacuum-expectation-value v ($\Lambda \gg v$) can be parametrised at low energies, $E \ll \Lambda$, in terms of higher-dimensional operators built up from the Standard Model fields and respecting its symmetries. Measurements of (fiducial) cross-sections allow constraining of the coefficients associated to each SMEFT operator, and hence put constraints on new physics at some fixed scale Λ, for which $\Lambda = 1$ TeV is used throughout this note. The methodology employed here is quite similar to the one used by the individual Higgs analyses, especially $H \to ZZ^* \to 4\ell$ ($\ell = e$ or μ) [10] and $H \to b\bar{b}$ (VH, $V = W$ or Z) [11, 12]. A similar combined measurement has previously been performed on a subset of the data [13], but the measurement technique has been significantly developed in Ref. [14]. Its application to the combined measurements of the $H \to b\bar{b}$ (VH), $H \to ZZ^* \to 4\ell$ and $H \to \gamma\gamma$ channels comes with specific challenges, linked to the search of the set of operators that can be effectively probed in the combination, which can be different from the union of operators probed by each of the individual analyses, due to different correlations between production and decay of these channels.

Conversely, in the MSSM approach a combination of Higgs boson measurements in various decay channels is used, including besides $H \to b\bar{b}$ (VH) [11], $H \to ZZ^* \to 4\ell$ [10] and $H \to \gamma\gamma$ [15], vector-boson-fusion production of $H \to b\bar{b}$ (VBF) [16] and $H \to b\bar{b}$ ($t\bar{t}H$) [17], as well as $H \to WW^*$ [18], $H \to \tau\tau$ [19], $H \to$ multilepton ($t\bar{t}H$) [20], and $H \to \mu\mu$ [21]. These measurements are interpreted in a model-dependent way, assuming that the observed Higgs boson is the light CP-even Higgs boson of the minimal supersymmetric extension of the Standard Model. In the past years, measurements were interpreted [22] in the hMSSM model [23], for various values of the mass of the neutral CP-odd boson A (m_A), and the ratio of the vacuum expectation values of the Higgs doublets ($\tan\beta \equiv v_2/v_1$). The use of this model as a benchmark MSSM scenario to study constraints in the ($M_A, \tan\beta$)-plane suffers from limitations in regions with small M_A, or large $\tan\beta$, or both low M_A and low $\tan\beta$. Here, six more recent benchmark MSSM scenarios [24, 25] are tested, including two that were especially designed for the low $\tan\beta$ (<10) regime.

The note is structured as follows: Section 2 gives an overview of the combined Higgs couplings analysis that is used as a baseline to derive the results presented. Section 3 describes the general approach of deriving limits on Wilson coefficients, while Section 4 details the specific choices of Wilson coefficients and their combinations probed in this analysis as well as the corresponding results. Similarly, Section 5 describes the approach taken to interpret the Higgs coupling measurements in the context of the MSSM, while Section 6 presents the resulting limits in the ($M_A, \tan\beta$)-plane. Finally, Section 7 presents the conclusions.

2 Combined measurement of Higgs boson production and decay

The results of this note are based on pp collision data collected by the ATLAS experiment[1] [26–28] in the years from 2015 to 2018, with the LHC operating at a center-of-mass energy of 13 TeV. The decay channels, targeted production modes and integrated luminosities of the datasets used in each analysis are summarized in Table 1. The uncertainty on the combined 2015–2018 integrated luminosity is 1.7% [29], obtained using the LUCID-2 detector [30] for the primary luminosity measurements.

Table 1: The decay channels, targeted production modes and integrated luminosity ($\mathcal{L}$) used for each input analysis of the combination. The references for the input analyses and information about which measurements they enter are also provided. The definition of the STXS stage of the signal yield parametrization is detailed in Section 2.2.

Analysis		Integrated lumi (fb^{-1})	Reference	STXS stage	Used in MSSM	Used in EFT
$H \to \gamma\gamma$	(all production modes)	139	[15]	1.2	✓	✓
$H \to ZZ^* \to 4\ell$	(all production modes)	139	[10]	1.2	✓	✓
$H \to b\bar{b}$	(VH)	139	[11]	1.2	✓	✓
$H \to WW^*$	(ggH, VBF)	36.1	[18]	1.0	✓	-
$H \to \tau\tau$	(ggH, VBF)	36.1	[19]	1.0	✓	-
$H \to b\bar{b}$	(VBF)	24.5 – 30.6	[16]	0	✓	-
$H \to b\bar{b}$	($t\bar{t}H$)	36.1	[17]	0	✓	-
$H \to$ multilepton	($t\bar{t}H$)	36.1	[20]	0	✓	-
$H \to \mu\mu$	(all production modes)	139	[21]	0	✓	-

2.1 Simulation of the Standard Model signal

For each Higgs boson decay mode, the used branching fraction corresponds to theoretical calculations at the highest available order [31].

All analyses except $H \to b\bar{b}$ (VBF) use a consistent set of Higgs boson signal samples which is described in the following paragraphs. The samples used for $H \to b\bar{b}$ (VBF) are described separately at the end of this section.

Higgs boson production via gluon-gluon fusion (ggH) is simulated using the Powheg Box [32–35] NNLOPS implementation [36, 37]. The event generator uses HNNLO [38] to reweight the inclusive Higgs boson rapidity distribution produced by the next-to-leading order (NLO) generation of $pp \to H +$ parton, with the scale of each parton emission determined using the MiNLO procedure [39]. The PDF4LHC15 parton distribution functions (PDFs) are used for the central prediction and uncertainty. The sample is normalized such that it reproduces the total cross section predicted by a next-to-next-to-next-to-leading-order (N^{3}LO) QCD calculation with NLO electroweak corrections applied [31, 40–43]. The NNLOPS

[1] ATLAS uses a right-handed coordinate system with its origin at the nominal interaction point (IP) in the center of the detector and the z-axis along the beam pipe. The x-axis points from the IP to the center of the LHC ring, and the y-axis points upwards. Cylindrical coordinates (r, ϕ) are used in the transverse plane, ϕ being the azimuthal angle around the z-axis. The pseudorapidity is defined in terms of the polar angle θ as $\eta = -\ln\tan(\theta/2)$. Angular distance is measured in units of $\Delta R \equiv \sqrt{(\Delta\eta)^2 + (\Delta\phi)^2}$.

generator reproduces the Higgs boson p_T distribution predicted by the NNLO plus next-to-next-to-leading logarithm (NNLL) calculation of Hres2.3 [44], which includes the effects of top- and bottom-quark masses and uses dynamical renormalization and factorization scales.

The VBF and VH production processes are simulated at NLO accuracy in QCD using the Powheg Box [45] generator with the PDF4LHC15 set of PDFs, where the simulation of VH relies on improved NLO calculations [46]. The VBF sample is normalized to an approximate-NNLO QCD cross section with NLO electroweak corrections applied [31, 47–49]. The VH samples are normalized to cross sections calculated at NNLO in QCD with NLO electroweak corrections [50, 51] and additional NLO QCD corrections [52] for the $gg \to ZH$ subprocess [31].

Higgs boson production in association with a top–antitop pair is simulated at NLO accuracy in QCD using the Powheg Box generator with the PDF4LHC15 set of PDFs for the $H \to \gamma\gamma$ and $H \to ZZ^* \to 4\ell$ decay processes. For other Higgs boson decays, the MadGraph5_aMC@NLO [53] generator is used with the NNPDF3.0 set of PDFs. In both cases the sample is normalized to a calculation with NLO QCD and electroweak corrections [31, 54–57].

In addition to the primary Higgs boson processes, separate samples are used to model lower-rate processes. For the 36 fb^{-1} analyses, Higgs boson production in association with a bottom–antibottom pair ($b\bar{b}H$) is simulated using MadGraph5_aMC@NLO [58] with NNPDF2.3LO PDFs and is normalized to a cross section calculated to NNLO in QCD [31, 59–61]. The sample includes the effect of interference with the ggH production mechanism. Higgs boson production in association with a single top quark and a W boson (tHW) is produced at LO accuracy using MadGraph5_aMC@NLO. Finally, Higgs boson production in association with a single top quark in the t-channel (tHq) is generated at LO accuracy using MadGraph5_aMC@NLO with CT10 [62] PDF sets. The tH samples are normalized to NLO QCD calculations [31, 63]. For the 139 fb^{-1} analyses, the PDF used for the $b\bar{b}H$ sample is CT10, and the single top associated samples are produced at NLO accuracy in QCD using the NNPDF3.0NLO PDF set.

In the all-hadronic channel of the $H \to b\bar{b}$ (VBF) analysis, the Powheg Box generator with the CT10 [62] set of PDFs is used to simulate the ggH and VBF production processes, and interfaced with Pythia8 for parton shower. In the photon channel of the $H \to b\bar{b}$ (VBF) analysis, VBF and ggH production in association with a photon is simulated using the MadGraph5_aMC@NLO generator with the PDF4LHC15 set of PDFs, and also using the Pythia8 generator for the parton shower. For both channels, contributions from VH and $t\bar{t}H$ production are generated with Pythia8 generator with the NNPDF3.0 set of PDFs, and with MadGraph5_aMC@NLO showered with Herwig++ and using the NLO CT10 PDF, respectively.

All parton-level events are input to Pythia8 [64] to model the Higgs boson decay, parton showering, hadronization, and multiple parton interactions (MPI). The generators are interfaced to Pythia8, using the AZNLO and A14 parameter sets [65].

Particle-level events were passed through a Geant 4 [66] simulation of the ATLAS detector [67] and reconstructed using the same analysis software as used for the data. Event pileup is included in the simulation by overlaying inelastic pp collisions, such that the average number of interactions per bunch crossing reproduces that observed in the data. The inelastic pp collisions were simulated with Pythia8 using the MSTW2008lo [68] set of PDFs with the A2 [69] set of tuned parameters or using the NNPDF2.3LO set of PDFs with the A3 [70] set of tuned parameters.

2.2 Signal yield parametrization

In all analyses listed in Table 1, the estimated contributions to the Higgs boson signal yield are separately parametrized for every contributing permutation of Higgs boson production/decay mode, i.e. the likelihood for each analysis region k is modeled as

$$L(N_k|\mu^{i,X},\boldsymbol{\theta}) = \text{Poisson}\left(N_k|s_k(\mu^{i,X},\boldsymbol{\theta}) + b_k(\boldsymbol{\theta})\right) \tag{1}$$

$$s_k(\mu^{i,X},\boldsymbol{\theta}) = \sum_{i,X} \mu^{i,X} \times \mathcal{L} \times (\sigma \times B)^{i,X}_{\text{SM,MC}}(\boldsymbol{\theta}) \times \epsilon^{i,X}_k(\boldsymbol{\theta}), \tag{2}$$

where N_k is the observed event count, s_k is the expected signal count, $\mathcal{L}$ is the integrated luminosity, $\mu^{i,X}$ is a scale parameter for the SM Higgs boson signal $(\sigma \times B)^{i,X}_{\text{SM,MC}}$ used in the MC simulation with the indices i and X enumerating the considered production and decay modes. Furthermore, $\epsilon^{i,X}_k$ represents the corresponding acceptances times efficiency, b_k represents the expected event count from background processes, and $\boldsymbol{\theta}$ represents the ensemble of nuisance parameters that describe the systematic uncertainties that originate from theoretical and experimental sources. Unlike the cross-section results presented in Ref. [9], which only account for signal theory uncertainties in migration effects that occur at the reconstruction level through the term $\epsilon^{i,X}(\boldsymbol{\theta})$, the scale factor formulation of Eq. (2) used here also accounts for the effect of theory uncertainties on the inclusive signal cross-section via the term $(\sigma \times B)^{i,X}_{\text{SM,MC}}(\boldsymbol{\theta})$. For the analysis presented here, the scale factor $\mu^{i,X}$ is factorized as

$$\mu^{i,X} = \frac{\sigma^i \times B^{H\to X}}{(\sigma \times B)^{i,X}_{\text{SM,MC}}}, \tag{3}$$

where σ^i and $B^{H\to X}$ represent Higgs boson production cross sections and branching fractions respectively. The Higgs boson production cross sections σ^i are parameterized at a minimum granularity of inclusive production rates, labeled by LO process (i=ggH, VBF, . . .). A more fine-grained definition of Higgs boson production cross sections additionally partitioned in particle-level kinematic regions, e.g. in bins of p_T^{H}, allow the ensemble of parameters σ^i to describe deviations in differential distributions, with the level of detail controlled by the number of particle-level regions i that are defined. Conversely, the precision with which this more fine-grained ensemble of parameters σ^i can be measured depends on the design of the analysis as well as the amount of available data. Analysis regions k, defined at the reconstruction level, are typically chosen to match the particle-level regions i as closely as possible, in order to reduce the extrapolation uncertainty. As reconstruction-level selections do generally not correspond exactly to particle level regions, multiple particle-level regions i will contribute to the signal yield s_k of Eq. (2).

For an interpretation of the measured Higgs boson data in a particular physics model (SMEFT, MSSM) with parameters $\boldsymbol{\alpha}$, the original model parameters σ^i and $B^{H\to X}$ are replaced with functional expressions that parameterize the predictions of the model, $\sigma^i(\boldsymbol{\alpha})$ and $B^{H\to X}(\boldsymbol{\alpha})$, so that the likelihood of Eq. (1) is directly expressed in the parameters $\boldsymbol{\alpha}$, and constraints on these parameters can be directly inferred from the modified likelihood expression. While the original parameters σ^i no longer appear in the reparameterized expression, the granularity of the definition of the regions that defined σ^i will continue to be a relevant factor in the achievable level of detail in the parameterization in $\boldsymbol{\alpha}$.

For the analyses presented here, regions in Higgs boson production phase space known as simplified template cross sections [31, 71–73] (STXS) are used. STXS regions are defined in terms of the kinematics of the Higgs boson and, when they are present, of associated jets and W and Z bosons, independently of the Higgs boson decay process. Partitions are chosen according to three criteria: sensitivity to deviations from the SM expectation, avoidance of large theory uncertainties in the corresponding SM predictions, and approximately matching experimental selections so as to minimize model-dependent extrapolations with respect to e.g. the acceptance factor of the STXS bins. All STXS regions are defined for a Higgs boson rapidity y_H satisfying $|y_H| < 2.5$, corresponding approximately to the region of experimental sensitivity. Jets are reconstructed from all stable particles with an average lifetime greater than 10 ps, excluding the decay products of the Higgs boson and leptons from W and Z boson decays, using the anti-k_t algorithm with a jet radius parameter $R = 0.4$, and must have a transverse momentum $p_{\mathrm{T,jet}} > 30$ GeV. Higgs boson production is first classified according to the nature of the initial state and the associated particles, the latter including the decay products of the W and Z bosons if they are present. These classes are: $t\bar{t}H$ and tH processes; $qq \to Hqq$ processes, with contributions from both VBF production and quark-initiated VH production with a hadronic decay of the gauge boson; VH production with a leptonic decay of the vector boson (V(lep)H), including $gg \to ZH$ production; and finally the ggH process. The last process is considered together with $gg \to ZH$, $Z \to q\bar{q}$ production, as a single $gg \to H$ process. The $b\bar{b}H$ production mode is modeled as a 1% [31] increase of the $gg \to H$ yield in each STXS cross section, since the acceptances for both processes are similar for all input analyses [31]. Theory uncertainties for the $gg \to H$, $qq \to Hqq$, and $t\bar{t}H$ processes are defined as in Ref. [10, 15], while those of the V(lep)H process follow the scheme described in Ref. [74].

For each production mode, multiple levels of progressively more detailed partitioning are defined with STXS stages [31]. The most detailed Stage 1.2 splitting of the STXS framework is implemented by the 139 fb^{-1} measurements of $H \to b\bar{b}$ (VH), $H \to ZZ^* \to 4\ell$ and $H \to \gamma\gamma$ presented in this note, which allows for their use in the EFT interpretation analysis. However, as the individual analyses provide only limited sensitivity to some of the Stage 1.2 categories, some of these categories are merged for the combined EFT analysis. The mapping of the merged EFT regions to the STXS Stage 1.2 regions is detailed in Table 2, and the corresponding measured signal strengths and their correlations are shown in Fig. 1 and Fig. 2 respectively. For the measurement bins defined by merging several bins of the STXS Stage-1.2 framework, the efficiency and acceptance factors $\epsilon_k^{i,X}$ are determined using SM predictions for the relative fraction of each Stage-1.2 bin. SM uncertainties in these fractions are taken into account.

For the MSSM interpretation only inclusive cross section predictions are available, hence STXS Stage 1.2 regions do not represent a useful level of detail for this interpretation. Therefore, for the MSSM analysis all STXS-1.2 cross sections are merged into the six Stage-0 cross sections (as defined in the first column of Table 2.) Therefore, the MSSM interpretation can include six additional Higgs boson analyses that are only available in more coarse-grained STXS levels (Level 0 and 1.0), as shown in Table 1.

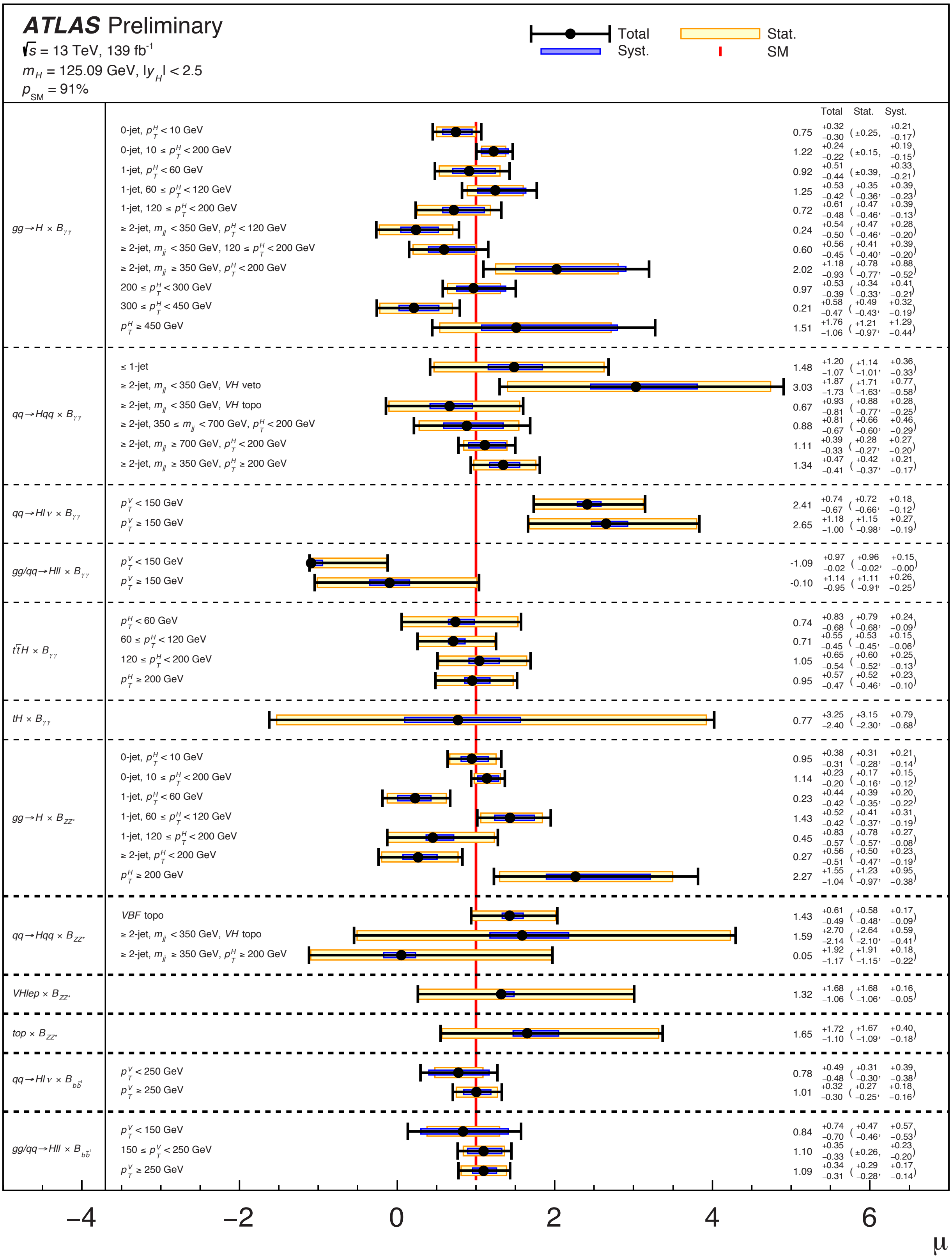

Figure 1: Measured signal strength for each STXS category entering the EFT analysis. The corresponding categories are defined in Table 2. Input data taken from Ref. [9]. The probability to obtain the observed data under the SM hypothesis (p_{SM}) is 91%.

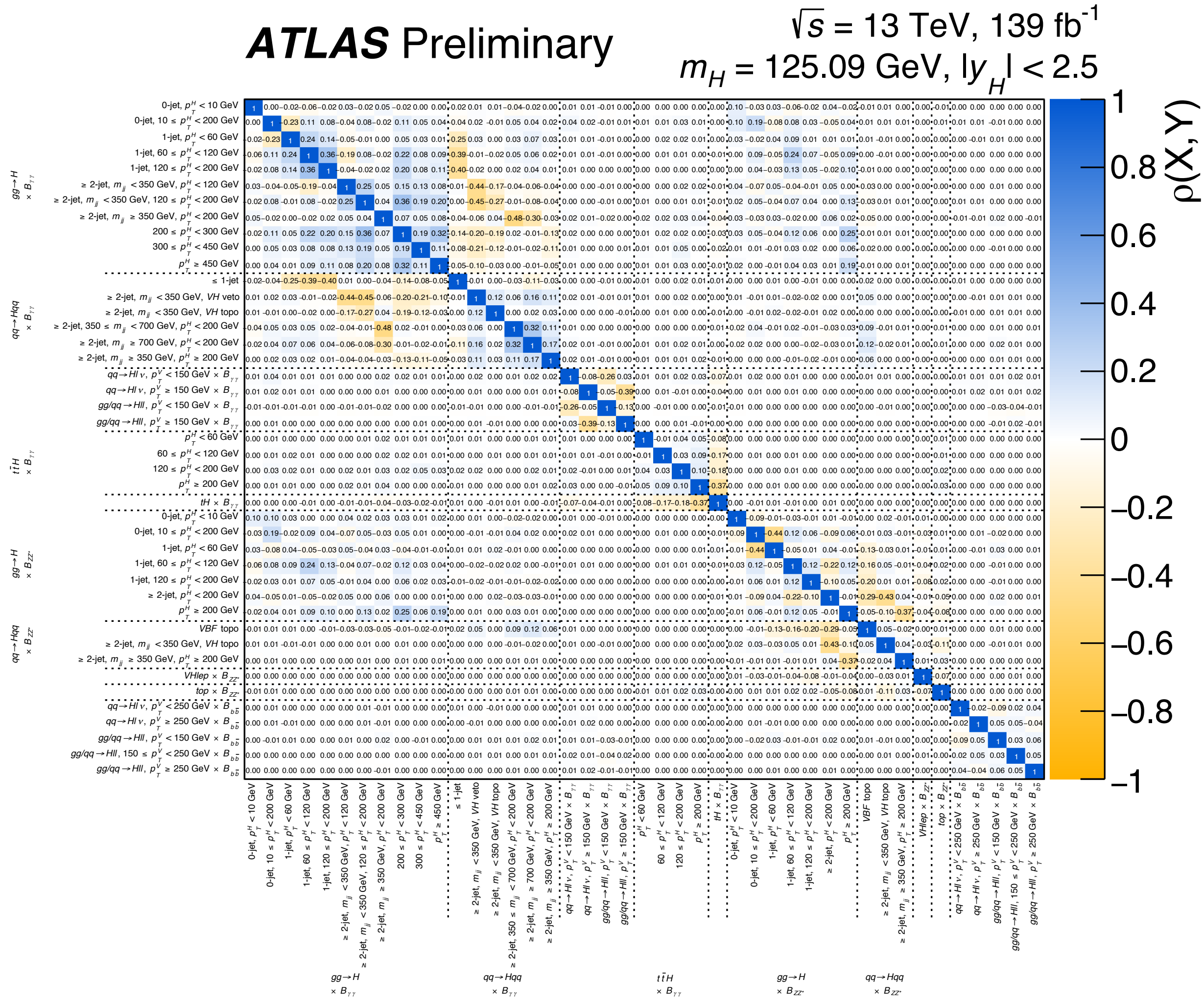

Figure 2: Correlation matrix corresponding to the measurements shown in Fig. 1. Input data taken from Ref. [9].

Table 2: Definition of Simplified Template Cross Sections at Stage-0 and Stage-1.2, and their mapping to the merged regions used for the EFT reinterpretation analysis. All dimensional quantities are in units of GeV. All bins sharing the same label are merged.

STXS Region Stage-0	STXS Region Stage-1.2	$H\to\gamma\gamma$	$H\to ZZ^*\to 4\ell$	$H\to b\bar{b}$ (VH)
ggH	$N_{\text{jets}}=0$, p_T^H<10	$N_{\text{jets}}=0$, p_T^H<10	$N_{\text{jets}}=0$, p_T^H<10	
	$N_{\text{jets}}=0$, 10<p_T^H	$N_{\text{jets}}=0$, 10<p_T^H	$N_{\text{jets}}=0$, 10<p_T^H	
	$N_{\text{jets}}=1$, p_T^H<60	$N_{\text{jets}}=1$, p_T^H<60	$N_{\text{jets}}=1$, p_T^H<60	
	$N_{\text{jets}}=1$, 60<p_T^H<120	$N_{\text{jets}}=1$, 60<p_T^H<120	$N_{\text{jets}}=1$, 60<p_T^H<120	
	$N_{\text{jets}}=1$, 120<p_T^H<200	$N_{\text{jets}}=1$, 120<p_T^H<200	$N_{\text{jets}}=1$, 120<p_T^H<200	
	$N_{\text{jets}}\geq 2$, m_{jj}<350, p_T^H<60	$N_{\text{jets}}\geq 2$, m_{jj}<350, p_T^H<120	$N_{\text{jets}}\geq 2$, $p_T^H\leq 200$	
	$N_{\text{jets}}\geq 2$, m_{jj}<350, 60<p_T^H<120	$N_{\text{jets}}\geq 2$, m_{jj}<350, p_T^H<120	$N_{\text{jets}}\geq 2$, $p_T^H\leq 200$	
	$N_{\text{jets}}\geq 2$, m_{jj}<350, 120<p_T^H<200	$N_{\text{jets}}\geq 2$, m_{jj}<350, 120<p_T^H<200	$N_{\text{jets}}\geq 2$, $p_T^H\leq 200$	
	$N_{\text{jets}}\geq 2$, 350<m_{jj}<700, p_T^H<200, p_T^{Hjj}<25	$N_{\text{jets}}\geq 2$, 350<m_{jj}, p_T^H<200	$N_{\text{jets}}\geq 2$, $p_T^H\leq 200$	
	$N_{\text{jets}}\geq 2$, 350<m_{jj}<700, p_T^H<200, 25<p_T^{Hjj}	$N_{\text{jets}}\geq 2$, 350<m_{jj}, p_T^H<200	$N_{\text{jets}}\geq 2$, $p_T^H\leq 200$	
	$N_{\text{jets}}\geq 2$, 700<m_{jj}, p_T^H<200, p_T^{Hjj}<25	$N_{\text{jets}}\geq 2$, 350<m_{jj}, p_T^H<200	$N_{\text{jets}}\geq 2$, $p_T^H\leq 200$	
	$N_{\text{jets}}\geq 2$, 700<m_{jj}, p_T^H<200, 25<p_T^{Hjj}	$N_{\text{jets}}\geq 2$, 350<m_{jj}, p_T^H<200	$N_{\text{jets}}\geq 2$, $p_T^H\leq 200$	
	200<p_T^H<300	200<p_T^H<300	200<p_T^H	
	300<p_T^H<450	300<p_T^H<450	200<p_T^H	
	450<p_T^H<650	450<p_T^H	200<p_T^H	
	650<p_T^H	450<p_T^H	200<p_T^H	
$qq\to Hqq$ "VBF", "$qqVH$ had"	$N_{\text{jets}}=0$	$N_{\text{jets}}\leq 1$		
	$N_{\text{jets}}=1$	$N_{\text{jets}}\leq 1$		
	$N_{\text{jets}}\geq 2$, m_{jj}<60	$N_{\text{jets}}\geq 2$, m_{jj}<60 $\vee$ 120<m_{jj}<350	VBF	
	$N_{\text{jets}}\geq 2$, 60<m_{jj}<120	$N_{\text{jets}}\geq 2$, 60<m_{jj}<120	$N_{\text{jets}}\geq 2$, 60<m_{jj}<120	
	$N_{\text{jets}}\geq 2$, 120<m_{jj}<350	$N_{\text{jets}}\geq 2$, m_{jj}<60 $\vee$ 120<m_{jj}<350	VBF	
	$N_{\text{jets}}\geq 2$, 350<m_{jj} 200<p_T^H	$N_{\text{jets}}\geq 2$, 350<m_{jj}, 200<p_T^H	$N_{\text{jets}}\geq 2$, 350<m_{jj}, 200<p_T^H	
	$N_{\text{jets}}\geq 2$, 350<m_{jj}<700, p_T^H<200, p_T^{Hjj}<25	$N_{\text{jets}}\geq 2$, 350<m_{jj}<700, p_T^H<200	VBF	
	$N_{\text{jets}}\geq 2$, 350<m_{jj}<700, p_T^H<200, 25<p_T^{Hjj}	$N_{\text{jets}}\geq 2$, 350<m_{jj}<700, p_T^H<200	VBF	
	$N_{\text{jets}}\geq 2$, 700<m_{jj}, p_T^H<200, p_T^{Hjj}<25	$N_{\text{jets}}\geq 2$, 700<m_{jj}, p_T^H<200	VBF	
	$N_{\text{jets}}\geq 2$, 700<m_{jj}, p_T^H<200, 25<p_T^{Hjj}	$N_{\text{jets}}\geq 2$, 700<m_{jj}, p_T^H<200	VBF	
$qq\to H\ell\nu$ "$qqWH$ lep"	p_T^V<75 ($N_{\text{jets}}=0$ / $N_{\text{jets}}=1$ / $N_{\text{jets}}\geq 2$)	WH p_T^V<150	VH lep	WH p_T^V<250
	75<p_T^V<150 ($N_{\text{jets}}=0$ / $N_{\text{jets}}=1$ / $N_{\text{jets}}\geq 2$)	WH p_T^V<150	VH lep	WH p_T^V<250
	150<p_T^V<250 ($N_{\text{jets}}=0$ / $N_{\text{jets}}=1$ / $N_{\text{jets}}\geq 2$)	WH 150<p_T^V	VH lep	WH p_T^V<250
	250<p_T^V<400 ($N_{\text{jets}}=0$ / $N_{\text{jets}}=1$ / $N_{\text{jets}}\geq 2$)	WH 150<p_T^V	VH lep	WH 250<p_T^V
	400<p_T^V ($N_{\text{jets}}=0$ / $N_{\text{jets}}=1$ / $N_{\text{jets}}\geq 2$)	WH 150<p_T^V	VH lep	WH 250<p_T^V
$qq\to H\ell\ell$ "$qqZH$ lep"	p_T^V<75 ($N_{\text{jets}}=0$ / $N_{\text{jets}}=1$ / $N_{\text{jets}}\geq 2$)	ZH p_T^V<150	VH lep	ZH p_T^V<150
	75<p_T^V<150 ($N_{\text{jets}}=0$ / $N_{\text{jets}}=1$ / $N_{\text{jets}}\geq 2$)	ZH p_T^V<150	VH lep	ZH p_T^V<150
	150<p_T^V<250 ($N_{\text{jets}}=0$ / $N_{\text{jets}}=1$ / $N_{\text{jets}}\geq 2$)	ZH 150<p_T^V	VH lep	ZH 150<p_T^V<250
	250<p_T^V<400 ($N_{\text{jets}}=0$ / $N_{\text{jets}}=1$ / $N_{\text{jets}}\geq 2$)	ZH 150<p_T^V	VH lep	ZH 250<p_T^V
	400<p_T^V ($N_{\text{jets}}=0$ / $N_{\text{jets}}=1$ / $N_{\text{jets}}\geq 2$)	ZH 150<p_T^V	VH lep	ZH 250<p_T^V
$gg\to H\ell\ell$ "$ggZH$ lep"	p_T^V<75 ($N_{\text{jets}}=0$ / $N_{\text{jets}}=1$ / $N_{\text{jets}}\geq 2$)	ZH p_T^V<150	VH lep	ZH p_T^V<150
	75<p_T^V<150 ($N_{\text{jets}}=0$ / $N_{\text{jets}}=1$ / $N_{\text{jets}}\geq 2$)	ZH p_T^V<150	VH lep	ZH p_T^V<150
	150<p_T^V<250 ($N_{\text{jets}}=0$ / $N_{\text{jets}}=1$ / $N_{\text{jets}}\geq 2$)	ZH 150<p_T^V	VH lep	ZH 150<p_T^V<250
	250<400 ($N_{\text{jets}}=0$ / $N_{\text{jets}}=1$ / $N_{\text{jets}}\geq 2$)	ZH 150<p_T^V	VH lep	ZH 250<p_T^V
	250<p_T^V ($N_{\text{jets}}=0$ / $N_{\text{jets}}=1$ / $N_{\text{jets}}\geq 2$)	ZH 150<p_T^V	VH lep	ZH 250<p_T^V
$t\bar{t}H$	p_T^H<60	p_T^H<60	$t(t)H$	
	60<p_T^H<120	60<p_T^H<120	$t(t)H$	
	120<p_T^H<200	120<p_T^H<200	$t(t)H$	
	200<p_T^H<300	200<p_T^H	$t(t)H$	
	300<p_T^H	200<p_T^H	$t(t)H$	
	$b\bar{b}H$	merged with ggH		
	tH	tH	$t(t)H$	

3 Methodology of Effective Field Theory interpretations

Standard Model Effective Field Theory provides a theoretically elegant language to encode the modifications of the Higgs properties induced by a wide class of beyond-the-SM models that reduce to the SM at low energies, and is systematically improvable with higher-order perturbative calculations. Within the mathematical language of the SMEFT, the effects of BSM dynamics at high energies $\Lambda \gg v$, well above the electroweak scale $v = 246$ GeV, can be parametrised at low energies, $E \ll \Lambda$, in terms of higher-dimensional operators built up from the Standard Model fields and respecting its symmetries such as gauge invariance

$$\mathcal{L}_{\mathrm{SMEFT}} = \mathcal{L}_{\mathrm{SM}} + \sum_{i}^{N_{d6}} \frac{c_i}{\Lambda^2} O_i^{(6)} + \sum_{j}^{N_{d8}} \frac{b_j}{\Lambda^4} O_j^{(8)} + \ldots, \tag{4}$$

where $\mathcal{L}_{\mathrm{SM}}$ is the SM Lagrangian, $O_i^{(6)}$ and $O_j^{(8)}$ represent a complete set of operators of mass-dimensions $d = 6$ and $d = 8$, and c_j, b_j are the corresponding Wilson coefficients. Operators with $d = 5$ and $d = 7$ violate lepton and/or baryon number conservation and are not relevant for Higgs physics. The effective theory expansion in Eq. (4) is robust, fully general, and can be systematically matched to explicit ultraviolet-complete BSM scenarios.

In this analysis the "Warsaw" basis [75] is used, which forms a complete set of all $O_i^{(6)}$ operators in Eq. (4) allowed by the SM gauge symmetries. This basis is widely used in EFT measurements in various fields of particle physics and the usage of a common basis will allow easier future combination of these measurements. Contributions of operators of mass-dimension $d = 8$ are not considered. The goal of the analysis is to constrain the $d = 6$ Wilson coefficients that correspond to operators that either directly or indirectly impact Higgs boson couplings to SM particles [14, 76]. Table 3 lists the operators considered in this analysis, and their corresponding Wilson coefficients c_j. Here, all CP-even $d = 6$ operators were considered for which the Λ^{-2}-suppressed contribution to any of the STXS categories measured in Figure 1 exceeds 1‰ with respect to the SM prediction at $c_i = 1$. In this analysis, a value of $\Lambda = 1$ TeV is assumed, coefficients for alternative values of $\Lambda = X$ can be trivially obtained through a scaling with a factor $(X/1\ \mathrm{TeV})^2$. All complex-valued Wilson coeffients, notably c_{uW}, c_{uG}, c_{uB} and c_{uH} in this analysis, are used with $\Im(c_i) = 0$.

3.1 Simulation of the impact of SMEFT operators

The impact of the $d = 6$ SMEFT operators listed in Table 3 has been computed with the UFO model of Madgraph [53], using lowest order calculations in QCD for all production and decay modes.

Calculations for Higgs production modes with tree-level diagrams have been performed with SMEFTsim [77], under the assumption of a $U(3)^5$ flavour symmetry (which corresponds to the unbroken global flavour symmetry present in the SM outside the Yukawa sector), and providing the Fermi constant G_F, and the Z and W boson masses as input. Cross-sections have been calculated at NLO accuracy in QCD for ggH, $gg \to ZH$ and $H \to gg$ with SMEFTatNLO [78] and at NLO accuracy in QED for SMEFT-SM interference terms in $H \to \gamma\gamma$ [79], also providing m_W as input. SMEFT modifications to the background processes in the included analyses are not considered.

In the simulation, kinematic cuts on the minimal (b-)jet transverse momentum of $p_{\mathrm{T}} > 20$ GeV have been imposed. Furthermore, for the Higgs boson decay a requirement of $\Delta R > 0.05$ between two jets or two leptons is imposed in order to avoid divergences in the matrix element calculation. Additional

Table 3: Wilson coefficients c_j and corresponding $d = 6$ SMEFT operators O_j used in this analysis. Corresponding example diagrams are shown in Tables 17 and 18 in Appendix A.

Wilson coefficient	Operator	Wilson coefficient	Operator
$c_{H\Box}$	$(H^\dagger H)\Box(H^\dagger H)$	c_{uG}	$(\bar{q}_p\sigma^{\mu\nu}T^A u_r)\widetilde{H}\,G^A_{\mu\nu}$
c_{HDD}	$\left(H^\dagger D^\mu H\right)^*\left(H^\dagger D_\mu H\right)$	c_{uW}	$(\bar{q}_p\sigma^{\mu\nu}u_r)\tau^I\widetilde{H}\,W^I_{\mu\nu}$
c_{HG}	$H^\dagger H\,G^A_{\mu\nu}G^{A\mu\nu}$	c_{uB}	$(\bar{q}_p\sigma^{\mu\nu}u_r)\widetilde{H}\,B_{\mu\nu}$
c_{HB}	$H^\dagger H\,B_{\mu\nu}B^{\mu\nu}$	c'_{ll}	$(\bar{l}_p\gamma_\mu l_t)(\bar{l}_r\gamma^\mu l_s)$
c_{HW}	$H^\dagger H\,W^I_{\mu\nu}W^{I\mu\nu}$	$c^{(1)}_{qq}$	$(\bar{q}_p\gamma_\mu q_t)(\bar{q}_r\gamma^\mu q_s)$
c_{HWB}	$H^\dagger\tau^I H\,W^I_{\mu\nu}B^{\mu\nu}$	$c^{(3)}_{qq}$	$(\bar{q}_p\gamma_\mu\tau^I q_r)(\bar{q}_s\gamma^\mu\tau^I q_t)$
c_{eH}	$(H^\dagger H)(\bar{l}_p e_r H)$	c_{qq}	$(\bar{q}_p\gamma_\mu q_t)(\bar{q}_r\gamma^\mu q_s)$
c_{uH}	$(H^\dagger H)(\bar{q}_p u_r\widetilde{H})$	$c^{(31)}_{qq}$	$(\bar{q}_p\gamma_\mu\tau^I q_t)(\bar{q}_r\gamma^\mu\tau^I q_s)$
c_{dH}	$(H^\dagger H)(\bar{q}_p d_r\widetilde{H})$	c_{uu}	$(\bar{u}_p\gamma_\mu u_r)(\bar{u}_s\gamma^\mu u_t)$
$c^{(1)}_{Hl}$	$(H^\dagger i\overleftrightarrow{D}_\mu H)(\bar{l}_p\gamma^\mu l_r)$	$c^{(1)}_{uu}$	$(\bar{u}_p\gamma_\mu u_t)(\bar{u}_r\gamma^\mu u_s)$
$c^{(3)}_{Hl}$	$(H^\dagger i\overleftrightarrow{D}^I_\mu H)(\bar{l}_p\tau^I\gamma^\mu l_r)$	$c^{(1)}_{qu}$	$(\bar{q}_p\gamma_\mu q_t)(\bar{u}_r\gamma^\mu u_s)$
c_{He}	$(H^\dagger i\overleftrightarrow{D}_\mu H)(\bar{e}_p\gamma^\mu e_r)$	$c^{(8)}_{ud}$	$(\bar{u}_p\gamma_\mu T^A u_r)(\bar{d}_s\gamma^\mu T^A d_t)$
$c^{(1)}_{Hq}$	$(H^\dagger i\overleftrightarrow{D}_\mu H)(\bar{q}_p\gamma^\mu q_r)$	$c^{(8)}_{qu}$	$(\bar{q}_p\gamma_\mu T^A q_r)(\bar{u}_s\gamma^\mu T^A u_t)$
$c^{(3)}_{Hq}$	$(H^\dagger i\overleftrightarrow{D}^I_\mu H)(\bar{q}_p\tau^I\gamma^\mu q_r)$	$c^{(8)}_{qd}$	$(\bar{q}_p\gamma_\mu T^A q_r)(\bar{d}_s\gamma^\mu T^A d_t)$
c_{Hu}	$(H^\dagger i\overleftrightarrow{D}_\mu H)(\bar{u}_p\gamma^\mu u_r)$	c_W	$\epsilon^{IJK}W^{I\nu}_\mu W^{J\rho}_\nu W^{K\mu}_\rho$
c_{Hd}	$(H^\dagger i\overleftrightarrow{D}_\mu H)(\bar{d}_p\gamma^\mu d_r)$	c_G	$f^{ABC}G^{A\nu}_\mu G^{B\rho}_\nu G^{C\mu}_\rho$

generator-level cuts are listed in Table 9 in Appendix A. For all events Pythia8 [64] is used for the simulation of parton showering, where Higgs decay is based on the Higgs width from Madgraph. A matching is performed to remove phase space overlap between the jets from the matrix element and the shower. The CKKW-l algorithm is used for all tree-level processes, with a matching parameter of 30 GeV, whereas the MLM algorithm [80, 81] is used for loop-induced processes, in particular ggH. The Rivet program [82] with the `HiggsTemplateCrossSections` [83] routine is used to analyse the simulated events, compute high-level kinematic quantities and classify the events according to their STXS bin.[2]

The STXS cross section predictions for a specific process, calculated as described above, are simulated in three independent parts:

$$\sigma_{\text{STXS}} = \sigma_{\text{SM}} + \sigma_{\text{int}} + \sigma_{\text{BSM}} \tag{5}$$

where σ_{SM} is the SM cross section, σ_{int} describes the interference between the SMEFT operators (BSM physics) and SM operators, and σ_{BSM} is the cross-section involving exclusively SMEFT operators. When considering only $d = 6$ SMEFT operators, it follows from Eq. (4) that σ_{int} consists of terms involving a single $d = 6$ SMEFT operator, suppressing each term by a factor Λ^{-2}, and that σ_{BSM} contains terms involving products of two $d = 6$ SMEFT operators, suppressing each term by a factor Λ^{-4}. For this reason the impact of the σ_{BSM} term is generally expected to be small, though its impact may still be non-negligible

[2] The Rivet algorithm has been modified to classify events in which a Higgs boson and two leptons arise from the same production vertex as VH production events. This modification ensures the proper classification of events with leptons from off-shell V decays, since MadGraph is only saving on-shell intermediate particles. Contributions from off-shell V bosons are small in the SM, but can be enhanced by SMEFT operators.

in certain regions of phase space, e. g. when energy scales are of order Λ.

The lowest-order cross-section terms generated by $d = 8$ operators that involve interference between SM and $d = 8$ SMEFT operators are also suppressed by a factor Λ^{-4}. As no complete calculations are available yet for $d = 8$ operators, their magnitude relative to σ_{BSM}, which is suppressed at the same order, is unknown. However, SMEFT interpretations will be presented both with and without the σ_{BSM} contribution to give a general indication of the sensitivity of the analysis to Λ^{-4} terms.

To reduce the impact of the limited QCD calculation order of SMEFT operators, the parametrisation of the predicted cross section is computed as a relative correction to a SM prediction that is computed at the highest available order for each process:

$$\sigma_{\text{STXS}} = \sigma_{\text{SM}}^{\text{((N)N)NLO}} \times \left(1 + \frac{\sigma_{\text{int}}^{\text{(N)LO}}}{\sigma_{\text{SM}}^{\text{(N)LO}}} + \frac{\sigma_{\text{BSM}}^{\text{(N)LO}}}{\sigma_{\text{SM}}^{\text{(N)LO}}}\right). \tag{6}$$

This calculation strategy assumes that the correction to the cross section from SMEFT operators is comparable at LO and higher orders [84].

Observable cross-sections are further modified by the impact of SMEFT operators on Higgs decay branching fractions. Since the Higgs boson is a narrow, scalar particle, and only on-shell production is considered in this analysis, its production cross section and decay width factorise. The impact of SMEFT operators on production and decay therefore also factorise and can be derived independently. Thus, the cross section for a given STXS region i and a given decay mode $H \to X$ is

$$(\sigma{\times}B)^{i,H\to X} = \sigma^{i} \times B^{H\to X} = \left(\sigma_{\text{SM}}^{i} + \sigma_{\text{int}}^{i} + \sigma_{\text{BSM}}^{i}\right) \times \left(\frac{\Gamma_{\text{SM}}^{H\to X} + \Gamma_{\text{int}}^{H\to X} + \Gamma_{\text{BSM}}^{H\to X}}{\Gamma_{\text{SM}}^{H} + \Gamma_{\text{int}}^{H} + \Gamma_{\text{BSM}}^{H}}\right). \tag{7}$$

Factorising the SM prediction, to allow the use of Eq. (6), the expression becomes

$$(\sigma{\times}B)^{i,H\to X} = (\sigma{\times}B)_{\text{SM,(N(N))NLO}}^{i,H\to X} \left(1 + \frac{\sigma_{\text{int,(N)LO}}^{i}}{\sigma_{\text{SM,(N)LO}}^{i}} + \frac{\sigma_{\text{BSM,(N)LO}}^{i}}{\sigma_{\text{SM,(N)LO}}^{i}}\right) \left(\frac{1 + \frac{\Gamma_{\text{int}}^{H\to X}}{\Gamma_{\text{SM}}^{H\to X}} + \frac{\Gamma_{\text{BSM}}^{H\to X}}{\Gamma_{\text{SM}}^{H\to X}}}{1 + \frac{\Gamma_{\text{int}}^{H}}{\Gamma_{\text{SM}}^{H}} + \frac{\Gamma_{\text{BSM}}^{H}}{\Gamma_{\text{SM}}^{H}}}\right), \tag{8}$$

where the ratios $\sigma_{\text{int}}/\sigma_{\text{SM}}$ and $\Gamma_{\text{int}}/\Gamma_{\text{SM}}$ have a linear dependence on SMEFT operators and are suppressed by a factor Λ^{-2}, and the ratios $\sigma_{\text{BSM}}/\sigma_{\text{SM}}$ and $\Gamma_{\text{BSM}}/\Gamma_{\text{SM}}$ have a quadratic dependence on SMEFT operators and are suppressed by a factor Λ^{-4}. In the analysis these ratios are parametrised as

$$\frac{\sigma_{\text{int}}^{i}}{\sigma_{\text{SM}}^{i}} = \sum_{j} A_{j}^{\sigma_i} c_j \qquad \frac{\sigma_{\text{BSM}}^{i}}{\sigma_{\text{SM}}^{i}} = \sum_{jk} B_{jk}^{\sigma_i} c_j c_k \tag{9}$$

$$\frac{\Gamma_{\text{int}}^{H\to X}}{\Gamma_{\text{SM}}^{H\to X}} = \sum_{j} A_{j}^{\Gamma^{H\to X}} c_j \qquad \frac{\Gamma_{\text{BSM}}^{H\to X}}{\Gamma_{\text{SM}}^{H\to X}} = \sum_{jk} B_{jk}^{\Gamma^{H\to X}} c_j c_k \tag{10}$$

$$\frac{\Gamma_{\text{int}}^{H}}{\Gamma_{\text{SM}}^{H}} = \sum_{j} A_{j}^{\Gamma^{H}} c_j \qquad \frac{\Gamma_{\text{BSM}}^{H}}{\Gamma_{\text{SM}}^{H}} = \sum_{jk} B_{jk}^{\Gamma^{H}} c_j c_k, \tag{11}$$

where all A_j and B_{jk} are constant factors obtained from simulation that express the sensitivity of the analysis to the operators O_j that correspond to the Wilson coefficients c_j, and indices j, k run over all non-negligible operators.

From Equations (8)-(11) two statistical models are constructed for the interpretation of the data: a fully linearised variant that only considers terms suppressed by up to a factor Λ^{-2}, and a quadratic variant that considers all available terms, including those with suppression factor Λ^{-4}.

3.2 Statistical model with linear terms

In a scenario where Λ^{-4}-suppressed contributions are ignored, the predicted signal event count can be explicitly linearised as function of the Wilson coefficients c_j. Ignoring all Λ^{-4}-suppressed BSM terms in Eq. (8), and using the parametrisation of Eq. (9)-(11), the expression for the cross-section reduces to

$$(\sigma\times B)^{i,H\to X} = (\sigma\times B)^{i,H\to X}_{\text{SM,((N)N)NLO}} \times \left(1+\frac{\sigma^{i}_{\text{int,(N)LO}}}{\sigma^{i}_{\text{SM,(N)LO}}}\right)\times\left(\frac{1+\frac{\Gamma^{H\to X}_{\text{int}}}{\Gamma^{H\to X}_{\text{SM}}}}{1+\frac{\Gamma^{H}_{\text{int}}}{\Gamma^{H}_{\text{SM}}}}\right) \tag{12}$$

$$= (\sigma\times B)^{i,H\to X}_{\text{SM,((N)N)LO}} \times \left(1+\sum_j A^{\sigma_i}_j c_j\right)\times\left(\frac{1+\sum_j A^{\Gamma^{H\to X}}_j c_j}{1+\sum_j A^{\Gamma^{H}}_j c_j}\right), \tag{13}$$

A Taylor expansion of the ratio expression in Eq. (13) results in a fully linearised expression for terms of order Λ^{-2},

$$(\sigma\times B)^{i,H\to X}_{\text{SM}+\Lambda^{-2}} = (\sigma\times B)^{i,H\to X}_{\text{SM,((N)N)LO}} \times \left(1+\sum_j A^{\sigma_i}_j c_j + \sum_j A^{\Gamma^{H\to X}}_j c_j - \sum_j A^{\Gamma^{H}}_j c_j\right) + O\left(\Lambda^{-4}\right) \tag{14}$$

$$= (\sigma\times B)^{i,H\to X}_{\text{SM,((N)N)LO}} \times \left(1+\sum_j \left(A^{\sigma_i}_j + A^{\Gamma^{H\to X}}_j - A^{\Gamma^{H}}_j\right) c_j\right) + O\left(\Lambda^{-4}\right), \tag{15}$$

where all higher order terms from the expansion are suppressed by power Λ^{-4} or beyond. Fig. 3 visualises the linear scale factors $A^{\sigma_i}_j$ and $(A^{\Gamma^{H\to X}}_j - A^{\Gamma^{H}}_j)$ for the relevant SMEFT operators associated to c_j on the STXS cross-sections and branching fractions. Using Eq. (15), the signal strength modifier for each analysis region k is computed as

$$\mu^{i,X} = \frac{(\sigma\times B)^{i,H\to X}_{\text{SM}+\Lambda^{-2}}}{(\sigma\times B)_{\text{SM,MC}}}. \tag{16}$$

It is assumed that the systematic uncertainties assigned to the acceptance factors $\epsilon^{i,X}_k$ that multiply $\mu^{i,X}$ in Eq. (2), arising from theory uncertainties which are fully taken into account in the SM cross-section prediction, cover the possible acceptance changes induced by SMEFT operators in Higgs production through the full validity range of the SMEFT model. The use of this assumption is motivated by the similarity of reconstruction-level analysis regions to STXS cross-section regions, which are designed to be relatively insensitive to acceptance changes induced by SMEFT operators. The effect of SMEFT operators on other observables used in the definition of the analysis regions, e.g through multivariate discriminants, is assumed to be negligible.

Conversely, the effect of SMEFT operators on Higgs boson decays can strongly affect the acceptance factors $\epsilon_k^{i,X}$, since decays are not limited to a restricted fiducial phase space in the STXS framework. The four-body $H\to ZZ^*\to 4\ell$ analysis is significantly impacted by acceptance effects due to the explicit relation of the analysis-level selection to m_Z, and an acceptance correction factor developed in Ref. [10] is used as an additional multiplicative factor in Eq. (16) for all analysis regions measuring $H\to ZZ^*\to 4\ell$ decays. This acceptance correction is derived as a function of c_{HW}, c_{HB} and c_{HWB}, as only these are measured in Ref. [10]. In principle, a dependence of this correction on $c_{Hl}^{(1)}$ and c_{He} is also expected, but is neglected in this analysis as the overall sensitivity to these operators is small. The small non-linear effect that the use of this acceptance correction has with respect to the assumed the linearity of Eq. (16) for $H\to ZZ^*\to 4\ell$ is neglected. For all other Higgs decays, the acceptance effects are neglected.

3.3 Statistical model with linear and quadratic terms

Alternatively, inserting the parametrisation of Eq. (9)-(11) in Eq. (8), gives

$$(\sigma\times B)^{i,H\to X}_{\mathrm{SM}+\Lambda^{-4}} = (\sigma\times B)^{i,H\to X}_{\mathrm{SM,((N)N)LO}}\left(1+\sum_j A_j^{\sigma_i}c_j+\sum_{jk}B_{jk}^{\sigma_i}c_jc_k\right)\left(\frac{1+\sum_j A_j^{\Gamma^{H\to X}}c_j+\sum_{jk}B_{jk}^{\Gamma^{H\to X}}c_jc_k}{1+\sum_j A_j^{\Gamma^{H}}c_j+\sum_{jk}B_{jk}^{\Gamma^{H}}c_jc_k}\right), \tag{17}$$

resulting in a prediction that includes all terms proportional to Λ^{-4}, while also retaining the terms suppressed by higher powers of Λ that arise in the ratio expression for the Higgs width. Assumptions made for this model on acceptance factors for production and decay are identical to those for the linear model.

While the set of operators proportional to Λ^{-4} considered in Eq. (8) is not complete, as terms expressing SM interference with $d = 8$ operators are not considered, a comparison of results obtained with the linear and quadratic statistical model will be indicative of the sensitivity of the measurement terms suppressed by Λ^{-4}.

Figure 4 illustrates the relative importance of the quadratic terms by comparing the impact $c_jA_j + c_j^2B_{jj}$ of variations of coefficients c_j in the various STXS regions and decay rates when including only linear terms A_j (shaded histograms) and when including both the linear and quadratic terms B_{jj} (open histograms). The relative importance of the quadratic term increases linearly with the considered variation of c_j, hence chosen magnitudes of the variations do not only scale the shown impact, but also the relative magnitude of the quadratic term. Figure 4 shows that the strongest impact of quadratic terms can be expected in the high-p_T regions of VH production for coefficients $c_{Hq}^{(3)}, c_{Hq}^{(1)}, c_{Hd}, c_{Hu}$ and in the tH channel for operator $c_{qq}^{(3)}$. Other regions that are subject to a moderately strong impact of quadratic terms are inclusive ggH production for operators c_{HG} and c_{uG}, and $\Gamma^{H\to\gamma\gamma}$ for c_{HB}, where in the latter case the impact is notably negative.

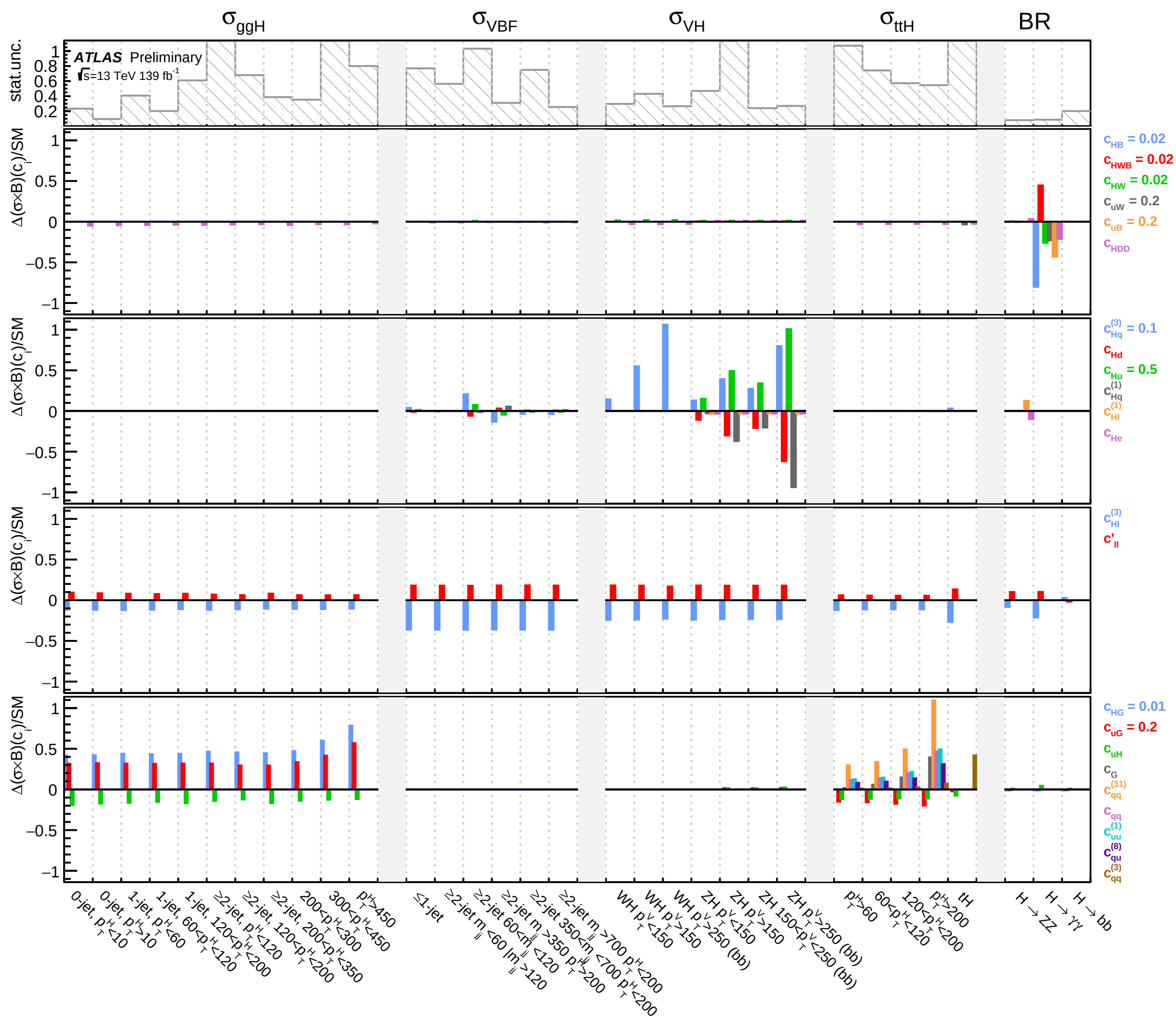

Figure 3: Impact of the most relevant SMEFT operators on the STXS regions and decay modes, relative to the SM cross-section, under the assumption of the linearized SMEFT model. For all coefficients c_j a unit variation is considered, unless specified otherwise in the legend. To judge the experimental sensitivity to constrain the operators from the data in the listed STXS regions, the statistical uncertainty on the corresponding regions (σ_{stat}) is shown in the top panel. For columns corresponding to multiple STXS×BR regions, the shown uncertainty reflects the statistical uncertainty on the average, under the assumption of uncorrelated statistical uncertainties. For presentational clarity, the statistical uncertainty of low precision STXS regions is clipped in the plot. The full parametrisation can be found in Tables 10 to 15 in Appendix A.

4 Constraints on Wilson coefficients of SMEFT operators

The aim of the EFT analysis is to obtain constraints on the Wilson coefficients c_j through a maximum likelihood analysis of the Higgs measurements expressed in the merged STXS Stage-1.2 regions shown in Table 2, i. e. $H\to\gamma\gamma$, $H\to ZZ^*\to 4\ell$ and $H\to b\bar{b}$ (VH): all signal strength modifiers $\mu^{i,X}$ of Eq. (2) are

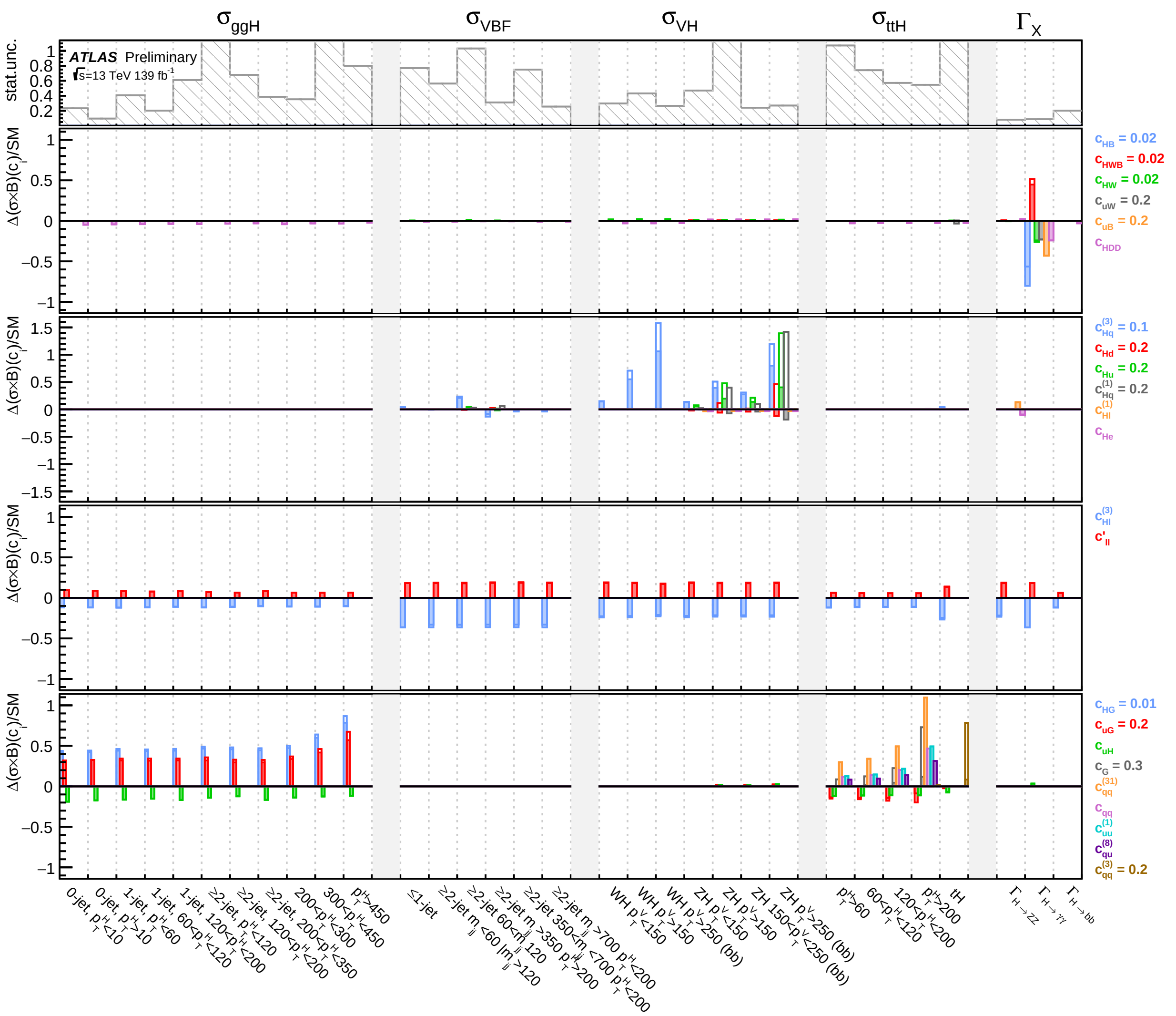

Figure 4: Comparison of the impact of the most relevant SMEFT operators on the STXS regions and decay modes, relative to the SM cross-section, for the linearized SMEFT model (shaded histogram) and the linear+quadratic SMEFT model (open histogram). For all coefficients c_j a unit variation is considered, unless specified otherwise in the legend. The variation shown for some c_j differ from those shown in Fig. 3. To judge the experimental sensitivity to constrain the operators from the data in the listed STXS regions, the statistical uncertainty on the corresponding regions (σ_{stat}) is shown in the top panel. For columns corresponding to multiple STXS×BR regions, the shown uncertainty reflects the statistical uncertainty on the average, under the assumption of uncorrelated statistical uncertainties. For presentational clarity, the statistical uncertainty of low precision STXS regions is clipped in the plot.

directly expressed in terms of the coefficients c_j:

$$s_k(c_i, \boldsymbol{\theta}) = \sum_{i,X} \left(\mu^{i,X} \equiv \frac{(\sigma\times B)^{i,H\to X}_{\text{SMEFT}}(c_i)}{(\sigma\times B)_{\text{SM,MC}}} \right) \times \mathcal{L} \times (\sigma\times B)^{i,X}_{\text{SM,MC}}(\boldsymbol{\theta}) \times \epsilon^{i,X}_k(\boldsymbol{\theta}), \tag{18}$$

with $\mathcal{L}$, $\epsilon^{i,X}_k(\boldsymbol{\theta})$ and $\boldsymbol{\theta}$ as defined in Eq. (2), and where the signal cross-section $(\sigma\times B)^{i,X}_{\text{SMEFT}}(c_j)$ is either taken from the linear model of Eq. (15) or the quadratic model of Eq. (17). In all results presented in this Section, the set of nuisance parameters $\boldsymbol{\theta}$ has been pruned, using an impact ranking technique, from

O(1000) down to O(700) nuisance parameters, which has an estimated cumulative impact on the estimated systematic uncertainty of less than 1%.

The available data samples contain insufficient information to constrain all coefficients c_j of Table 3 simultaneously, hence a standard numerical joint maximum likelihood estimation of this set of parameters c_j will not converge. As degrees of freedom left unconstrained by the data do not necessarily correspond to individual coefficients c_j, but may also be linear combinations $\sum_j a_j c_j$, the numeric estimation cannot be made to converge by considering only an appropriate subset of c_j in the estimation procedure, hence a modified basis will be used for the analysis.

4.1 Sensitivity estimate and choice of measured parameters

To determine a modified basis c'_i that can be estimated from the data, the SM expected covariance matrix V_{STXS} of the measurement, expressed in the basis of cross sections $(\sigma\times B)^i_{\text{STXS}}$, is analysed. The correlation matrix C_{STXS} corresponding to the V_{STXS} is shown in Fig. 2. From V_{STXS}, the Hessian matrix V^{-1}_{STXS} is obtained, and is rotated from the STXS basis $\mu^{i,X}$ to the SMEFT basis c_j

$$V^{-1}_{\text{SMEFT}} = P^T_{(i,X)\to(j)}\, V^{-1}_{\text{STXS}}\, P_{(i,X)\to(j)}. \tag{19}$$

The rotation matrix $P_{(i,X)\to(j)}$, is based on the linearised SMEFT model of Eq. (15):

$$P_{(i,X)\to(j)} = A_j^{\sigma_i} + A_j^{\Gamma^{H\to X}} - A_j^{\Gamma^H}, \tag{20}$$

where $A_j^{\sigma_i}$, $A_j^{\Gamma^{H\to X}}$ and $A_j^{\Gamma^H}$ are the constant factors obtained from simulation.

In the limit of Gaussian STXS measurements, the matrix V^{-1}_{SMEFT} represents the Fisher information matrix of its SMEFT re-parametrisation. An eigenvalue decomposition of the Fisher information matrix yields the eigenvectors e_i and their corresponding variances obtained from the eigenvalues, $V(e_i) = E_i^{-1}$. Figure 5 lists the eigenvectors and their corresponding eigenvalues obtained from the expected measurements and accounting for observed values of nuisance parameters, ranked by eigenvalue and truncated to eigenvalues $\lambda_i > 0.01$, corresponding to a truncation at an estimated uncertainty of $\sigma_{e_i} < 10$, well beyond the natural validity range of the c_i of EFTs of O(1).

From the ranking of Figure 5 and a survey of the sensitivity of the STXS regions to the Wilson coefficients in the linearised model, as shown in Fig. 3, the following observations are made:

1. Parameter $c^{(3)}_{Hq}$ can be individually well constrained (ev-3). The sensitivity is driven by the VH measurements, in particular $H \to b\bar{b}$ (VH).

2. Parameters c_{HG}, $|c_{uG}|$ and $|c_{uH}|$ are constrained by ggH and $t\bar{t}H$, while, c_{qq}, $c^{(3)}_{qq}$, $c^{(31)}_{qq}$, $c^{(1)}_{uu}$, $c^{(8)}_{ud}$, $c^{(1)}_{qu}$, $c^{(8)}_{qu}$, and c_G are only constrained from $t\bar{t}H$ (and $c^{(3)}_{qq}$ from tH) and affect the shape of the signal in a similar way. Therefore, only one linear combination (ev-5) of them can be precisely estimated. The most sensitive of these eigenvectors (ev-1,2) are a combination of c_{HG} and c_{uG}, which are the operators constrained strongest from ggH.

3. Parameters c_{HW}, c_{HB} and c_{HWB} are primarily constrained from $H\to\gamma\gamma$ decay (ev-1). The direction of ev-1 agrees at the percent-level with the predicted direction from the analytical calculation for $H\to\gamma\gamma$ decay width, as well as with the direction defined by the coefficient $C_{\gamma\gamma}$ of the SILH basis. Weaker constraints on c_{uW} andc_{uB} arise through a correlation with VH and VBF production (ev-2,3).

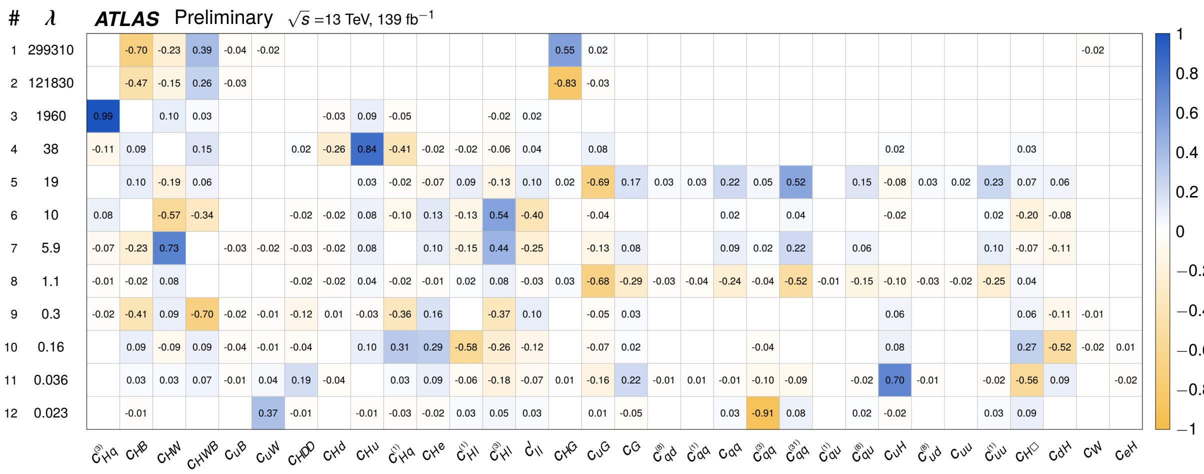

Figure 5: Eigenvectors of the inverse EFT covariance matrix obtained from EFT propagation to the covariance matrix V_{STXS} and with a significant (>0.01) eigenvalue λ. This eigenvalue threshold corresponds to an approximate expected uncertainty on that eigenvector of > 10.

4. A notable correlation exists between the weak constraints of $c^{(1)}_{Hl}$, $c^{(3)}_{Hl}$, c_{He} and $c^{(1)}_{Hq}$ (ev-9,10). This correlation has its source in the common measurement of most of these: $H \to b\bar{b}$ (VH). For this same reason also c_{Hu} and c_{Hd} are expected to be correlated, and this correlation group also includes $c^{(1)}_{Hq}$ (ev-4). Based on these observations, $c^{(1)}_{Hl}$ and c_{He} are grouped, $c^{(3)}_{Hl}$ and c'_{ll} are grouped, and c_{Hu}, c_{Hd} and $c^{(1)}_{Hq}$ are grouped.

Furthermore, parameters $c_{H\Box}$, c_{dH} and $|c_{eH}|$ all act as a global cross-section scale factor, are hence degenerate with a rescaling of all other c_j and therefore fixed at to zero. Balancing the aims of easy interpretability (each individual c_j maps to a model parameter, or combinations of c_j that arise in similar processes map to model parameter) and full decorrelation achieving numeric stability (each eigenvector e_i is a model parameter) , a new eigenvector decomposition in sub-spaces is constructed with guidance from the above observations on the decomposition:

$$
\begin{aligned}
\{c_i\} \quad = \quad & \{c^{(3)}_{Hq}\} \times \\
& \{c_{HG}, c_{uG}, c_{uH}, c^{(1)}_{qq}, c_{qq}, c^{(3)}_{qq}, c^{(31)}_{qq}, c_{uu}, c^{(1)}_{uu}, c^{(8)}_{ud}, c^{(1)}_{qu}, c^{(8)}_{qu}, c^{(8)}_{qd}, c_G\} \times \\
& \{c_{HW}, c_{HB}, c_{HWB}, c_{HDD}, c_{uW}, c_{uB}, \} \times \\
& \{c^{(1)}_{Hl}, c_{He}\} \times \\
& \{c^{(3)}_{Hl}, c'_{ll}\} \times \\
& \{c_{Hu}, c_{Hd}, c^{(1)}_{Hq}\}.
\end{aligned}
$$

The eigenvectors and values of the corresponding subspaces are listed in Table 4 and qualitatively confirm the observations from the analysis of the full STXS covariance matrix. The final parameter set c'_j constitutes the marked entries in Table 4 plus $c^{(3)}_{Hq}$, and the rotation matrix of this basis c'_j with respect to the Warsaw basis is visualised in Fig. 6.

The impact of variations of c'_j on the STXS regions and Higgs boson branching fractions is shown in Fig 7, with the same parameter grouping as was shown in Fig. 3, and demonstrates clearly that the basis c'_j represents impact variations across regions that are much more orthogonal than the Warsaw basis c_j.

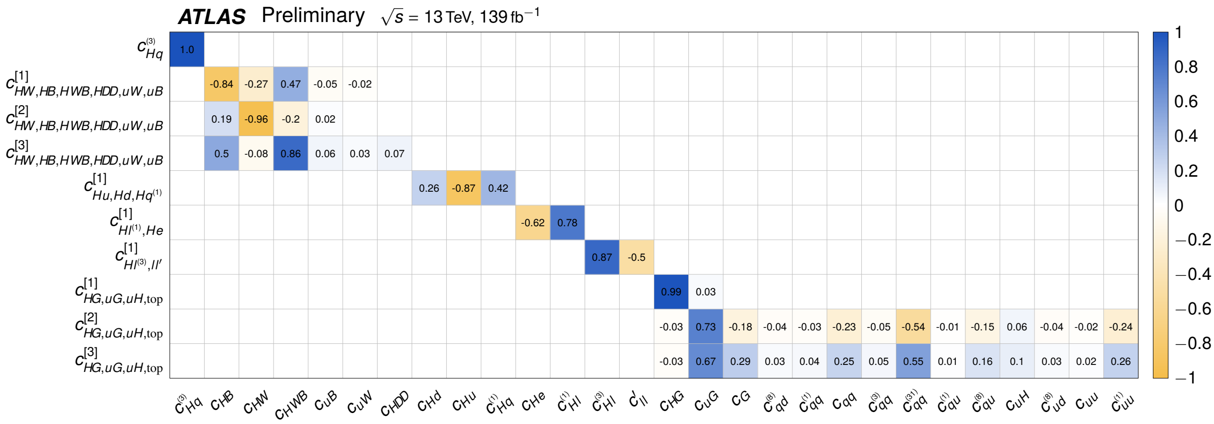

Figure 6: Visualization of the rotation matrix from the Warsaw basis c_j to the fit basis c'_j.

Scans of the profile likelihood reparametrized in the rotated basis c'_j confirm the absence of constraints in the direction of eigenvectors with weak eigenvalues, an example of which is shown in Fig. 8a, and the corresponding parameters are fixed to zero in the analysis. Furthermore, correlations between most c'_j exhibit a close to linear behaviour in a range of 2σ, as is shown in Fig. 8b, with the correlation of most c'_i and $c^{[1]}_{Hl^{(1)},He}$ being the main exception due to non-linear effects introduced by the $H \to ZZ^* \to 4\ell$ acceptance correction (See Fig. 8c for $c^{(3)}_{Hq}$, as a prominent example).

No separate optimisation of the parameter basis c'_j is performed for the quadratic SMEFT model of Eq. (17) as the non-linear effects of this model are expected to vanish for small c_j, thus asymptotically yielding the same rotation matrix as Eq. (20).

Table 4: Eigenvectors and eigenvalues from subspace rotations. The estimated variance associated with each eigenvector is the inverse of the corresponding eigenvalue. The eigenvectors $c^{[7]}_{HG,uG,uH,\mathrm{top}}$ through $c^{[14]}_{HG,uG,uH,\mathrm{top}}$ have eigenvalues $\lambda < 0.0001$ and are not shown. Eigenvectors that are retained as parameterized degrees of freedom in the final fit to data are marked in the last column.

Parameter		Definition	Eigenvalue	Fit Parameter
$c^{(3)}_{Hq}$		$c^{(3)}_{Hq}$	1900	✓
$c^{[i]}_{HW,HB,HWB,HDD,uW,uB}$	1	$-0.27c_{HW} - 0.84c_{HB} + 0.47c_{HWB} - 0.02c_{uW} - 0.05c_{uB}$	245000	✓
	2	$-0.96c_{HW} + 0.19c_{HB} - 0.20c_{HWB} + 0.02c_{uB}$	33	✓
	3	$-0.08c_{HW} + 0.50c_{HB} + 0.86c_{HWB} + 0.07c_{HDD} + 0.03c_{uW} + 0.06c_{uB}$	4	✓
	4	$0.03c_{HWB} - 0.85c_{HDD} + 0.32c_{uW} + 0.43c_{uB}$	0.017	
	5	$-0.01c_{HW} + 0.07c_{HB} + 0.05c_{HWB} - 0.44c_{HDD} - 0.86c_{uW} - 0.23c_{uB}$	0.0077	
	6	$-0.01c_{HW} + 0.06c_{HB} + 0.04c_{HWB} - 0.29c_{HDD} + 0.39c_{uW} - 0.87c_{uB}$	0.0025	
$c^{[i]}_{HG,uG,uH,\mathrm{top}}$	1	$+0.999c_{HG} + 0.038c_{uG}$	176000	✓
	2	$-0.03c_{HG} + 0.73c_{uG} - 0.03c^{(1)}_{qq} - 0.23c_{qq} - 0.05c^{(3)}_{qq} - 0.54c^{(31)}_{qq} - 0.02c_{uu} - 0.24c^{(1)}_{uu} - 0.04c^{(8)}_{ud} - 0.01c^{(1)}_{qu} - 0.15c^{(8)}_{qu} - 0.04c^{(8)}_{qd} - 0.18c_G + 0.06c_{uH}$	20	✓
	3	$-0.03c_{HG} + 0.67c_{uG} + 0.04c^{(1)}_{qq} + 0.25c_{qq} + 0.05c^{(3)}_{qq} + 0.55c^{(31)}_{qq} + 0.02c_{uu} + 0.26c^{(1)}_{uu} + 0.03c^{(8)}_{ud} + 0.01c^{(1)}_{qu} + 0.16c^{(8)}_{qu} + 0.03c^{(8)}_{qd} + 0.29c_G + 0.1c_{uH}$	1.3	✓
	4	$+0.11c_{uG} + 0.01c_{qq} - 0.018c^{(3)}_{qq} + 0.029c^{(31)}_{qq} + 0.012c^{(1)}_{uu} - 0.993c_{uH}$	0.14	
	5	$+0.02c_{qq} - 1.0c^{(3)}_{qq} + 0.06c^{(31)}_{qq} + 0.03c^{(1)}_{uu} + 0.02c^{(8)}_{qu} + 0.02c_{uH}$	0.02	
	6	$+0.07c_{uG} - 0.02c^{(1)}_{qq} + 0.07c_{qq} + 0.03c^{(3)}_{qq} + 0.32c^{(31)}_{qq} + 0.06c^{(1)}_{uu} + 0.04c^{(8)}_{ud} + 0.08c^{(8)}_{qu} + 0.04c^{(8)}_{qd} - 0.94c_G + 0.02c_{uH}$	0.0092	
$c^{[1]}_{Hl^{(1)},He}$		$+0.78c^{(1)}_{Hl} - 0.62c_{He}$	2.6	✓
$c^{[2]}_{Hl^{(1)},He}$		$+0.62c^{(1)}_{Hl} + 0.78c_{He}$	0.056	
$c^{[1]}_{Hu,Hd,Hq^{(1)}}$		$-0.87c_{Hu} + 0.26c_{Hd} + 0.42c^{(1)}_{Hq}$	59	✓
$c^{[2]}_{Hu,Hd,Hq^{(1)}}$		$+0.41c_{Hu} - 0.09c_{Hd} + 0.91c^{(1)}_{Hq}$	0.10	
$c^{[3]}_{Hu,Hd,Hq^{(1)}}$		$-0.28c_{Hu} - 0.96c_{Hd} + 0.03c^{(1)}_{Hq}$	0.0018	
$c^{[1]}_{Hl^{(3)},ll'}$		$0.87c^{(3)}_{Hl} - 0.50c'_{ll}$	27	✓
$c^{[2]}_{Hl^{(3)},ll'}$		$0.50c^{(3)}_{Hl} + 0.87c'_{ll}$	0.33	

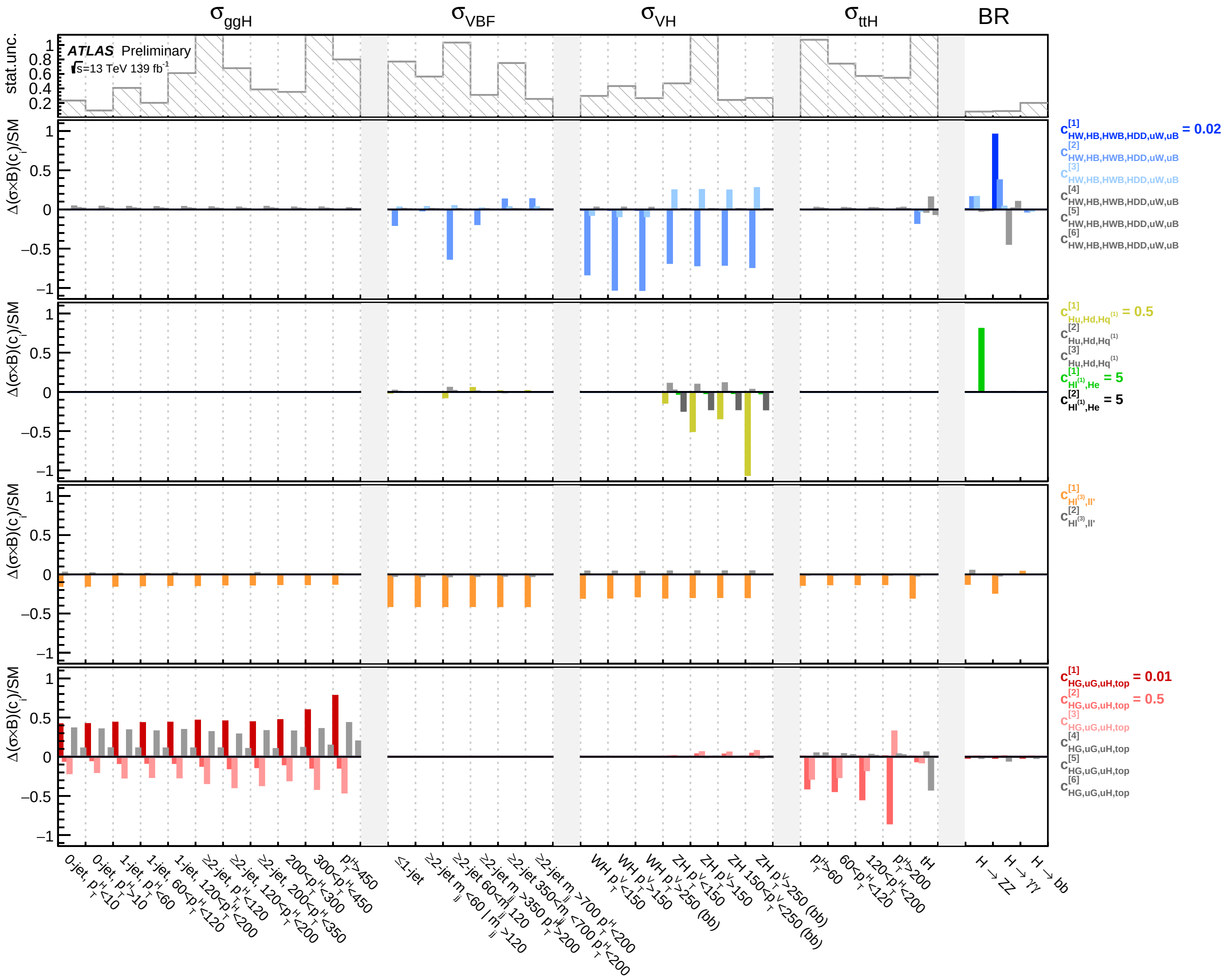

Figure 7: Impact of coefficients of the rotated basis c'_j on the STXS regions and decay modes, relative to the SM cross-section, under the assumption of the linearized SMEFT model. For all coefficients c'_j a unit variation is considered, unless specified otherwise in the legend. Additional eigenvectors that are not part of the fit basis are shown in gray for completeness. Scales and groupings in this figure are consistent with those in Fig. 3. To judge the experimental sensitivity to constrain the operators from the data in the listed STXS regions, the statistical uncertainty on the corresponding regions (σ_{stat}) is shown in the top panel. For columns corresponding to multiple STXS×BR regions, the shown uncertainty reflects the statistical uncertainty on the average, under the assumption of uncorrelated statistical uncertainties. For presentational clarity, the statistical uncertainty of low precision STXS regions is clipped in the plot.

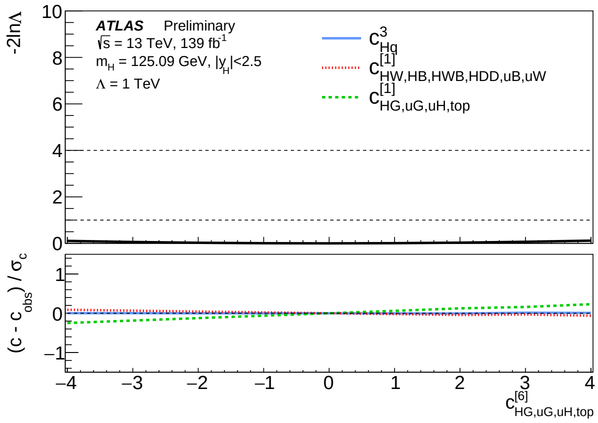

(a)

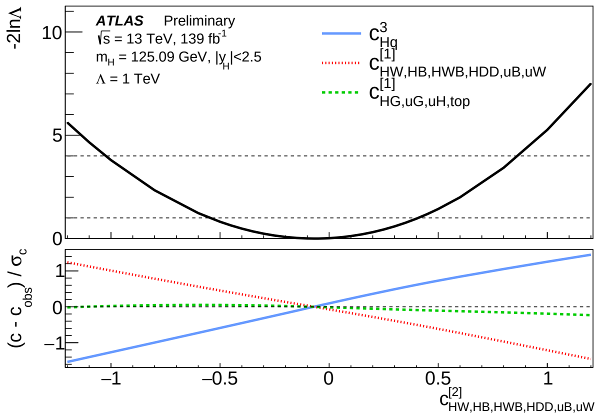

(b)

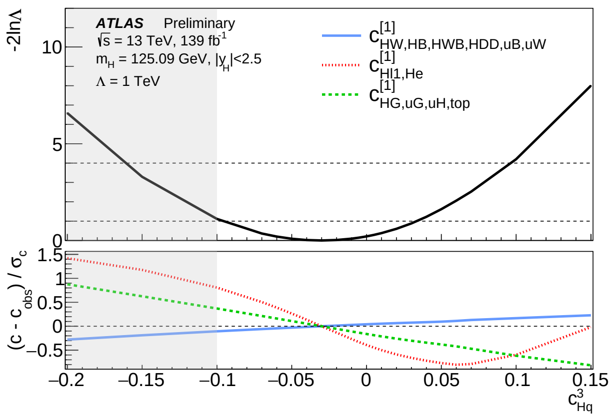

(c)

Figure 8: Scans of the profile likelihood of the linear SMEFT model over various parameters. For each scan, the pull of selected other parameters is shown on the same scale. The lower and upper horizontal dashed lines represent the threshold for the profile likelihood ration corresponding to 1 σ and 2 σ confidence intervals respectively. The scan of the weak eigenvector $c^{[6]}_{HG,uG,uH,\text{top}}$ (a) is representative of most scans of approximately flat directions, which are fixed in the fit. The scan of $c^{[2]}_{HW,HB,HWB,HDD,uW,uB}$ (b) is representative of most scans of parameters included in the final fit, illustrating linear correlations with other parameters of interest in a wide scan range. The scan of $c^{(3)}_{Hq}$ (c) illustrates one of the few non-linear correlation effects observed, in this case caused by a residual effect of the $H \to ZZ$ acceptance correction. The shaded region indicates the parameter space where one or more observable bins have negative predicted signal cross-section.

4.2 Results

The observed and the SM expected constraints on the parameters c'_j using the linearised SMEFT model, and the SMEFT model with additional quadratic terms are summarised in Tables 5 and 6, and visualized in Figures 9, 10 and 13. All measured parameters are consistent with the SM expectation within their uncertainty.

One-dimensional profile likelihood scans in each c'_j, profiled over all other c'_j, are shown in Figures 11 and 12 for the expected and observed data. All scanned parameters for the linearized model exhibit Gaussian behaviour to good approximation, except for $c^{[1]}_{Hl^{(1)},He}$, which is affected by the non-linear acceptance correction effects in the $H \rightarrow ZZ^* \rightarrow 4\ell$ decay channel that dominates the measurement of this coefficient.

The profile likelihood for the model including quadratic terms sometimes results in two local minima per parameter, notably for $c^{[1]}_{HW,HB,HWB,HDD,uW,uB}$ and $c^{[3]}_{HG,uG,uH,\mathrm{top}}$, and to a lesser extent $c^{(3)}_{Hq}$, and generally result in rather non-Gaussian likelihood scans for that reason. Despite this, constraints obtained from the model including quadratic terms are generally somewhat tighter than those obtained from the linearized model, suggesting a non-negligible influence of $d = 6$ operator terms suppressed by power Λ^{-4}.

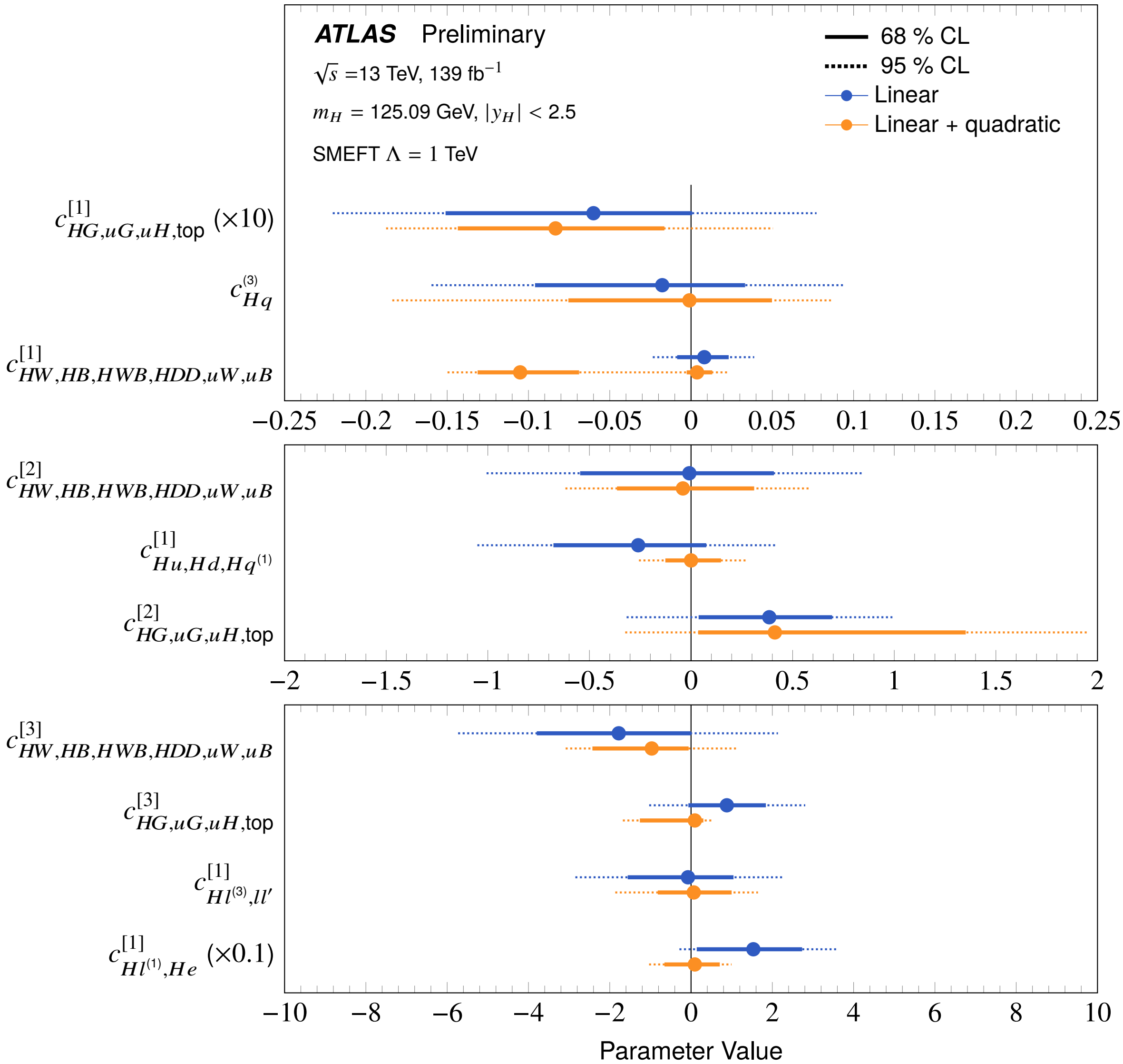

Figure 9: Summary of observed measurements of the parameters c_i' with the SMEFT linearized model (blue) and the SMEFT model with additional quadratic terms (orange). The ranges shown correspond to 68% (solid) and 95% (dashed) confidence level intervals, where all other coefficients and all nuisance parameters were profiled. For the model with quadratic terms, two exactly degenerate solutions are found for $c^{[1]}_{HW,HB,HWB,HDD,uW,uB}$, which are both indicated.

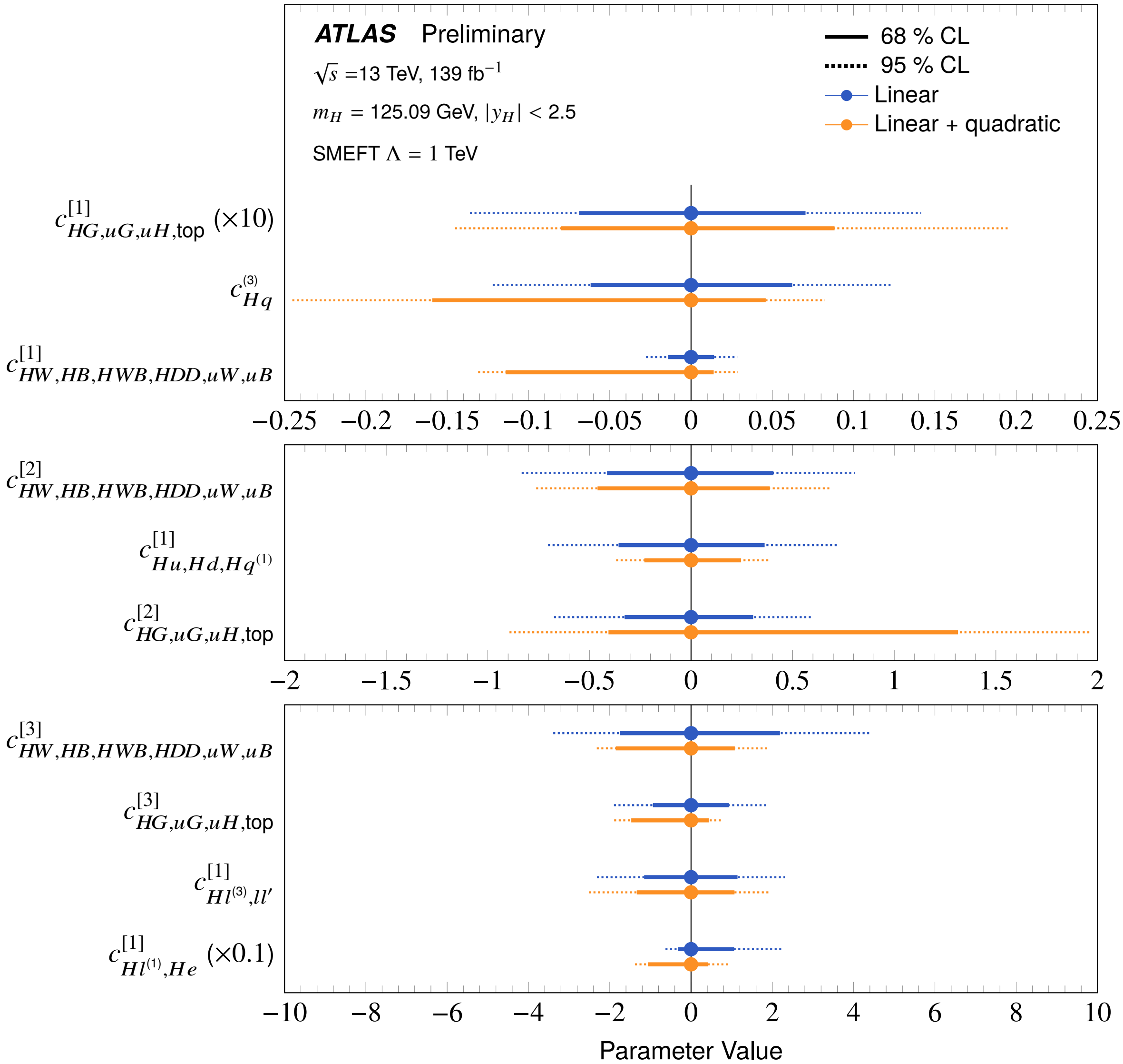

Figure 10: Summary of SM expected measurements of the parameters c_i' with the SMEFT linearized model (blue) and the SMEFT model with additional quadratic terms (orange). The ranges shown correspond to 68% (solid) and 95% (dashed) confidence level intervals, where all other coefficients and all nuisance parameters were profiled.

Table 5: Summary of the observed measurement of the parameters c_i' with the SMEFT linearized model and the SMEFT model with additional quadratic terms. The ranges correspond to 68% and 95% confidence level intervals, where all other coefficients and all nuisance parameters were profiled.

Model Parameter	Linear Model			Quadratic Model		
	Measured value	68% CI	95% CI	Measured value	68% CI	95% CI
$c^{[1]}_{HG,uG,uH,\text{top}}$	−0.006	[−0.015, 0.00007]	[−0.022, 0.008]	−0.008	[−0.014, −0.0016]	[−0.019, 0.005]
$c^{[2]}_{HG,uG,uH,\text{top}}$	0.4	[0.04, 0.7]	[−0.32, 1]	0.4	[0.04, 1.4]	[−0.32, 2.0]
$c^{[3]}_{HG,uG,uH,\text{top}}$	0.9	[−0.07, 1.8]	[−1.0, 2.8]	0.09	[−1.3, 0.30]	[−1.7, 0.5]
$c^{[1]}_{HW,HB,HWB,HDD,uW,uB}$	0.008	[−0.009, 0.023]	[−0.024, 0.04]	−0.1,0.004	[−0.13, −0.07]∧ [−0.0027, 0.013]	[−0.15, 0.023]
$c^{[2]}_{HW,HB,HWB,HDD,uW,uB}$	−0.008	[−0.5, 0.4]	[−1.0, 0.9]	−0.04	[−0.4, 0.31]	[−0.6, 0.6]
$c^{[3]}_{HW,HB,HWB,HDD,uW,uB}$	−1.8	[−4, 0.00020]	[−6, 2.1]	−1	[−2.4, −0.06]	[−3, 1.2]
$c^{(3)}_{Hq}$	−0.018	[−0.1, 0.033]	[−0.16, 0.09]	−0.001	[−0.08, 0.05]	[−0.18, 0.09]
$c^{[1]}_{Hu,Hd,Hq^{(1)}}$	−0.26	[−0.7, 0.07]	[−1.1, 0.4]	0	[−0.13, 0.15]	[−0.26, 0.27]
$c^{[1]}_{Hl^{(3)},ll'}$	−0.08	[−1.6, 1.0]	[−2.8, 2.3]	0.07	[−0.8, 1]	[−1.9, 1.6]
$c^{[1]}_{Hl^{(1)},He}$	15	[1.4, 27]	[−2.9, 36]	0.9	[−7, 7]	[−10, 10]

Table 6: Summary of the SM expected measurement of the parameters c'_i with the SMEFT linearized model and the SMEFT model with additional quadratic terms. The ranges correspond to 68% and 95% confidence level intervals, where all other coefficients and all nuisance parameters were profiled.

Model Parameter	Linear Model		Quadratic Model	
	68% CI	95% CI	68% CI	95% CI
$c^{[1]}_{HG,uG,uH,\mathrm{top}}$	[−0.007, 0.007]	[−0.014, 0.014]	[−0.008, 0.009]	[−0.015, 0.020]
$c^{[2]}_{HG,uG,uH,\mathrm{top}}$	[−0.33, 0.3]	[−0.7, 0.6]	[−0.4, 1.3]	[−0.9, 2.0]
$c^{[3]}_{HG,uG,uH,\mathrm{top}}$	[−0.9, 0.9]	[−1.9, 1.9]	[−1.5, 0.4]	[−1.9, 0.8]
$c^{[1]}_{HW,HB,HWB,HDD,uW,uB}$	[−0.014, 0.014]	[−0.028, 0.028]	[−0.11, 0.014]	[−0.13, 0.029]
$c^{[2]}_{HW,HB,HWB,HDD,uW,uB}$	[−0.4, 0.4]	[−0.8, 0.8]	[−0.5, 0.4]	[−0.8, 0.7]
$c^{[3]}_{HW,HB,HWB,HDD,uW,uB}$	[−1.7, 2.2]	[−3.4, 4]	[−1.9, 1.1]	[−2.3, 1.9]
$c^{(3)}_{Hq}$	[−0.06, 0.06]	[−0.12, 0.12]	[−0.16, 0.05]	[−0.25, 0.08]
$c^{[1]}_{Hu,Hd,Hq^{(1)}}$	[−0.4, 0.4]	[−0.7, 0.7]	[−0.23, 0.25]	[−0.4, 0.4]
$c^{[1]}_{Hl^{(3)},ll'}$	[−1.2, 1.1]	[−2.3, 2.3]	[−1.3, 1.1]	[−2.5, 1.9]
$c^{[1]}_{Hl^{(1)},He}$	[−3.2, 11]	[−6, 23]	[−11, 4]	[−14, 9]

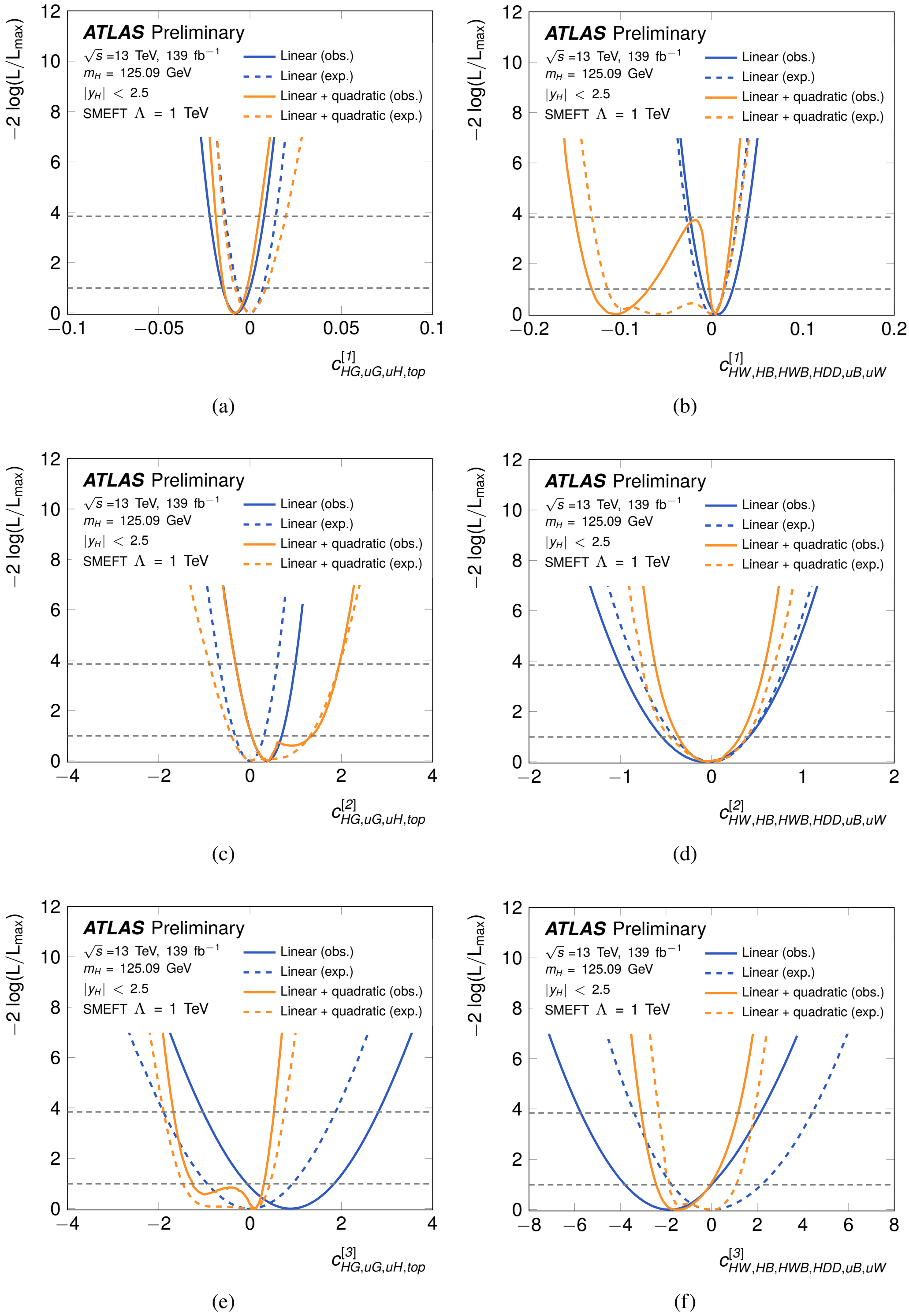

Figure 11: Profile likelihood scans of the fitted coefficients c'_j on SM expected and observed data, comparing the SMEFT linearized model (blue) and the SMEFT linear plus quadratic model (orange). The horizontal dashed lines in each plot correspond to the asymptotic threshold values for 68% and 95% confidence intervals. Profile likelihood scans of the linear plus quadratic model can exhibit 2 minima in the scanned parameter, whereas scans of the linearized model can only have one minimum per parameter. Multiple minima in the coefficients c'_j that are profiled in each scan may furthermore result in discontinuous derivatives in the profile likelihood (e.g. prominently visible in the observed data in (c)).

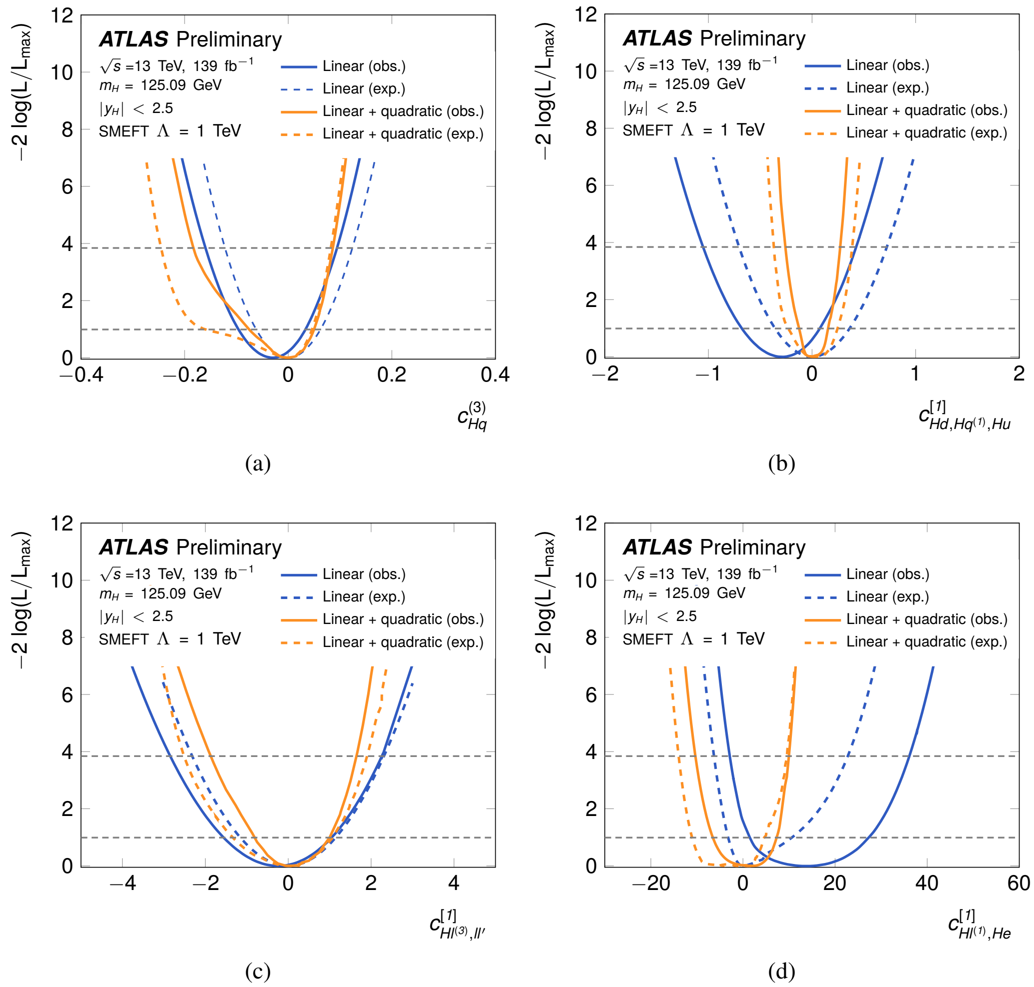

Figure 12: Profile likelihood scans of the fitted coefficients c'_j on SM expected and observed data, comparing the SMEFT linearized model (blue) and the SMEFT linear plus quadratic model (orange). The horizontal dashed lines in each plot correspond to the asymptotic threshold values for 68% and 95% confidence intervals. Profile likelihood scans of the linear plus quadratic model can exhibit 2 minima in the scanned parameter, whereas scans of the linearized model can only have one minimum per parameter. Multiple minima in the coefficients c'_j that are profiled in each scan may furthermore result in discontinuities in the profile likelihood.

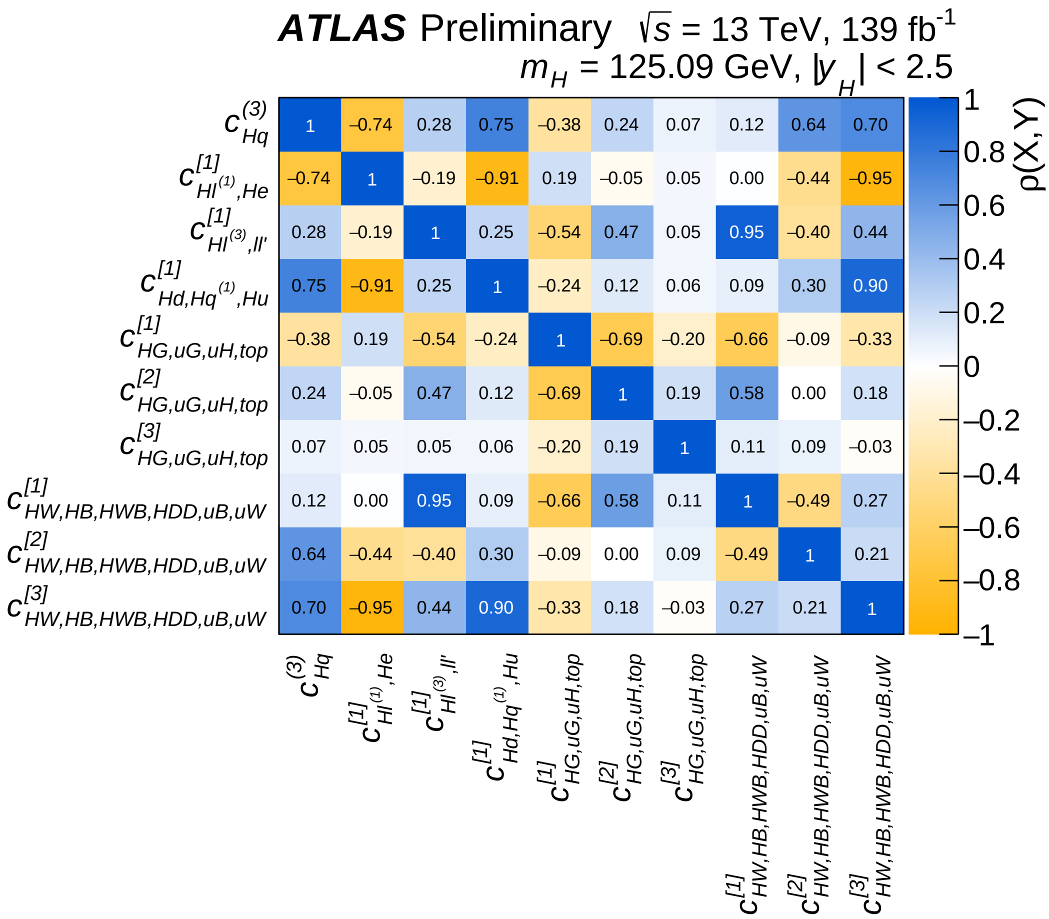

	$c_{Hq}^{(3)}$	$c^{[1]}_{Hl^{(1)},He}$	$c^{[1]}_{Hl^{(3)},ll'}$	$c^{[1]}_{Hd,Hq^{(1)},Hu}$	$c^{[1]}_{HG,uG,uH,top}$	$c^{[2]}_{HG,uG,uH,top}$	$c^{[3]}_{HG,uG,uH,top}$	$c^{[1]}_{HW,HB,HWB,HDD,uB,uW}$	$c^{[2]}_{HW,HB,HWB,HDD,uB,uW}$	$c^{[3]}_{HW,HB,HWB,HDD,uB,uW}$
$c_{Hq}^{(3)}$	1	–0.74	0.28	0.75	–0.38	0.24	0.07	0.12	0.64	0.70
$c^{[1]}_{Hl^{(1)},He}$	–0.74	1	–0.19	–0.91	0.19	–0.05	0.05	0.00	–0.44	–0.95
$c^{[1]}_{Hl^{(3)},ll'}$	0.28	–0.19	1	0.25	–0.54	0.47	0.05	0.95	–0.40	0.44
$c^{[1]}_{Hd,Hq^{(1)},Hu}$	0.75	–0.91	0.25	1	–0.24	0.12	0.06	0.09	0.30	0.90
$c^{[1]}_{HG,uG,uH,top}$	–0.38	0.19	–0.54	–0.24	1	–0.69	–0.20	–0.66	–0.09	–0.33
$c^{[2]}_{HG,uG,uH,top}$	0.24	–0.05	0.47	0.12	–0.69	1	0.19	0.58	0.00	0.18
$c^{[3]}_{HG,uG,uH,top}$	0.07	0.05	0.05	0.06	–0.20	0.19	1	0.11	0.09	–0.03
$c^{[1]}_{HW,HB,HWB,HDD,uB,uW}$	0.12	0.00	0.95	0.09	–0.66	0.58	0.11	1	–0.49	0.27
$c^{[2]}_{HW,HB,HWB,HDD,uB,uW}$	0.64	–0.44	–0.40	0.30	–0.09	0.00	0.09	–0.49	1	0.21
$c^{[3]}_{HW,HB,HWB,HDD,uB,uW}$	0.70	–0.95	0.44	0.90	–0.33	0.18	–0.03	0.27	0.21	1

Figure 13: Correlation matrix for the linearized SMEFT model for the observed data.

5 Methodology of MSSM interpretations

Supersymmetry (SUSY) [85–93], a theoretically motivated framework for extending the Standard Model, is conceived to address some of the Standard Model's unanswered questions, particularly the hierarchy problem [94–97], which is related to the fine tuning needed to obtain the correct mass for the observed Higgs boson. SUSY can also provide credible dark matter candidates [98, 99] and can improve the unification of the electroweak and strong interactions [100–108].

The minimal supersymmetric extension of the Standard Model (MSSM) [109–113] predicts partners for each of the SM states. There are a total of eight spin-half partners of the electroweak gauge and Higgs bosons: the neutral bino (superpartner of the U(1) gauge field); the winos, which are a charged pair and a neutral particle (superpartners of the W bosons of the SU(2) L gauge fields), and the Higgsinos, which are two neutral particles and a charged pair (superpartners of the Higgs field's degrees of freedom). The Higgs sector consists of two SU(2) doublets, H_1 and H_2. Both Higgs doublets acquire vacuum expectation values, v_1 and v_2 respectively. Their ratio is denoted by $\tan\beta \equiv v_2/v_1$, and they satisfy $v_1^2 + v_2^2 = v^2 \approx (246\,\text{GeV})^2$. Five Higgs bosons are predicted in the MSSM: two neutral CP-even bosons h and H, one neutral CP-odd boson A, and two charged bosons $H^{\pm}$.

In addition to searches for MSSM particles, such as additional Higgs bosons, evidence for the MSSM, or constraints on its parameters can also be obtained from studies of the properties of the $h(125)$ under the assumption that it is the light CP-even h boson of the theory.

The MSSM has over a hundred parameters that describe the pattern of sparticle masses and their decays. This parameter space is too large to be scanned exhaustively and compared to ATLAS data. Hence, several benchmark scenarios have been proposed over the years. By making some assumptions, the scenarios reduce the parameter space and simplify the interpretations of the results.

5.1 MSSM Benchmark Scenarios

In this study, properties of the measured of the 125 GeV Higgs boson are compared to six MSSM benchmark scenarios, under the assumption that the observed boson is the light CP-even Higgs boson h of the MSSM theory. In each benchmark scenario the compatibility of the scenario with the observed Higgs data is tested for a range of benchmark parameter values. For all scenarios, two benchmark parameters are considered: m_A and $\tan\beta$.

The six benchmarks are summarized below. Detailed information on the models and on their specific parameter settings can be found in Refs. [24, 25].

1. $\boldsymbol{M_h^{125}}$ **scenario:** All superparticles are chosen to be so heavy that production and decays of the MSSM Higgs bosons are only mildly affected by their presence. The loop-induced SUSY contribution to the couplings of the light CP-even scalar are small, and the heavy Higgs bosons with masses up to 2 TeV decay only to SM particles.

2. $\boldsymbol{M_h^{125}(\tilde{\chi})}$ **scenario:** All charginos and neutralinos are relatively light, with significant higgsino-gaugino mixing. This affects the decays of the heavier Higgs bosons, weakening the exclusion bounds from $H/A \to \tau\tau$ searches, as well as the decay of the SM-like Higgs boson to photons. On the other hand, the possibility to look for additional Higgs bosons through their decays to charginos and neutralinos opens up.

3. **$M_h^{125}(\tilde{\tau})$ scenario:** Light staus and light gaugino-like charginos and neutralinos. The effect of the light staus on the decays of the heavier Higgs bosons, as well as on the decay of the SM-like Higgs boson to photons, is most relevant at large $\tan\beta$. Compared with the previous scenario, a larger mass for the higgsinos implies that the decays of the heavier Higgs bosons to charginos and neutralinos become relevant at larger values of M_A.

4. **M_h^{125}(alignment) scenario:** In the "alignment without decoupling" scenario, for a given value of $\tan\beta$, one of the two neutral CP-even scalars has SM-like couplings independently of the mass spectrum of the remaining Higgs bosons. In particular, for $\tan\beta$ around 7 the properties of the lighter scalar h are in agreement with those of the observed Higgs boson also for relatively low values of M_A.

5. **$M_{h,\mathrm{EFT}}^{125}$ scenario:** This scenario is characterized by a flexible mass scale M_{SUSY} of the superpartners. In all the original benchmark scenarios presented above, the supersymmetric partners of the SM fermions (sfermions) are tied to the TeV scale. In this case, the parameter region $\tan\beta < 5$ is ruled out because the mass M_h of the SM-like Higgs boson is predicted to be lower than the measured value. To re-open the parameter region of low $\tan\beta$ values, the sfermion mass scale, M_{SUSY} is adjusted dynamically from 6 TeV to 10^{16} TeV to achieve a 125 GeV Higgs. As in this scenario all superparticles are chosen to be so heavy that production and decays of the MSSM Higgs bosons are only mildly affected by their presence, the SUSY contribution to the Higgs properties is calculated with an effective field theory (EFT).

6. **$M_{h,\mathrm{EFT}}^{125}(\tilde{\chi})$ scenario:** In contrast to the $M_{h,\mathrm{EFT}}^{125}$ scenario, this scenario features light neutralinos and charginos whose presence significantly alters the phenomenology of the Higgs boson. The SUSY scale is again adjusted at every parameter point in order to obtain a light Higgs mass of $M_h \approx 125$ GeV.

5.2 Interpretation of Higgs data

For each MSSM benchmark point modified Higgs production cross sections and decay branching fractions are predicted. Higgs masses and mixing (and effective Yukawa couplings) have been calculated with FeynHiggs [114–120]. Branching ratio predictions combine the most precise estimates of FeynHiggs, HDECAY [121, 122] and PROPHECY4f [123, 124]. For the gluon-fusion process inclusive cross sections are obtained with SusHi [125, 126], which includes NLO QCD corrections [127], NNLO QCD corrections for the top-quark contribution in the effective theory of a heavy top quark [128–132] and electroweak effects by light quarks [133, 134]. For the SM-like Higgs boson SusHi adds N3LO corrections in the effective theory of a heavy top quark in a threshold expansion [41, 135, 136]. Cross sections for bottom-quark initiated Higgs production rely on matched predictions [137–140], which are based on the five flavour NNLO QCD calculation [61] and the four flavour NLO QCD calculation [59, 60].

Since MSSM Higgs production cross sections are only calculated inclusively, the STXS Stage-1.2 phase space partitioning of production cross sections is not used in this analysis. Instead a splitting by production process is used to express the signal strength modifies $\mu^{i,X}$ in the signal yield expression of Eq. (2):

$$\mu^{i,X}(m_A, \tan\beta) = \frac{\sigma^i(m_A, \tan\beta)}{\sigma^i_{\mathrm{SM}}} \cdot \frac{B^X(m_A, \tan\beta)}{B^X_{\mathrm{SM}}} \equiv r^i(m_A, \tan\beta) \cdot r^X(m_A, \tan\beta), \qquad (21)$$

where the index i enumerates the STXS-0 production processes: ggH, $b\bar{b}H$, $t\bar{t}H$, VBF, $qq/qg{\to}ZH$, $gg{\to}ZH$, $qq{\to}WH$, as defined in Table 2. All nine analyses listed in Table 1 are available in STXS-0 form and allow to measure Higgs decays to WW, ZZ, bb, $\tau\tau$, $\mu\mu$, $\gamma\gamma$, enumerated by index X in Eq. (21).

In this analysis, the numerical predictions provided for MSSM scenarios by the LHC Higgs Cross Section Working Group are used [141] for the benchmarks listed in Section 5.1, which provide all $B^X_{\mathrm{MSSM}}(m'_h)$ and the inclusive Higgs widths $\Gamma^{h\to X}_{\mathrm{MSSM}}(m'_h)$, where m'_h is the mass of the light CP-even Higgs boson h predicted by the MSSM and may differ somewhat from the assumed SM value of 125.09 GeV. However, regions of the benchmark parameter space where m'_h differs from the assumed SM value by more than 3 GeV, the estimated uncertainty on the calculated Higgs mass in FeynHiggs [116, 142], will be considered as excluded.

For the cross-section scale factor for the ggH and $b\bar{b}H$ processes, the numeric cross sections predictions are used. Conversely, the MSSM cross sections for the $qq/qg{\to}VH$ and VBF processes are not provided. Instead, the cross-section scale factors for these are estimated from the corresponding relative change to the partial decay width Γ_V in the MSSM. The predictions for the $t(\bar{t})H$ and $gg{\to}ZH$ cross-section scale factors are obtained with a similar rescaling, using the square of the relative change in the coupling strengths in the MSSM. The expression for all MSSM cross-section productions are specified in Table 7, where all SM cross sections and partial widths are evaluated for a Higgs mass m'_h. These SM cross sections, as well as the partial widths, are provided by Ref. [141].

Table 7: Expressions used for STXS-0 production cross-sections in the MSSM interpretation. The Higgs couplings strength scale factor κ'_t is provided numerically, while the scale factors κ'_V, κ'_b are calculated from $\kappa'^2_i = \Gamma^{H\to i}_{\mathrm{MSSM}}(m'_h)/\Gamma^{h\to i}_{\mathrm{SM}}(m'_h)$.

STXS-0 Process	Expression for cross-section scale factor r^i
ggH	$\sigma^{\mathrm{MSSM}}_{\mathrm{ggH}}(m'_h)/\sigma^{\mathrm{SM}}_{\mathrm{ggH}}(m'_h)$
$b\bar{b}H$	$\sigma^{\mathrm{MSSM}}_{\mathrm{bbH}}(m'_h)/\sigma^{\mathrm{SM}}_{\mathrm{bbH}}(m'_h)$
VBF	$0.73\kappa'^2_W + 0.27\kappa'^2_Z$
$qq/qg{\to}VH$	κ'^2_V
$t\bar{t}H$	κ'^2_t
$gg{\to}ZH$	$2.456\kappa'^2_Z + 0.456\kappa'^2_t - 1.903\kappa'_Z\kappa'_t - 0.011\kappa'_Z\kappa'_b + 0.003\kappa'_t\kappa'_b$
tHW	$2.909\kappa'^2_t + 2.310\kappa'^2_W - 4.220\kappa'_t\kappa'_W$
tHq	$2.633\kappa'^2_t + 3.578\kappa'^2_W - 5.211\kappa'_t\kappa'_W$

All branching ratios scale factors r^X are calculated as

$$r^X = \frac{\Gamma^{h\to X}_{\mathrm{MSSM}}(m'_h)}{\Gamma^{h\to X}_{\mathrm{SM}}(m'_h)} \cdot \frac{\Gamma^h_{\mathrm{SM}}(m'_h)}{\Gamma^h_{\mathrm{MSSM}}(m'_h)}. \quad (22)$$

As the cross section and branching ratio scale factors r^i, r^X are only calculated for a discrete set of points in the 2-dimensional benchmark parameter space, a likelihood based on Eq. (21) and the expressions in Table 7 cannot be differentially expressed in terms of its theory parameters ($m_A, \tan\beta$). Instead, exclusion contours are based on a numerical interpolation of the profile likelihood ratio at fixed values of ($m_A, \tan\beta$), profiling only the nuisance parameters.

6 Limits on MSSM

Figure 14 shows the observed and expected 95% CL exclusion limits of the MSSM in the two-dimensional plane of m_A and $\tan\beta$ for the M_h^{125}, $M_h^{125}(\tilde{\chi})$, $M_h^{125}(\tilde{\tau})$, M_h^{125}(alignment) benchmark scenarios. For all four scenarios, the regions excluded by the Higgs mass requirement ($|m'_h - 125.09$ GeV$| < 3$ GeV) are separately indicated with gray shaded areas.

In the M_h^{125} scenario, the low m_A region is disfavored due to the suppression of $h \to b\bar{b}$ in that region. In the $M_h^{125}(\tilde{\tau})$ scenario, the region at low m_A and $\tan\beta < 55$ is excluded due to a predicted significant enhancement of the Higgs width in combination with a suppression of the branching fraction $h \to \gamma\gamma$. In the region $\tan\beta > 55$, the $\tilde{\tau}$ loop has a significant impact on the hbb coupling, resulting in an enhanced prediction of BR($h \to \gamma\gamma$), and is therefore excluded. The observed exclusion range starts at a larger value of $\tan\beta$ than the expected exclusion range because the observed value of κ_γ is larger than one ($\kappa_\gamma = 1.06^{+0.08}_{-0.07}$) [9]) Similar to the $M_h^{125}(\tilde{\tau})$ scenario, in the $M_h^{125}(\tilde{\chi})$ scenario, low values of m_A are excluded due to the suppression of BR($h \to \gamma\gamma$). In the region with $\tan\beta < 10$, the enhancement of electroweakino effects and the absence of a $\tilde{\tau}$ loop will enhance BR($h \to \gamma\gamma$) but the resulting exclusion is less stringent than that of the m'_h mass requirement. In the M_h^{125}(alignment) scenario, the limit of alignment without decoupling is only realized for $\tan\beta \approx 7$ and $m_A > 170$ GeV. For larger values of m_A MSSM couplings are more similar to SM couplings causing the allowed region to open up.

In all four benchmarks the MSSM analysis generally excludes the low m_A regime for most of the scanned $\tan\beta$ range, while the requirement $|m'_h - 125.09| < 3$ GeV helps to exclude the low $\tan\beta$ range for all scanned values of m_A, which is not covered by the direct searches for MSSM $H/A \to \tau\tau$ [143] and $H^\pm \to tb$ [144].

Figure 15 shows the observed and expected 95% CL exclusion limits of the MSSM in the two-dimensional plane of m_A and $\tan\beta$ for the $M_{h,\text{EFT}}^{125}$ and $M_{h,\text{EFT}}^{125}(\tilde{\chi})$ scenarios. No results of direct searches are available for these benchmarks. No part of the parameter space is excluded by the condition $|m'_h - 125.09$ GeV$| < 3$ GeV for these benchmarks, as $m'_h = 125.09$ GeV can be achieved throughout the shown range of ($m_A, \tan\beta$) because of the flexible m_{SUSY} scale in these benchmarks.

For both the $M_{h,\text{EFT}}^{125}$ and $M_{h,\text{EFT}}^{125}(\tilde{\chi})$ scenarios, the limit at low m_A is driven by a predicted enhancement in $H \to b\bar{b}$ decays. In the $M_{h,\text{EFT}}^{125}(\tilde{\chi})$ scenario, the $H\to\gamma\gamma$ decay is enhanced in the $\tan\beta \lesssim 1.5$ region due to the presence of light charginos. As the observed coupling of the Higgs boson to photons slightly exceeds the expected value ($\kappa_\gamma = 1.06^{+0.08}_{-0.07}$), the constraint from $H\to\gamma\gamma$ is less strong than expected.

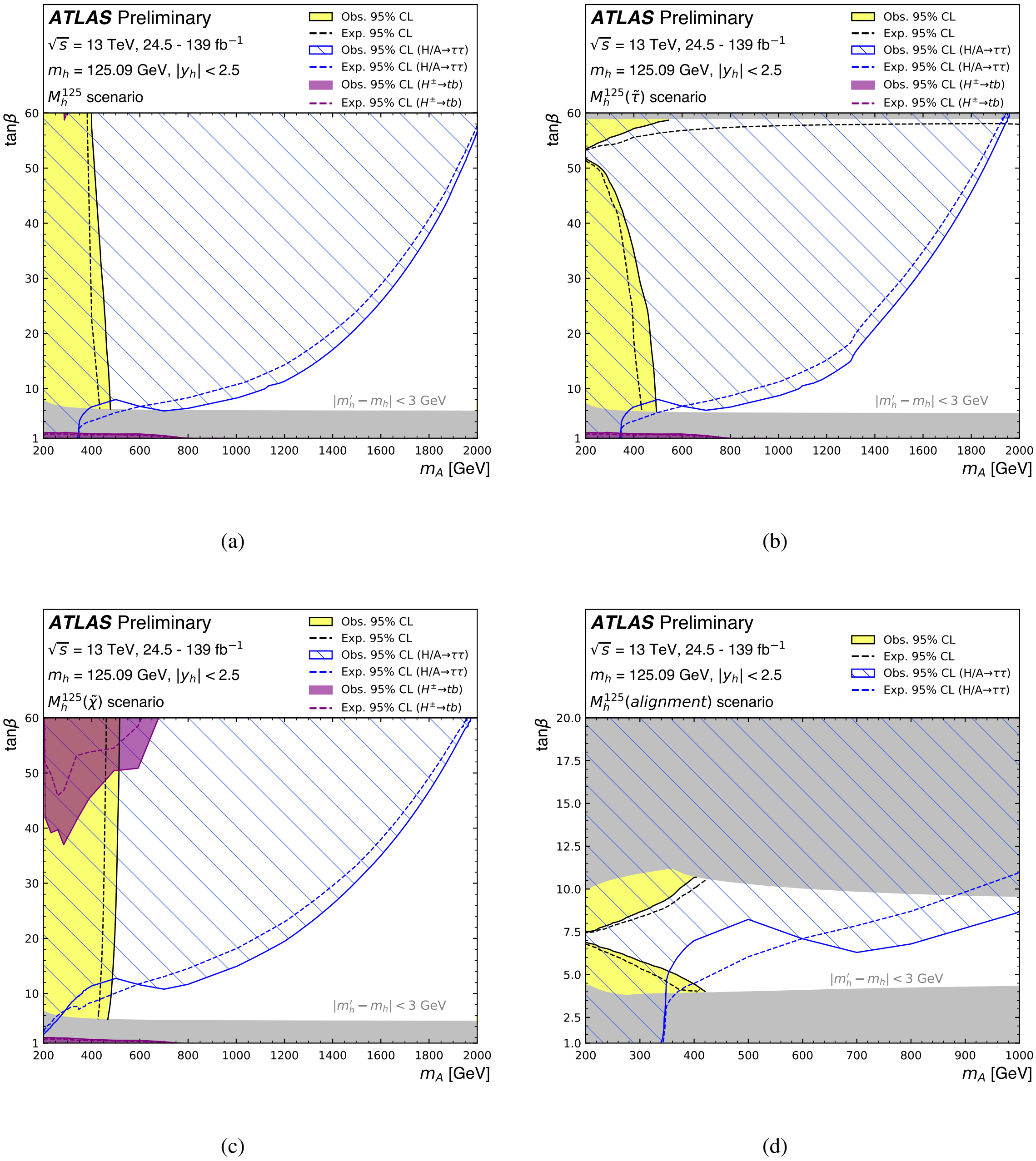

Figure 14: Exclusion contours in the $(m_A, \tan\beta)$ plane for (a) the M_h^{125}, (b) $M_h^{125}(\tilde{\tau})$, (c) $M_h^{125}(\tilde{\chi})$ and (d) M_h^{125}(alignment) scenarios. Observed (solid) and expected (dashed) contours at 95% C.L., defined as $-2\ln\Lambda = 5.99$ according to the asymptotic approximation, are shown. The excluded parameter space is marked in yellow. The parameter space excluded by the condition $|m_h' - 125.09| < 3$ GeV is marked in gray. For comparison, the parameter space excluded by the search for $H/A \to \tau\tau$ [143] and for $H^\pm \to t\bar{b}$ [144] are overlaid in blue and purple, respectively. For the M_h^{125}(alignment) scenario no exclusion limits from the search for $H^\pm \to t\bar{b}$ exist.

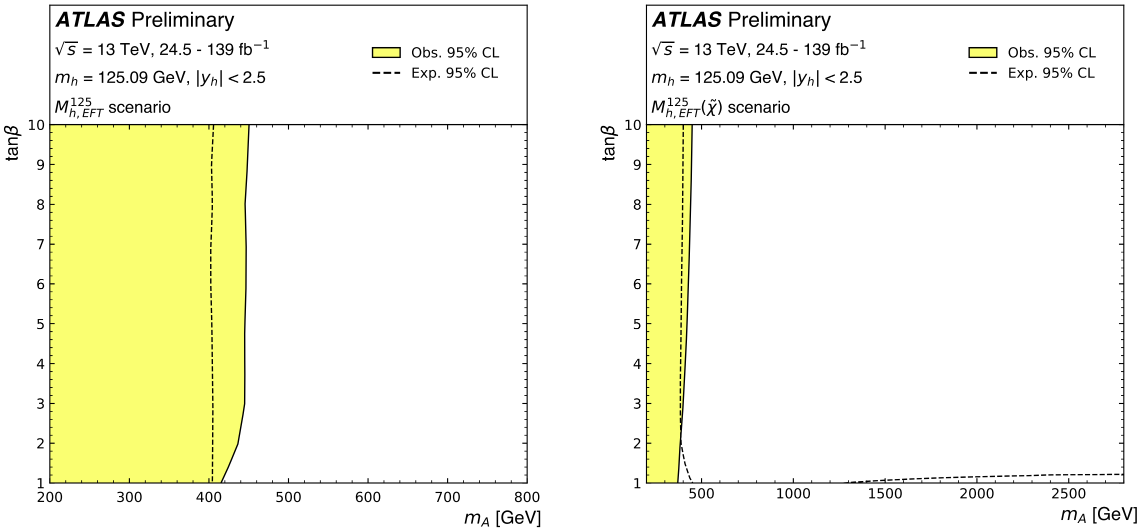

(a)

(b)

Figure 15: Exclusion contours in the $(m_A, \tan\beta)$ plane for the (a) $M^{125}_{h,\mathrm{EFT}}$ and (b) $M^{125}_{h,\mathrm{EFT}}(\tilde{\chi})$ scenarios. Observed (solid) and expected (dashed) contours at 95% C.L., defined as $-2\ln\Lambda = 5.99$ according to the asymptotic approximation, are shown. The excluded parameter space is marked in yellow.

7 Conclusions

Novel interpretations of the combined Higgs boson measurements recently presented by ATLAS have been performed. Constraints on linear combinations of Wilson coefficients corresponding to SM Effective Field Theory operators in the Warsaw basis are reported. In this model-independent parametrization of new physics effects, no significant deviations from the SM have been observed. A comparison of results interpreted with a linearized SMEFT model and a model that also includes quadratic terms shows sizeable sensitivity to operators suppressed by Λ^4 in all of the measured parameters. Constraints have also been set on the parameters $m_A, \tan\beta$ of the MSSM, in the context of six benchmark scenarios proposed by the BSM subgroup of the LHC Higgs Cross-Section WG. These results are complementary to limits from direct searches for additional Higgs bosons.

Appendix

A Additional material concerning the EFT interpretation

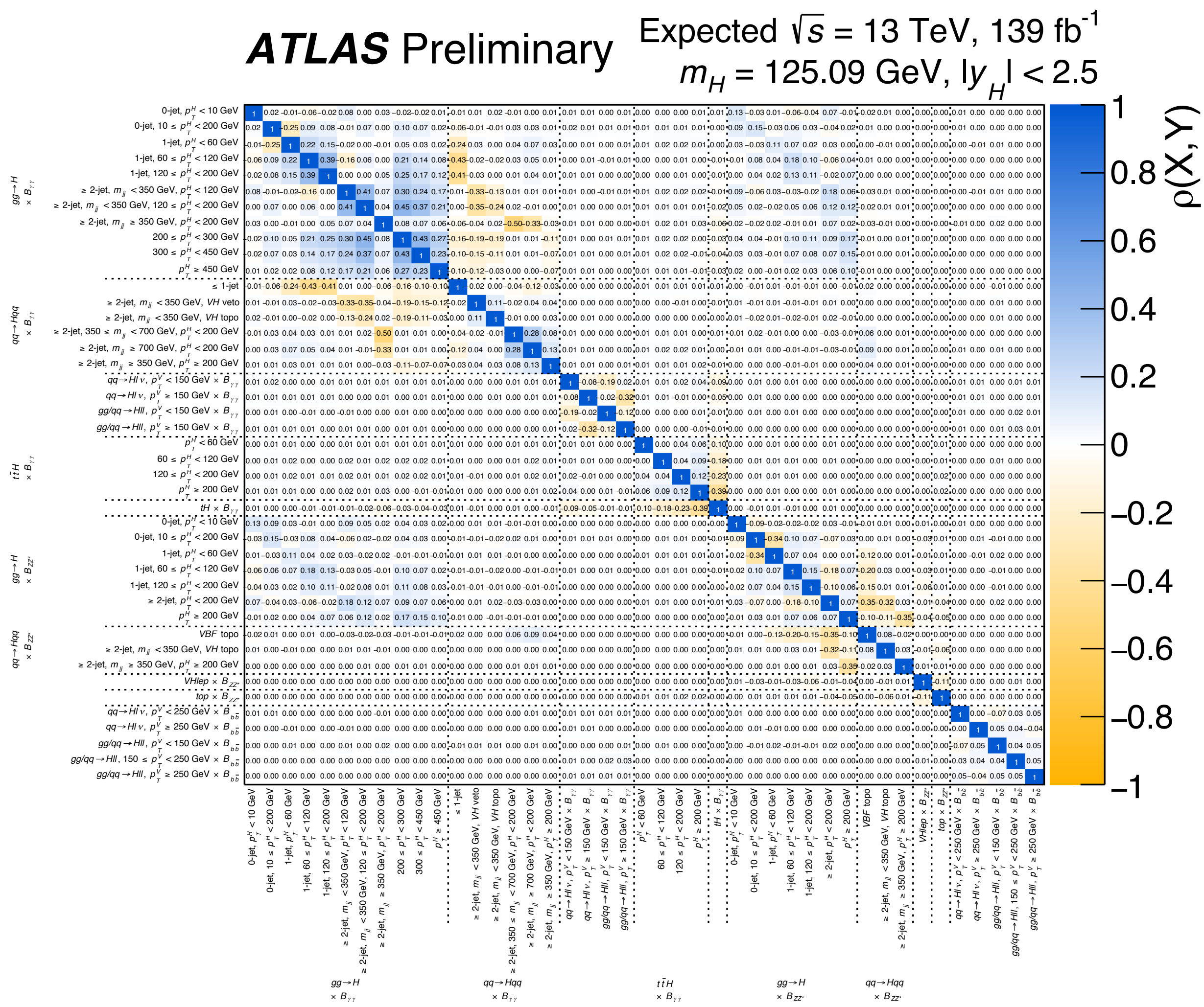

Figure 16: Correlation matrix corresponding to the expected measurements shown in Fig. 1.

Table 8: Eigenvectors of the inverse of the EFT covariance matrix of Eq. (19) with eigenvalues > 0.01. This eigenvalue limit corresponds to an approximate expected uncertainty on that eigenvector of > 10.

No.	Eigenvalue	Eigenvector
1	299310	$-0.02c_W + 0.55c_{HG} - 0.23c_{HW} - 0.70c_{HB} + 0.39c_{HWB} + 0.02c_{uG} - 0.02c_{uW} - 0.04c_{uB}$
2	121830	$-0.83c_{HG} - 0.15c_{HW} - 0.47c_{HB} + 0.26c_{HWB} - 0.03c_{uG} - 0.03c_{uB}$
3	1960	$0.10c_{HW} + 0.03c_{HWB} - 0.02c^{(3)}_{Hl} - 0.05c^{(1)}_{Hq} + 0.99c^{(3)}_{Hq} + 0.09c_{Hu} - 0.03c_{Hd} + 0.02c'_{ll}$
4	38	$+0.03c_{H\Box} + 0.02c_{HDD} + 0.09c_{HB} + 0.15c_{HWB} + 0.02c_{uH} + 0.08c_{uG} - 0.02c^{(1)}_{Hl} - 0.06c^{(3)}_{Hl} - 0.02c_{He} - 0.41c^{(1)}_{Hq} - 0.11c^{(3)}_{Hq} + 0.84c_{Hu} - 0.26c_{Hd} + 0.04c'_{ll}$
5	19	$+0.17c_G + 0.07c_{H\Box} + 0.02c_{HG} - 0.19c_{HW} + 0.10c_{HB} + 0.06c_{HWB} - 0.08c_{uH} + 0.06c_{dH} - 0.69c_{uG} + 0.09c^{(1)}_{Hl} - 0.13c^{(3)}_{Hl} - 0.07c_{He} - 0.02c^{(1)}_{Hq} + 0.03c_{Hu} + 0.10c'_{ll} + 0.03c^{(1)}_{qq} + 0.22c_{qq} + 0.05c^{(3)}_{qq} + 0.52c^{(31)}_{qq} + 0.02c_{uu} + 0.23c^{(1)}_{uu} + 0.03c^{(8)}_{ud} + 0.15c^{(8)}_{qu} + 0.03c^{(8)}_{qd}$
6	10	$-0.20c_{H\Box} - 0.02c_{HDD} - 0.57c_{HW} - 0.34c_{HWB} - 0.02c_{uH} - 0.08c_{dH} - 0.04c_{uG} - 0.13c^{(1)}_{Hl} + 0.54c^{(3)}_{Hl} + 0.13c_{He} - 0.10c^{(1)}_{Hq} + 0.08c^{(3)}_{Hq} + 0.08c_{Hu} - 0.02c_{Hd} - 0.40c'_{ll} + 0.02c_{qq} + 0.04c^{(31)}_{qq} + 0.02c^{(1)}_{uu}$
7	5.9	$+0.08c_G - 0.07c_{H\Box} - 0.03c_{HDD} + 0.73c_{HW} - 0.23c_{HB} - 0.11c_{dH} - 0.13c_{uG} - 0.02c_{uW} - 0.03c_{uB} - 0.15c^{(1)}_{Hl} + 0.44c^{(3)}_{Hl} + 0.10c_{He} - 0.07c^{(3)}_{Hq} + 0.08c_{Hu} - 0.02c_{Hd} - 0.25c'_{ll} + 0.09c_{qq} + 0.02c^{(3)}_{qq} + 0.22c^{(31)}_{qq} + 0.10c^{(1)}_{uu} + 0.06c^{(8)}_{qu}$
8	1.1	$-0.29c_G + 0.04c_{H\Box} - 0.02c_{HDD} + 0.03c_{HG} + 0.08c_{HW} - 0.02c_{HB} - 0.10c_{uH} - 0.68c_{uG} + 0.02c^{(1)}_{Hl} + 0.08c^{(3)}_{Hl} - 0.01c_{He} - 0.02c^{(1)}_{Hq} - 0.01c^{(3)}_{Hq} + 0.04c_{Hu} - 0.02c_{Hd} - 0.03c'_{ll} - 0.04c^{(1)}_{qq} - 0.24c_{qq} - 0.04c^{(3)}_{qq} - 0.52c^{(31)}_{qq} - 0.02c_{uu} - 0.25c^{(1)}_{uu} - 0.03c^{(8)}_{ud} - 0.01c^{(1)}_{qu} - 0.15c^{(8)}_{qu} - 0.03c^{(8)}_{qd}$
9	0.30	$+0.03c_G - 0.01c_W + 0.06c_{H\Box} - 0.12c_{HDD} + 0.09c_{HW} - 0.41c_{HB} - 0.70c_{HWB} + 0.06c_{uH} - 0.11c_{dH} - 0.05c_{uG} - 0.01c_{uW} - 0.02c_{uB} - 0.37c^{(3)}_{Hl} + 0.16c_{He} - 0.36c^{(1)}_{Hq} - 0.02c^{(3)}_{Hq} - 0.03c_{Hu} + 0.01c_{Hd} + 0.10c'_{ll}$
10	0.16	$+0.02c_G - 0.02c_W + 0.27c_{H\Box} - 0.04c_{HDD} - 0.09c_{HW} + 0.09c_{HB} + 0.09c_{HWB} + 0.01c_{eH} + 0.08c_{uH} - 0.52c_{dH} - 0.07c_{uG} - 0.01c_{uW} - 0.04c_{uB} - 0.58c^{(1)}_{Hl} - 0.26c^{(3)}_{Hl} + 0.29c_{He} + 0.31c^{(1)}_{Hq} + 0.10c_{Hu} - 0.12c'_{ll} - 0.04c^{(3)}_{qq}$
11	0.036	$+0.22c_G - 0.56c_{H\Box} + 0.19c_{HDD} + 0.01c_{HG} + 0.03c_{HW} + 0.03c_{HB} + 0.07c_{HWB} - 0.02c_{eH} + 0.70c_{uH} + 0.09c_{dH} - 0.16c_{uG} + 0.04c_{uW} - 0.01c_{uB} - 0.06c^{(1)}_{Hl} - 0.18c^{(3)}_{Hl} + 0.09c_{He} + 0.03c^{(1)}_{Hq} - 0.04c_{Hd} - 0.07c'_{ll} + 0.01c^{(1)}_{qq} - 0.01c_{qq} - 0.10c^{(3)}_{qq} - 0.09c^{(31)}_{qq} - 0.02c^{(1)}_{uu} - 0.01c^{(8)}_{ud} - 0.02c^{(8)}_{qu} - 0.01c^{(8)}_{qd}$
12	0.023	$-0.05c_G + 0.09c_{H\Box} - 0.01c_{HDD} - 0.01c_{HB} - 0.02c_{uH} + 0.01c_{uG} + 0.37c_{uW} + 0.03c^{(1)}_{Hl} + 0.05c^{(3)}_{Hl} - 0.02c_{He} - 0.03c^{(1)}_{Hq} - 0.01c_{Hu} + 0.03c'_{ll} + 0.03c_{qq} - 0.91c^{(3)}_{qq} + 0.08c^{(31)}_{qq} + 0.03c^{(1)}_{uu} + 0.02c^{(8)}_{qu}$

Table 9: Settings used in the MadGraph5_aMC@NLO generation. The parameters `drll`, `drjj`, `drbb`, and `drjb` describe the minimum radial difference between two leptons, jets, *b*-jets or a jet and a *b*-jet. The parameters `ptj`, `ptb`, `ptl`, and `etal` describe the minimum transverse momentum of a jet, *b*-jet, lepton, and the maximum pseudorapidity of a lepton.

Parameter	Value	Default	Comment
`lhaid`	90400 `PDF4LHC15_nlo_30_pdfas`	263000 `NNPDF30_lo_as_0130`	sets α_s to the default value assumed in the PDF fit (α_s = 0.118 for 90400)
`drll, drjj, drbb, drjb`	0.05	0.4	Avoid bias in the selection, minimum value of 0.05 chosen to avoid divergences.
`ptj, ptb`	20 GeV	20 GeV	Chosen to match jet selection of the Rivet routine.
`ptl`	0 GeV	10 GeV	Cut applied only to charged leptons.
`etal`	10	2.5	Cut applied only to charged leptons.
`ktdurham`	30 GeV	X	Merging scale for CKKW-L scheme. Recommended to be 1/4 of the relevant scale of the process. Settings propagated to Pythia.

Table 10: Parametrisation of the $gg \to H$ bins with 0- and N_{jets}=1 selection of the STXS as defined in its stage 1.2 with the parameter definitions of the SMEFTsim model. The numbers are rounded according to their statistical uncertainty. Dimensional quantities are printed in units of GeV.

Category in ggH $N_{\text{jets}} \leq 1$	**Parametrisation**
$200 < p_{\text{T}}^{H} < 300$	$0.12 c_{H\Box} - 0.030 c_{HDD} + 47 c_{HG} - 0.122 c_{uH} + 1.69 c_{uG} - 0.120 c_{Hl}^{(3)} + 0.058 c'_{ll}$
$300 < p_{\text{T}}^{H} < 450$	$0.12 c_{H\Box} - 0.029 c_{HDD} + 60 c_{HG} - 0.12 c_{uH} + 2.1 c_{uG} - 0.11 c_{Hl}^{(3)} + 0.055 c'_{ll}$
$450 < p_{\text{T}}^{H} < 650$	$0.12 c_{H\Box} - 0.030 c_{HDD} + 70 c_{HG} - 0.14 c_{uH} + 2. c_{uG} - 0.13 c_{Hl}^{(3)} + 0.07 c'_{ll}$
$p_{\text{T}}^{H} > 650$	$0.12 c_{H\Box} - 0.02 c_{HDD} + 200 c_{HG} - 0.05 c_{uH} + 10 c_{uG} - 0.07 c_{Hl}^{(3)} + 0.06 c'_{ll}$
$N_{\text{jets}}=0, p_{\text{T}}^{H} < 10$	$0.12 c_{H\Box} - 0.0294 c_{HDD} + 42.0 c_{HG} - 0.117 c_{uH} + 1.59 c_{uG} - 0.117 c_{Hl}^{(3)} + 0.0587 c'_{ll}$
$N_{\text{jets}}=0, p_{\text{T}}^{H} > 10$	$0.12 c_{H\Box} - 0.0295 c_{HDD} + 42.2 c_{HG} - 0.1186 c_{uH} + 1.62 c_{uG} - 0.1182 c_{Hl}^{(3)} + 0.0590 c'_{ll}$
$N_{\text{jets}}=1, p_{\text{T}}^{H} < 60$	$0.12 c_{H\Box} - 0.0330 c_{HDD} + 44.0 c_{HG} - 0.132 c_{uH} + 1.60 c_{uG} - 0.132 c_{Hl}^{(3)} + 0.065 c'_{ll}$
$N_{\text{jets}}=1, 60 < p_{\text{T}}^{H} < 120$	$0.12 c_{H\Box} - 0.0314 c_{HDD} + 43.5 c_{HG} - 0.125 c_{uH} + 1.58 c_{uG} - 0.125 c_{Hl}^{(3)} + 0.063 c'_{ll}$
$N_{\text{jets}}=1, 120 < p_{\text{T}}^{H} < 200$	$0.12 c_{H\Box} - 0.028 c_{HDD} + 44 c_{HG} - 0.118 c_{uH} + 1.60 c_{uG} - 0.112 c_{Hl}^{(3)} + 0.058 c'_{ll}$

Table 11: Parametrisation of the $gg \to H$ bins with 2-jet selection of the STXS as defined in its stage 1.2 with the parameter definitions of the SMEFTsim model. The numbers are rounded according to their statistical uncertainty. Dimensional quantities are printed in units of GeV.

Category in ggH $N_{\text{jets}}\geq 2$	**Parametrisation**
$N_{\text{jets}}\geq 2$, $m_{jj}<350$, $p_T^H<60$	$0.12c_{H\Box} - 0.033c_{HDD} + 46c_{HG} - 0.128c_{uH} + 1.63c_{uG} - 0.132c_{Hl}^{(3)} + 0.065c'_{ll}$
$N_{\text{jets}}\geq 2$, $m_{jj}<350$, $60<p_T^H<120$	$0.12c_{H\Box} - 0.033c_{HDD} + 47c_{HG} - 0.133c_{uH} + 1.59c_{uG} - 0.130c_{Hl}^{(3)} + 0.065c'_{ll}$
$N_{\text{jets}}\geq 2$, $m_{jj}<350$, $120<p_T^H<200$	$0.12c_{H\Box} - 0.032c_{HDD} + 46c_{HG} - 0.132c_{uH} + 1.48c_{uG} - 0.130c_{Hl}^{(3)} + 0.066c'_{ll}$
$N_{\text{jets}}\geq 2$, $350<m_{jj}<700$, $p_T^H<200$, $p_T^{Hjj}<25$	$0.12c_{H\Box} - 0.038c_{HDD} + 48c_{HG} - 0.16c_{uH} + 1.60c_{uG} - 0.147c_{Hl}^{(3)} + 0.075c'_{ll}$
$N_{\text{jets}}\geq 2$, $350<m_{jj}<700$, $p_T^H<200$, $p_T^{Hjj}>25$	$0.12c_{H\Box} - 0.033c_{HDD} + 42c_{HG} - 0.131c_{uH} + 1.43c_{uG} - 0.124c_{Hl}^{(3)} + 0.064c'_{ll}$
$N_{\text{jets}}\geq 2$, $m_{jj}>700$, $p_T^H<200$, $p_T^{Hjj}<25$	$0.12c_{H\Box} - 0.033c_{HDD} + 50c_{HG} - 0.14c_{uH} + 1.60c_{uG} - 0.13c_{Hl}^{(3)} + 0.068c'_{ll}$
$N_{\text{jets}}\geq 2$, $m_{jj}>700$, $p_T^H<200$, $p_T^{Hjj}>25$	$0.12c_{H\Box} - 0.030c_{HDD} + 44c_{HG} - 0.13c_{uH} + 1.4c_{uG} - 0.13c_{Hl}^{(3)} + 0.061c'_{ll}$

Table 12: Parametrisation of the $gg \to H\ell\ell$ bins of the STXS as defined in its stage 1.2 with the parameters definition of the SMEFTsim model. The numbers are rounded according to their statistical uncertainty. Dimensional quantities are printed in units of GeV.

Category in $gg \to H\ell\ell$	**Parametrisation**
$p_T^V<75$	$0.12c_{H\Box} - 0.0057c_{HDD} + 0.0090c_{HWB} + 0.0454c_{uH} + 0.309c_{uG} - 0.0102c_{Hl}^{(1)} - 0.283c_{Hl}^{(3)} - 0.0231c_{He} - 0.827c_{Hq}^{(1)} - 0.289c_{Hq}^{(3)} + 0.246c_{Hu} + 0.296c_{Hd} + 0.218c'_{ll}$
$75<p_T^V<150$	$0.12c_{H\Box} - 0.0015c_{HDD} + 0.0088c_{HWB} + 0.0542c_{uH} + 0.387c_{uG} - 0.0103c_{Hl}^{(1)} - 0.284c_{Hl}^{(3)} - 0.0235c_{He} - 0.698c_{Hq}^{(1)} - 0.250c_{Hq}^{(3)} + 0.199c_{Hu} + 0.257c_{Hd} + 0.220c'_{ll}$
$150<p_T^V<250$, $N_{\text{jets}}=0$	$0.12c_{H\Box} + 0.020c_{HDD} + 0.008c_{HWB} + 0.100c_{uH} + 0.539c_{uG} - 0.0104c_{Hl}^{(1)} - 0.287c_{Hl}^{(3)} - 0.0236c_{He} - 0.499c_{Hq}^{(1)} - 0.199c_{Hq}^{(3)} + 0.105c_{Hu} + 0.205c_{Hd} + 0.223c'_{ll}$
$150<p_T^V<250$, $\geq N_{\text{jets}}=1$	$0.12c_{H\Box} + 0.0142c_{HDD} + 0.0084c_{HWB} + 0.0851c_{uH} + 0.491c_{uG} - 0.0103c_{Hl}^{(1)} - 0.284c_{Hl}^{(3)} - 0.0233c_{He} - 0.552c_{Hq}^{(1)} - 0.212c_{Hq}^{(3)} + 0.131c_{Hu} + 0.219c_{Hd} + 0.219c'_{ll}$
$p_T^V>250$	$0.12c_{H\Box} + 0.050c_{HDD} + 0.0091c_{HWB} + 0.163c_{uH} + 0.680c_{uG} - 0.0108c_{Hl}^{(1)} - 0.286c_{Hl}^{(3)} - 0.0240c_{He} - 0.352c_{Hq}^{(1)} - 0.171c_{Hq}^{(3)} + 0.020c_{Hu} + 0.177c_{Hd} + 0.221c'_{ll}$

Table 13: Parametrisation of the $qq \to Hqq$ bins of the STXS as defined in its stage 1.2 with the parameter definitions of the SMEFTsim model. The numbers are rounded according to their statistical uncertainty. Dimensional quantities are printed in units of GeV.

Category in $qq \to Hqq$	**Parametrisation**
N_{jets}=0	$0.12c_{H\Box} - 0.011c_{HDD} + 0.32c_{HW} + 0.008c_{HB} + 0.048c_{HWB} - 0.36c_{Hl}^{(3)} + 0.46c_{Hq}^{(3)} + 0.027c_{Hu} - 0.0125c_{Hd} + 0.18c'_{ll}$
N_{jets}=1	$0.12c_{H\Box} - 0.0111c_{HDD} + 0.187c_{HW} + 0.0063c_{HB} + 0.047c_{HWB} - 0.368c_{Hl}^{(3)} + 0.003c_{Hq}^{(1)} + 0.39c_{Hq}^{(3)} + 0.0278c_{Hu} - 0.0113c_{Hd} + 0.183c'_{ll}$
$N_{\text{jets}} \geq 2 m_{jj} < 60$	$0.12c_{H\Box} - 0.011c_{HDD} + 0.38c_{HW} + 0.012c_{HB} + 0.060c_{HWB} - 0.36c_{Hl}^{(3)} + 0.94c_{Hq}^{(3)} + 0.055c_{Hu} - 0.022c_{Hd} + 0.178c'_{ll}$
$N_{\text{jets}} \geq 2 60 < m_{jj} < 120$	$0.12c_{H\Box} - 0.0072c_{HDD} + 0.638c_{HW} + 0.0230c_{HB} + 0.100c_{HWB} - 0.364c_{Hl}^{(3)} - 0.015c_{Hq}^{(1)} + 2.07c_{Hq}^{(3)} + 0.152c_{Hu} - 0.0593c_{Hd} + 0.181c'_{ll}$
$N_{\text{jets}} \geq 2 120 < m_{jj} < 350$	$0.12c_{H\Box} - 0.0099c_{HDD} - 0.021c_{HW} + 0.0017c_{HB} + 0.0368c_{HWB} - 0.363c_{Hl}^{(3)} - 0.003c_{Hq}^{(1)} - 0.155c_{Hq}^{(3)} - 0.0038c_{Hu} + 0.0022c_{Hd} + 0.181c'_{ll}$
$N_{\text{jets}} \geq 2 m_{jj} > 350, p_{\text{T}}^{H} > 200$	$0.12c_{H\Box} - 0.0072c_{HDD} + 0.188c_{HW} - 0.0012c_{HB} + 0.038c_{HWB} - 0.362c_{Hl}^{(3)} + 0.047c_{Hq}^{(1)} - 1.33c_{Hq}^{(3)} - 0.095c_{Hu} + 0.0314c_{Hd} + 0.181c'_{ll}$
$N_{\text{jets}} \geq 2 350 < m_{jj} < 700, p_{\text{T}}^{H} < 200, p_{\text{T}}^{Hjj} < 25$	$0.12c_{H\Box} - 0.0110c_{HDD} - 0.134c_{HW} - 0.0014c_{HB} + 0.0234c_{HWB} - 0.368c_{Hl}^{(3)} - 0.371c_{Hq}^{(3)} - 0.0203c_{Hu} + 0.0084c_{Hd} + 0.184c'_{ll}$
$N_{\text{jets}} \geq 2 350 < m_{jj} < 700, p_{\text{T}}^{H} < 200, p_{\text{T}}^{Hjj} > 25$	$0.12c_{H\Box} - 0.0101c_{HDD} - 0.143c_{HW} + 0.027c_{HWB} - 0.358c_{Hl}^{(3)} + 0.002c_{Hq}^{(1)} - 0.38c_{Hq}^{(3)} - 0.0204c_{Hu} + 0.0081c_{Hd} + 0.183c'_{ll}$
$N_{\text{jets}} \geq 2 m_{jj} > 700, p_{\text{T}}^{H} < 200, p_{\text{T}}^{Hjj} < 25$	$0.12c_{H\Box} - 0.0101c_{HDD} - 0.117c_{HW} - 0.0016c_{HB} + 0.0231c_{HWB} - 0.365c_{Hl}^{(3)} + 0.010c_{Hq}^{(1)} - 0.364c_{Hq}^{(3)} - 0.0216c_{Hu} + 0.0074c_{Hd} + 0.182c'_{ll}$
$N_{\text{jets}} \geq 2 m_{jj} > 700, p_{\text{T}}^{H} < 200, p_{\text{T}}^{Hjj} > 25$	$0.12c_{H\Box} - 0.0096c_{HDD} - 0.168c_{HW} + 0.023c_{HWB} - 0.361c_{Hl}^{(3)} + 0.015c_{Hq}^{(1)} - 0.442c_{Hq}^{(3)} - 0.0282c_{Hu} + 0.0091c_{Hd} + 0.180c'_{ll}$

Table 14: Parametrisation of the leptonic $qq/qg \to VH$ bins of the STXS as defined in its stage 1.2 with the parameter definitions of the SMEFTsim model. The numbers are rounded according to their statistical uncertainty. Dimensional quantities are printed in units of GeV.

Category in $qq \to H\ell\nu$	**Parametrisation**
p_T^V<75	$0.12c_{H\Box} - 0.0304c_{HDD} + 0.813c_{HW} - 0.241c^{(3)}_{Hl} + 1.142c^{(3)}_{Hq} + 0.183c'_{ll}$
75<p_T^V<150	$0.12c_{H\Box} - 0.0304c_{HDD} + 0.946c_{HW} - 0.244c^{(3)}_{Hl} + 1.90c^{(3)}_{Hq} + 0.183c'_{ll}$
150<p_T^V<250, N_{jets}=0	$0.12c_{H\Box} - 0.0312c_{HDD} + 1.06c_{HW} - 0.247c^{(3)}_{Hl} + 4.07c^{(3)}_{Hq} + 0.187c'_{ll}$
150<p_T^V<250, $N_{\text{jets}}\geq$1	$0.12c_{H\Box} - 0.0307c_{HDD} + 1.08c_{HW} - 0.239c^{(3)}_{Hl} + 3.58c^{(3)}_{Hq} + 0.180c'_{ll}$
p_T^V>250	$0.12c_{H\Box} - 0.0282c_{HDD} + 1.07c_{HW} - 0.228c^{(3)}_{Hl} + 10.6c^{(3)}_{Hq} + 0.170c'_{ll}$

Category in $qq \to H\ell\ell$	**Parametrisation**
p_T^V<75	$0.12c_{H\Box} + 0.0129c_{HDD} + 0.665c_{HW} + 0.0835c_{HB} + 0.303c_{HWB} - 0.0362c^{(1)}_{Hl} - 0.241c^{(3)}_{Hl} - 0.0359c_{He} + 0.029c^{(1)}_{Hq} + 1.27c^{(3)}_{Hq} + 0.245c_{Hu} - 0.1064c_{Hd} + 0.183c'_{ll}$
p_T^V<150	$0.12c_{H\Box} + 0.0128c_{HDD} + 0.771c_{HW} + 0.092c_{HB} + 0.341c_{HWB} - 0.0360c^{(1)}_{Hl} - 0.238c^{(3)}_{Hl} - 0.0362c_{He} + 0.01c^{(1)}_{Hq} + 1.80c^{(3)}_{Hq} + 0.403c_{Hu} - 0.166c_{Hd} + 0.182c'_{ll}$
p_T^V<250, N_{jets}=0	$0.12c_{H\Box} + 0.013c_{HDD} + 0.86c_{HW} + 0.103c_{HB} + 0.366c_{HWB} - 0.035c^{(1)}_{Hl} - 0.232c^{(3)}_{Hl} - 0.0358c_{He} - 0.12c^{(1)}_{Hq} + 3.63c^{(3)}_{Hq} + 0.87c_{Hu} - 0.323c_{Hd} + 0.177c'_{ll}$
p_T^V<250, $N_{\text{jets}}\geq$1	$0.12c_{H\Box} + 0.013c_{HDD} + 0.85c_{HW} + 0.102c_{HB} + 0.373c_{HWB} - 0.036c^{(1)}_{Hl} - 0.230c^{(3)}_{Hl} - 0.0367c_{He} - 0.10c^{(1)}_{Hq} + 3.19c^{(3)}_{Hq} + 0.77c_{Hu} - 0.282c_{Hd} + 0.177c'_{ll}$
p_T^V>250	$0.12c_{H\Box} + 0.010c_{HDD} + 0.88c_{HW} + 0.135c_{HB} + 0.41c_{HWB} - 0.037c^{(1)}_{Hl} - 0.234c^{(3)}_{Hl} - 0.036c_{He} - 1.12c^{(1)}_{Hq} + 9.9c^{(3)}_{Hq} + 2.51c_{Hu} - 0.81c_{Hd} + 0.181c'_{ll}$

Table 15: Parametrisation of the $t\bar{t}H$ and tH bins of the STXS as defined in its stage 1.2 with the parameter definitions of the SMEFTsim model. The numbers are rounded according to their statistical uncertainty. No new physics is considered in the top quark decay. Dimensional quantities are printed in units of GeV.

Category in $t\bar{t}H$ or tH	**Parametrisation**
p_{T}^{H}<60	$0.021c_{G} + 0.12c_{H\Box} - 0.0301c_{HDD} + 0.411c_{HG} - 0.121c_{uH} - 0.764c_{uG} - 0.004c_{uW} - 0.0015c_{uB} - 0.121c_{Hl}^{(3)} + 0.0031c_{Hq}^{(3)} + 0.0612c'_{ll} + 0.0154c_{qq}^{(1)} + 0.121c_{qq}^{(1)}1 + 0.0142c_{qq}^{(3)} + 0.299c_{qq}^{(31)} + 0.0088c_{uu}^{(+)}0.128c_{uu}^{(1)} - 0.0015c_{ud}^{(1)} + 0.0213c_{ud}^{(8)} + 0.0056c_{qu}^{(1)} + 0.082c_{qu}^{(8)} - 0.001c_{qd}^{(1)} + 0.0215c_{qd}^{(8)}$
60<p_{T}^{H}<120	$0.061c_{G} + 0.12c_{H\Box} - 0.0286c_{HDD} + 0.450c_{HG} - 0.1149c_{uH} - 0.790c_{uG} - 0.005c_{uW} - 0.0017c_{uB} - 0.1151c_{Hl}^{(3)} + 0.0032c_{Hq}^{(3)} + 0.0574c'_{ll} + 0.0183c_{qq}^{(1)} + 0.138c_{qq}^{(1)}1 + 0.0175c_{qq}^{(3)} + 0.340c_{qq}^{(31)} + 0.0104c_{uu}^{(+)}0.147c_{uu}^{(1)} - 0.0017c_{ud}^{(1)} + 0.0244c_{ud}^{(8)} + 0.0066c_{qu}^{(1)} + 0.0968c_{qu}^{(8)} - 0.001c_{qd}^{(1)} + 0.0243c_{qd}^{(8)}$
120<p_{T}^{H}<200	$0.152c_{G} + 0.12c_{H\Box} - 0.0282c_{HDD} + 0.553c_{HG} + 0.0013c_{HW} - 0.113c_{uH} - 0.890c_{uG} - 0.007c_{uW} - 0.002c_{uB} - 0.114c_{Hl}^{(3)} + 0.0045c_{Hq}^{(3)} + 0.0569c'_{ll} + 0.0282c_{qq}^{(1)} + 0.202c_{qq}^{(1)}1 + 0.0275c_{qq}^{(3)} + 0.493c_{qq}^{(31)} + 0.0156c_{uu}^{(+)}0.217c_{uu}^{(1)} - 0.0025c_{ud}^{(1)} + 0.0347c_{ud}^{(8)} + 0.0097c_{qu}^{(1)} + 0.138c_{qu}^{(8)} - 0.0016c_{qd}^{(1)} + 0.0345c_{qd}^{(8)}$
200<p_{T}^{H}<300	$0.311c_{G} + 0.12c_{H\Box} - 0.0277c_{HDD} + 0.68c_{HG} + 0.002c_{HW} - 0.001c_{HWB} - 0.112c_{uH} - 0.97c_{uG} - 0.0105c_{uW} - 0.003c_{uB} - 0.114c_{Hl}^{(3)} - 0.0015c_{Hq}^{(1)} + 0.0091c_{Hq}^{(3)} + 0.0569c'_{ll} + 0.0493c_{qq}^{(1)} + 0.336c_{qq}^{(1)}1 + 0.0484c_{qq}^{(3)} + 0.82c_{qq}^{(31)} + 0.0268c_{uu}^{(+)}0.358c_{uu}^{(1)} - 0.0042c_{ud}^{(1)} + 0.0545c_{ud}^{(8)} + 0.0159c_{qu}^{(1)} + 0.228c_{qu}^{(8)} - 0.0025c_{qd}^{(1)} + 0.0541c_{qd}^{(8)}$
p_{T}^{H}>300	$0.58c_{G} + 0.12c_{H\Box} - 0.0276c_{HDD} + 0.84c_{HG} + 0.003c_{HW} - 0.001c_{HWB} - 0.110c_{uH} - 1.04c_{uG} - 0.0186c_{uW} - 0.0068c_{uB} - 0.112c_{Hl}^{(3)} - 0.0105c_{Hq}^{(1)} + 0.0503c_{Hq}^{(3)} + 0.0110c_{Hu} - 0.0032c_{Hd} + 0.056c'_{ll} + 0.120c_{qq}^{(1)} + 0.75c_{qq}^{(1)}1 + 0.122c_{qq}^{(3)} + 1.70c_{qq}^{(31)} + 0.064c_{uu}^{(+)}0.78c_{uu}^{(1)} - 0.0091c_{ud}^{(1)} + 0.110c_{ud}^{(8)} + 0.0344c_{qu}^{(1)} + 0.497c_{qu}^{(8)} - 0.0045c_{qd}^{(1)} + 0.111c_{qd}^{(8)}$
tH	$0.12c_{H\Box} - 0.0272c_{HDD} + 0.254c_{HG} + 0.1808c_{HW} - 0.0764c_{uH} - 0.119c_{uG} - 0.170c_{uW} - 0.2679c_{Hl}^{(3)} + 0.319c_{Hq}^{(3)} + 0.1341c'_{ll} + 0.418c_{qq}^{(3)}$

Table 16: Interference term parametrisation of the decay widths of the considered Higgs boson decays as well as for the total Higgs boson width. Only terms with $\left(\frac{\Gamma_{\text{int}}}{\Gamma_{\text{SM}}}\right)_i > 0.001\%c_i$ are considered. Dimensional quantities are printed in units of GeV.

Channel	$\Gamma_{\text{int}}/\Gamma_{\text{SM}}$
$H \to \gamma\gamma$	$-40.15c_{HB} - 13.08c_{HW} + 22.4c_{HWB} - 0.9463c_W + 0.12c_{H\Box} - 0.2417c_{HDD} + 0.03447c_{uH} - 1.151c_{uW} - 2.150c_{uB} - 0.3637c_{Hl}^{(3)} + 0.1819c'_{ll}$
$H \to ZZ^* \to 4\ell$	$0.12c_{H\Box} + 0.005c_{HDD} - 0.296c_{HW} - 0.197c_{HB} + 0.296c_{HWB} + 0.126c_{Hl}^{(1)} - 0.234c_{Hl}^{(3)} - 0.101c_{He} + 0.181c'_{ll}$
$H \to b\bar{b}$ (VH)	$0.12c_{H\Box} - 0.030c_{HDD} - 0.121c_{dH} - 0.121c_{Hl}^{(3)} + 0.061c'_{ll}$
Total	$-0.001c_W + 0.12c_{H\Box} - 0.030c_{HDD} + 1.362c_{HG} - 0.048c_{HW} - 0.049c_{HB} + 0.046c_{HWB} - 0.005c_{eH} - 0.012c_{uH} - 0.085c_{dH} + 0.051c_{uG} - 0.002c_{uW} - 0.003c_{uB} - 0.150c_{Hl}^{(3)} + 0.013c_{Hq}^{(3)} + 0.079c'_{ll}$

Table 17: Definition of the most relevant EFT operators impacting the Higgs boson production and decay in the considered phase space together with examples of diagrams in which they play a role.

Coefficient	Operator	Example process
c_{HDD}	$\left(H^\dagger D^\mu H\right)^* \left(H^\dagger D_\mu H\right)$	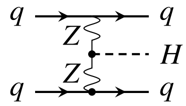
c_{HG}	$H^\dagger H\, G^A_{\mu\nu} G^{A\mu\nu}$	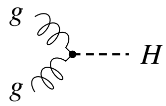
c_{HB}	$H^\dagger H\, B_{\mu\nu} B^{\mu\nu}$	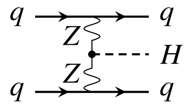
c_{HW}	$H^\dagger H\, W^I_{\mu\nu} W^{I\mu\nu}$	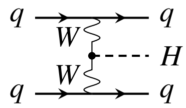
c_{HWB}	$H^\dagger \tau^I H\, W^I_{\mu\nu} B^{\mu\nu}$	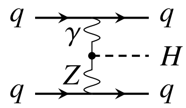
c_{eH}	$(H^\dagger H)(\bar{l}_p e_r H)$	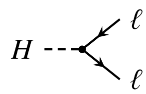
$c^{(1)}_{Hl}$	$(H^\dagger i\overleftrightarrow{D}_\mu H)(\bar{l}_p \gamma^\mu l_r)$	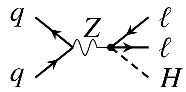
$c^{(3)}_{Hl}$	$(H^\dagger i\overleftrightarrow{D}^I_\mu H)(\bar{l}_p \tau^I \gamma^\mu l_r)$	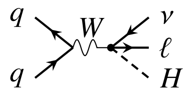
c_{He}	$(H^\dagger i\overleftrightarrow{D}_\mu H)(\bar{e}_p \gamma^\mu e_r)$	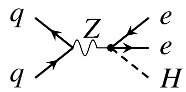
$c^{(1)}_{Hq}$	$(H^\dagger i\overleftrightarrow{D}_\mu H)(\bar{q}_p \gamma^\mu q_r)$	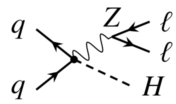
$c^{(3)}_{Hq}$	$(H^\dagger i\overleftrightarrow{D}^I_\mu H)(\bar{q}_p \tau^I \gamma^\mu q_r)$	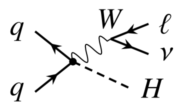
c_{Hu}	$(H^\dagger i\overleftrightarrow{D}_\mu H)(\bar{u}_p \gamma^\mu u_r)$	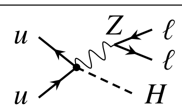
c_{Hd}	$(H^\dagger i\overleftrightarrow{D}_\mu H)(\bar{d}_p \gamma^\mu d_r)$	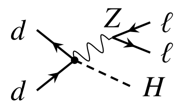

Table 18: Definition of the most relevant EFT operators impacting the Higgs boson production and decay in the considered phase space together with examples of diagrams in which they play a role.

Coefficient	Operator	Example process
c_{uG}	$(\bar{q}_p \sigma^{\mu\nu} T^A u_r) \widetilde{H}\, G^A_{\mu\nu}$	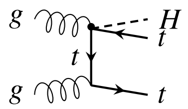
c_{uW}	$(\bar{q}_p \sigma^{\mu\nu} u_r) \tau^I \widetilde{H}\, W^I_{\mu\nu}$	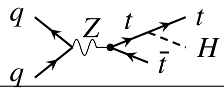
c_{uB}	$(\bar{q}_p \sigma^{\mu\nu} u_r) \widetilde{H}\, B_{\mu\nu}$	
$c^{(1)}_{qq}$	$(\bar{q}_p \gamma_\mu q_t)(\bar{q}_r \gamma^\mu q_s)$	
$c^{(3)}_{qq}$	$(\bar{q}_p \gamma_\mu \tau^I q_r)(\bar{q}_s \gamma^\mu \tau^I q_t)$	
c_{qq}	$(\bar{q}_p \gamma_\mu q_t)(\bar{q}_r \gamma^\mu q_s)$	
$c^{(31)}_{qq}$	$(\bar{q}_p \gamma_\mu \tau^I q_t)(\bar{q}_r \gamma^\mu \tau^I q_s)$	
c_{uu}	$(\bar{u}_p \gamma_\mu u_r)(\bar{u}_s \gamma^\mu u_t)$	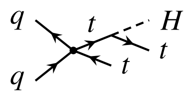
$c^{(1)}_{uu}$	$(\bar{u}_p \gamma_\mu u_t)(\bar{u}_r \gamma^\mu u_s)$	
$c^{(1)}_{qu}$	$(\bar{q}_p \gamma_\mu q_t)(\bar{u}_r \gamma^\mu u_s)$	
$c^{(8)}_{ud}$	$(\bar{u}_p \gamma_\mu T^A u_r)(\bar{d}_s \gamma^\mu T^A d_t)$	
$c^{(8)}_{qu}$	$(\bar{q}_p \gamma_\mu T^A q_r)(\bar{u}_s \gamma^\mu T^A u_t)$	
$c^{(8)}_{qd}$	$(\bar{q}_p \gamma_\mu T^A q_r)(\bar{d}_s \gamma^\mu T^A d_t)$	
c_G	$f^{ABC} G^{A\nu}_\mu G^{B\rho}_\nu G^{C\mu}_\rho$	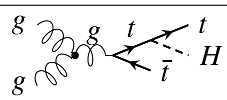

References

[1] F. Englert and R. Brout, *Broken Symmetry and the Mass of Gauge Vector Mesons*, Phys. Rev. Lett. **13** (9 1964) 321 (cit. on p. 2).

[2] P. W. Higgs, *Broken symmetries, massless particles and gauge fields*, Phys. Lett. **12** (1964) 132 (cit. on p. 2).

[3] P. W. Higgs, *Broken Symmetries and the Masses of Gauge Bosons*, Phys. Rev. Lett. **13** (16 1964) 508 (cit. on p. 2).

[4] G. S. Guralnik, C. R. Hagen and T. W. .B. Kibble, *Global conservation laws and massless particles*, Phys. Rev. Lett. **13** (1964) 585 (cit. on p. 2).

[5] P. W. Higgs, *Spontaneous symmetry breakdown without massless bosons*, Phys. Rev. **145** (1966) 1156 (cit. on p. 2).

[6] T. W. B. Kibble, *Symmetry breaking in non-Abelian gauge theories*, Phys. Rev. **155** (1967) 1554 (cit. on p. 2).

[7] ATLAS Collaboration, *Observation of a new particle in the search for the Standard Model Higgs boson with the ATLAS detector at the LHC*, Phys. Lett. B **716** (2012) 1, arXiv: 1207.7214 [hep-ex] (cit. on p. 2).

[8] CMS Collaboration, *Observation of a new boson at a mass of 125 GeV with the CMS experiment at the LHC*, Phys. Lett. B **716** (2012) 30, arXiv: 1207.7235 [hep-ex] (cit. on p. 2).

[9] ATLAS Collaboration, *A combination of measurements of Higgs boson production and decay using up to 139 fb^{-1} of proton–proton collision data at $\sqrt{s}$ = 13 TeV collected with the ATLAS experiment*, tech. rep. ATLAS-CONF-2020-027, CERN, 2020, URL: https://cds.cern.ch/record/2725733 (cit. on pp. 2, 5, 7, 8, 34).

[10] ATLAS Collaboration, *Higgs boson production cross-section measurements and their EFT interpretation in the 4ℓ decay channel at $\sqrt{s}$ = 13 TeV with the ATLAS detector*, Eur. Phys. J. C **80** (2020), arXiv: 2004.03447 [hep-ex] (cit. on pp. 2, 3, 6, 14).

[11] ATLAS Collaboration, *Measurements of WH and ZH production in the $H \to bb$ decay channel in pp collisions at 13 TeV with the ATLAS detector*, Submitted to Eur. Phys. J. C (2020), arXiv: 2007.02873 [hep-ex] (cit. on pp. 2, 3).

[12] ATLAS Collaboration, *Measurement of the associated production of a Higgs boson decaying into b-quarks with a vector boson at high transverse momentum in pp collisions at $\sqrt{s}$ = 13 TeV with the ATLAS detector*, Submitted to Phys. Lett. B (2020), arXiv: 2008.02508 [hep-ex] (cit. on p. 2).

[13] *Constraints on an effective Lagrangian from the combined $H \to ZZ^* \to 4\ell$ and $H \to \gamma\gamma$ channels using 36.1 fb^{-1} of $\sqrt{s}$ = 13 TeV pp collision data collected with the ATLAS detector*, tech. rep. ATL-PHYS-PUB-2017-018, CERN, 2017, URL: https://cds.cern.ch/record/2293084 (cit. on p. 2).

[14] ATLAS Collaboration, *Methodology for EFT interpretation of Higgs boson Simplified Template Cross-section results in ATLAS*, ATL-PHYS-PUB-2019-042, 2019, URL: https://atlas.web.cern.ch/Atlas/GROUPS/PHYSICS/PUBNOTES/ATL-PHYS-PUB-2019-042/ (cit. on pp. 2, 10).

[15] ATLAS Collaboration, *Measurement of the properties of Higgs boson production at $\sqrt{s}$ = 13 TeV in the $H \rightarrow \gamma\gamma$ channel using 139 fb^{-1} of pp collision data with the ATLAS experiment*, ATLAS-CONF-2020-026, 2020, URL: https://atlas.web.cern.ch/Atlas/GROUPS/PHYSICS/CONFNOTES/ATLAS-CONF-2020-026 (cit. on pp. 2, 3, 6).

[16] ATLAS Collaboration, *Search for Higgs bosons produced via vector-boson fusion and decaying into bottom quark pairs in $\sqrt{s}$ = 13 TeV pp collisions with the ATLAS detector*, Phys. Rev. D **98** (2018) 052003, arXiv: 1807.08639 [hep-ex] (cit. on pp. 2, 3).

[17] ATLAS Collaboration, *Search for the standard model Higgs boson produced in association with top quarks and decaying into a $b\bar{b}$ pair in pp collisions at $\sqrt{s}$ = 13 TeV with the ATLAS detector*, Phys. Rev. D **97** (2018) 072016, arXiv: 1712.08895 [hep-ex] (cit. on pp. 2, 3).

[18] ATLAS Collaboration, *Measurements of gluon-gluon fusion and vector-boson fusion Higgs boson production cross-sections in the $H \rightarrow WW^{*} \rightarrow e\nu\mu\nu$ decay channel in pp collisions at $\sqrt{s}$ = 13 TeV with the ATLAS detector*, Phys. Lett. B **789** (2019) 508, arXiv: 1808.09054 [hep-ex] (cit. on pp. 2, 3).

[19] ATLAS Collaboration, *Cross-section measurements of the Higgs boson decaying into a pair of τ-leptons in proton–proton collisions at $\sqrt{s}$ = 13 TeV with the ATLAS detector*, Phys. Rev. D **99** (2019) 072001, arXiv: 1811.08856 [hep-ex] (cit. on pp. 2, 3).

[20] ATLAS Collaboration, *Evidence for the associated production of the Higgs boson and a top quark pair with the ATLAS detector*, Phys. Rev. D **97** (2018) 072003, arXiv: 1712.08891 [hep-ex] (cit. on pp. 2, 3).

[21] ATLAS Collaboration, *Search for the dimuon decay of the Standard Model Higgs Boson with the ATLAS Detector*, Submitted to Phys. Lett. B (2020), arXiv: 2007.07830 [hep-ex] (cit. on pp. 2, 3).

[22] ATLAS Collaboration, *Combined measurements of Higgs boson production and decay using up to 80 fb^{-1} of proton–proton collision data at $\sqrt{s}$ = 13 TeV collected with the ATLAS experiment*, Phys. Rev. D **101** (2020) 012002, arXiv: 1909.02845 [hep-ex] (cit. on p. 2).

[23] A. Djouadi et al., *The post-Higgs MSSM scenario: Habemus MSSM?*, Eur. Phys. J. C **73** (2013) 2650, arXiv: 1307.5205 [hep-ph] (cit. on p. 2).

[24] E. Bagnaschi et al., *MSSM Higgs Boson Searches at the LHC: Benchmark Scenarios for Run 2 and Beyond*, Eur. Phys. J. C **79** (2019) 617, arXiv: 1808.07542 [hep-ph] (cit. on pp. 2, 31).

[25] H. Bahl, S. Liebler and T. Stefaniak, *MSSM Higgs benchmark scenarios for Run 2 and beyond: the low* $\tan\beta$ *region*, Eur. Phys. J. C **79** (2019) 279, arXiv: 1901.05933 [hep-ph] (cit. on pp. 2, 31).

[26] ATLAS Collaboration, *The ATLAS Experiment at the CERN Large Hadron Collider*, JINST **3** (2008) S08003, URL: http://stacks.iop.org/1748-0221/3/i=08/a=S08003 (cit. on p. 3).

[27] ATLAS Collaboration, *ATLAS Insertable B-Layer Technical Design Report*, ATLAS-TDR-19, 2010, URL: https://cds.cern.ch/record/1291633, *ATLAS Insertable B-Layer Technical Design Report Addendum*, ATLAS-TDR-19-ADD-1, 2012, URL: https://cds.cern.ch/record/1451888 (cit. on p. 3).

[28] B. Abbott et al., *Production and integration of the ATLAS Insertable B-Layer*, JINST **13** (2018) T05008, arXiv: 1803.00844 [physics.ins-det] (cit. on p. 3).

[29] ATLAS Collaboration, *Luminosity determination in pp collisions at $\sqrt{s}$ = 13 TeV using the ATLAS detector at the LHC*, tech. rep. ATLAS-CONF-2019-021, CERN, 2019, URL: http://cds.cern.ch/record/2677054 (cit. on p. 3).

[30] G. Avoni et al., *The new LUCID-2 detector for luminosity measurement and monitoring in ATLAS*, JINST **13** (2018) P07017 (cit. on p. 3).

[31] LHC Higgs Cross Section Working Group, D. de Florian et al., *Handbook of LHC Higgs Cross Sections: 4. Deciphering the Nature of the Higgs Sector*, (2016), arXiv: 1610.07922 [hep-ph] (cit. on pp. 3, 4, 6).

[32] P. Nason, *A new method for combining NLO QCD with shower Monte Carlo algorithms*, JHEP **11** (2004) 040, arXiv: hep-ph/0409146 [hep-ph] (cit. on p. 3).

[33] S. Frixione, P. Nason and C. Oleari, *Matching NLO QCD computations with parton shower simulations: the POWHEG method*, JHEP **11** (2007) 070, arXiv: 0709.2092 [hep-ph] (cit. on p. 3).

[34] S. Alioli, P. Nason, C. Oleari and E. Re, *A general framework for implementing NLO calculations in shower Monte Carlo programs: the POWHEG BOX*, JHEP **06** (2010) 043, arXiv: 1002.2581 [hep-ph] (cit. on p. 3).

[35] S. Alioli, P. Nason, C. Oleari and E. Re, *NLO Higgs boson production via gluon fusion matched with shower in POWHEG*, JHEP **04** (2009) 002, arXiv: 0812.0578 [hep-ph] (cit. on p. 3).

[36] K. Hamilton, P. Nason, E. Re and G. Zanderighi, *NNLOPS simulation of Higgs boson production*, JHEP **10** (2013) 222, arXiv: 1309.0017 [hep-ph] (cit. on p. 3).

[37] K. Hamilton, P. Nason and G. Zanderighi, *Finite quark-mass effects in the NNLOPS POWHEG+MiNLO Higgs generator*, JHEP **05** (2015) 140, arXiv: 1501.04637 [hep-ph] (cit. on p. 3).

[38] S. Catani and M. Grazzini, *Next-to-Next-to-Leading-Order Subtraction Formalism in Hadron Collisions and its Application to Higgs-Boson Production at the Large Hadron Collider*, Phys. Rev. Lett. **98** (2007) 222002, arXiv: hep-ph/0703012 [hep-ph] (cit. on p. 3).

[39] K. Hamilton, P. Nason, C. Oleari and G. Zanderighi, *Merging H/W/Z + 0 and 1 jet at NLO with no merging scale: a path to parton shower + NNLO matching*, JHEP **05** (2013) 082, arXiv: 1212.4504 [hep-ph] (cit. on p. 3).

[40] C. Anastasiou, C. Duhr, F. Dulat, F. Herzog and B. Mistlberger, *Higgs Boson Gluon-Fusion Production in QCD at Three Loops*, Phys. Rev. Lett. **114** (2015) 212001, arXiv: 1503.06056 [hep-ph] (cit. on p. 3).

[41] C. Anastasiou et al., *High precision determination of the gluon fusion Higgs boson cross-section at the LHC*, JHEP **05** (2016) 058, arXiv: 1602.00695 [hep-ph] (cit. on pp. 3, 32).

[42] S. Actis, G. Passarino, C. Sturm and S. Uccirati, *NLO electroweak corrections to Higgs boson production at hadron colliders*, Phys. Lett. B **670** (2008) 12, arXiv: 0809.1301 [hep-ph] (cit. on p. 3).

[43] C. Anastasiou, R. Boughezal and F. Petriello, *Mixed QCD-electroweak corrections to Higgs boson production in gluon fusion*, JHEP **04** (2009) 003, arXiv: 0811.3458 [hep-ph] (cit. on p. 3).

[44] M. Grazzini and H. Sargsyan, *Heavy-quark mass effects in Higgs boson production at the LHC*, JHEP **09** (2013) 129, arXiv: 1306.4581 [hep-ph] (cit. on p. 4).

[45] P. Nason and C. Oleari, *NLO Higgs boson production via vector-boson fusion matched with shower in POWHEG*, JHEP **02** (2010) 037, arXiv: 0911.5299 [hep-ph] (cit. on p. 4).

[46] K. Hamilton, P. Nason and G. Zanderighi, *MINLO: multi-scale improved NLO*, JHEP **10** (2012) 155, arXiv: 1206.3572 [hep-ph] (cit. on p. 4).

[47] M. Ciccolini, A. Denner and S. Dittmaier, *Strong and Electroweak Corrections to the Production of a Higgs Boson + 2 Jets via Weak Interactions at the Large Hadron Collider*, Phys. Rev. Lett. **99** (2007) 161803, arXiv: 0707.0381 [hep-ph] (cit. on p. 4).

[48] M. Ciccolini, A. Denner and S. Dittmaier, *Electroweak and QCD corrections to Higgs production via vector-boson fusion at the LHC*, Phys. Rev. D **77** (2008) 013002, arXiv: 0710.4749 [hep-ph] (cit. on p. 4).

[49] P. Bolzoni, F. Maltoni, S.-O. Moch and M. Zaro, *Higgs Boson Production via Vector-Boson Fusion at Next-to-Next-to-Leading Order in QCD*, Phys. Rev. Lett. **105** (2010) 011801, arXiv: 1003.4451 [hep-ph] (cit. on p. 4).

[50] O. Brein, A. Djouadi and R. Harlander, *NNLO QCD corrections to the Higgs-strahlung processes at hadron colliders*, Phys. Lett. B **579** (2004) 149, arXiv: hep-ph/0307206 [hep-ph] (cit. on p. 4).

[51] A. Denner, S. Dittmaier, S. Kallweit and A. Mück, *Electroweak corrections to Higgs-strahlung off W/Z bosons at the Tevatron and the LHC with HAWK*, JHEP **03** (2012) 075, arXiv: 1112.5142 [hep-ph] (cit. on p. 4).

[52] L. Altenkamp, S. Dittmaier, R. V. Harlander, H. Rzehak and T. J. E. Zirke, *Gluon-induced Higgs-strahlung at next-to-leading order QCD*, JHEP **02** (2013) 078, arXiv: 1211.5015 [hep-ph] (cit. on p. 4).

[53] J. Alwall et al., *The automated computation of tree-level and next-to-leading order differential cross sections, and their matching to parton shower simulations*, JHEP **07** (2014) 079, arXiv: 1405.0301 [hep-ph] (cit. on pp. 4, 10).

[54] W. Beenakker et al., *NLO QCD corrections to $t\bar{t}H$ production in hadron collisions*, Nucl. Phys. B **653** (2003) 151, arXiv: hep-ph/0211352 [hep-ph] (cit. on p. 4).

[55] S. Dawson, C. Jackson, L. Orr, L. Reina and D. Wackeroth, *Associated Higgs production with top quarks at the large hadron collider: NLO QCD corrections*, Phys. Rev. D **68** (2003) 034022, arXiv: hep-ph/0305087 [hep-ph] (cit. on p. 4).

[56] Y. Zhang, W.-G. Ma, R.-Y. Zhang, C. Chen and L. Guo, *QCD NLO and EW NLO corrections to $t\bar{t}H$ production with top quark decays at hadron collider*, Phys. Lett. B **738** (2014) 1, arXiv: 1407.1110 [hep-ph] (cit. on p. 4).

[57] S. Frixione, V. Hirschi, D. Pagani, H. S. Shao and M. Zaro, *Weak corrections to Higgs hadroproduction in association with a top-quark pair*, JHEP **09** (2014) 065, arXiv: 1407.0823 [hep-ph] (cit. on p. 4).

[58] M. Wiesemann et al., *Higgs production in association with bottom quarks*, JHEP **02** (2015) 132, arXiv: 1409.5301 [hep-ph] (cit. on p. 4).

[59] S. Dawson, C. Jackson, L. Reina and D. Wackeroth, *Exclusive Higgs boson production with bottom quarks at hadron colliders*, Phys. Rev. D **69** (7 2004) 074027, arXiv: hep-ph/0311067 [hep-ph] (cit. on pp. 4, 32).

[60] S. Dittmaier, M. Krämer and M. Spira, *Higgs radiation off bottom quarks at the Tevatron and the CERN LHC*, Phys. Rev. D **70** (7 2004) 074010, arXiv: hep-ph/0309204 [hep-ph] (cit. on pp. 4, 32).

[61] R. V. Harlander and W. B. Kilgore, *Higgs boson production in bottom quark fusion at next-to-next-to leading order*, Phys. Rev. D **68** (1 2003) 013001, arXiv: hep-ph/0304035 [hep-ph] (cit. on pp. 4, 32).

[62] H.-L. Lai et al., *New parton distributions for collider physics*, Phys. Rev. D **82** (2010) 074024, arXiv: 1007.2241 [hep-ph] (cit. on p. 4).

[63] F. Demartin, F. Maltoni, K. Mawatari and M. Zaro, *Higgs production in association with a single top quark at the LHC*, Eur. Phys. J. C **75** (2015) 267, arXiv: 1504.00611 [hep-ph] (cit. on p. 4).

[64] T. Sjöstrand, S. Mrenna and P. Z. Skands, *A brief introduction to PYTHIA 8.1*, Comput. Phys. Commun. **178** (2008) 852, arXiv: 0710.3820 [hep-ph] (cit. on pp. 4, 11).

[65] ATLAS Collaboration, *Measurement of the Z/γ^* boson transverse momentum distribution in pp collisions at $\sqrt{s} = 7$ TeV with the ATLAS detector*, JHEP **09** (2014) 145, arXiv: 1406.3660 [hep-ex] (cit. on p. 4).

[66] S. Agostinelli et al., *Geant4 – a simulation toolkit*, Nucl. Instrum. Meth. A **506** (2003) 250 (cit. on p. 4).

[67] ATLAS Collaboration, *The ATLAS Simulation Infrastructure*, Eur. Phys. J. C **70** (2010) 823, arXiv: 1005.4568 [physics.ins-det] (cit. on p. 4).

[68] A. Martin, W. Stirling, R. Thorne and G. Watt, *Parton distributions for the LHC*, Eur. Phys. J. C **63** (2009) 189, arXiv: 0901.0002 [hep-ph] (cit. on p. 4).

[69] ATLAS Collaboration, *Summary of ATLAS Pythia 8 tunes*, ATL-PHYS-PUB-2012-003, 2012, URL: https://cds.cern.ch/record/1474107 (cit. on p. 4).

[70] ATLAS Collaboration, *The Pythia 8 A3 tune description of ATLAS minimum bias and inelastic measurements incorporating the Donnachie–Landshoff diffractive model*, ATL-PHYS-PUB-2016-017, 2016, URL: https://cds.cern.ch/record/2206965 (cit. on p. 4).

[71] J. R. Andersen et al., *Les Houches 2015: Physics at TeV Colliders Standard Model Working Group Report*, (2016), arXiv: 1605.04692 [hep-ph] (cit. on p. 6).

[72] N. Berger et al., *Simplified Template Cross Sections - Stage 1.1*, (2019), arXiv: 1906.02754 [hep-ph] (cit. on p. 6).

[73] S. Amoroso et al., 'Les Houches 2019: Physics at TeV Colliders: Standard Model Working Group Report', *11th Les Houches Workshop on Physics at TeV Colliders: PhysTeV Les Houches*, 2020, arXiv: 2003.01700 [hep-ph] (cit. on p. 6).

[74] ATLAS Collaboration, *Evaluation of theoretical uncertainties for simplified template cross section measurements of V-associated production of the Higgs boson*, ATL-PHYS-PUB-2018-035, 2018, URL: https://cds.cern.ch/record/2649241 (cit. on p. 6).

[75] B. Grzadkowski, M. Iskrzynski, M. Misiak and J. Rosiek, *Dimension-Six Terms in the Standard Model Lagrangian*, JHEP **10** (2010) 085, arXiv: 1008.4884 [hep-ph] (cit. on p. 10).

[76] I. Brivio and M. Trott, *The Standard Model as an Effective Field Theory*, Phys. Rept. **793** (2019) 1, arXiv: 1706.08945 [hep-ph] (cit. on p. 10).

[77] I. Brivio, Y. Jiang and M. Trott, *The SMEFTsim package, theory and tools*, JHEP **12** (2017) 070, arXiv: 1709.06492 [hep-ph] (cit. on p. 10).

[78] C. Degrande et al., *Standard Model Effective Theory at Next-to-Leading-Order in QCD*, URL: http://feynrules.irmp.ucl.ac.be/wiki/SMEFTatNLO (cit. on p. 10).

[79] S. Dawson and P. P. Giardino, *Electroweak corrections to Higgs boson decays to $\gamma\gamma$ and W^+W^- in standard model EFT*, Phys. Rev. D **98** (2018) 095005, arXiv: 1807.11504 [hep-ph] (cit. on p. 10).

[80] M. L. Mangano, M. Moretti, F. Piccinini and M. Treccani, *Matching matrix elements and shower evolution for top-pair production in hadronic collisions*, Journal of High Energy Physics **2007** (2007) 013 (cit. on p. 11).

[81] S. Mrenna and P. Richardson, *Matching matrix elements and parton showers with HERWIG and PYTHIA*, JHEP **05** (2004) 040, arXiv: hep-ph/0312274 (cit. on p. 11).

[82] A. Buckley et al., *Rivet user manual*, Comput. Phys. Commun. **184** (2013) 2803, arXiv: 1003.0694 [hep-ph] (cit. on p. 11).

[83] LHC Higgs XS WG, URL: https://gitlab.cern.ch/LHCHIGGSXS/LHCHXSWG2/STXS/Classification (cit. on p. 11).

[84] C. Degrande, B. Fuks, K. Mawatari, K. Mimasu and V. Sanz, *Electroweak Higgs boson production in the standard model effective field theory beyond leading order in QCD*, Eur. Phys. J. **C77** (2017) 262, arXiv: 1609.04833 [hep-ph] (cit. on p. 12).

[85] H. Miyazawa, *Baryon Number Changing Currents*, Prog. Theor. Phys. **36 (6)** (1966) 1266 (cit. on p. 31).

[86] P. Ramond, *Dual Theory for Free Fermions*, Phys. Rev. D **3** (1971) 2415 (cit. on p. 31).

[87] Y. A. Gol'fand and E. P. Likhtman, *Extension of the Algebra of Poincare Group Generators and Violation of p Invariance*, JETP Lett. **13** (1971) 323, [Pisma Zh.Eksp.Teor.Fiz.13:452-455,1971] (cit. on p. 31).

[88] A. Neveu and J. H. Schwarz, *Factorizable dual model of pions*, Nucl. Phys. B **31** (1971) 86 (cit. on p. 31).

[89] A. Neveu and J. H. Schwarz, *Quark Model of Dual Pions*, Phys. Rev. D **4** (1971) 1109 (cit. on p. 31).

[90] J. Gervais and B. Sakita, *Field theory interpretation of supergauges in dual models*, Nucl. Phys. B **34** (1971) 632 (cit. on p. 31).

[91] D. V. Volkov and V. P. Akulov, *Is the Neutrino a Goldstone Particle?*, Phys. Lett. B **46** (1973) 109 (cit. on p. 31).

[92] J. Wess and B. Zumino, *A Lagrangian Model Invariant Under Supergauge Transformations*, Phys. Lett. B **49** (1974) 52 (cit. on p. 31).

[93] J. Wess and B. Zumino, *Supergauge Transformations in Four-Dimensions*, Nucl. Phys. B **70** (1974) 39 (cit. on p. 31).

[94] S. Weinberg, *Implications of dynamical symmetry breaking*, Phys. Rev. D **13** (1976) 974 (cit. on p. 31).

[95] E. Gildener, *Gauge-symmetry hierarchies*, Phys. Rev. D **14** (1976) 1667 (cit. on p. 31).

[96] S. Weinberg, *Implications of dynamical symmetry breaking: An addendum*, Phys. Rev. D **19** (1979) 1277 (cit. on p. 31).

[97] L. Susskind, *Dynamics of spontaneous symmetry breaking in the Weinberg-Salam theory*, Phys. Rev. D **20** (1979) 2619 (cit. on p. 31).

[98] H. Goldberg, *Constraint on the Photino Mass from Cosmology*, Phys. Rev. Lett. **50** (1983) 1419 (cit. on p. 31).

[99] J. Ellis, J. Hagelin, D. Nanopoulos, K. Olive and M. Srednicki, *Supersymmetric relics from the big bang*, Nuclear Physics B **238** (1984) 453 (cit. on p. 31).

[100] S. Dimopoulos, S. Raby and F. Wilczek, *Supersymmetry and the scale of unification*, Phys. Rev. D **24** (1981) 1681 (cit. on p. 31).

[101] N. Sakai, *Naturalnes in supersymmetric GUTS*, Zeitschrift für Physik C Particles and Fields **11** (1981) 153 (cit. on p. 31).

[102] L. Ibáñez and G. Ross, *Low-energy predictions in supersymmetric grand unified theories*, Phys. Lett. B **105** (1981) 439 (cit. on p. 31).

[103] M. Einhorn and D. Jones, *The weak mixing angle and unification mass in supersymmetric SU(5)*, Nuclear Physics B **196** (1982) 475 (cit. on p. 31).

[104] W. J. Marciano and G. Senjanović, *Predictions of supersymmetric grand unified theories*, Phys. Rev. D **25** (1982) 3092 (cit. on p. 31).

[105] C. Giunti, C. W. Kim and U. W. Lee, *Running coupling constants and grand unification models*, Modern Physics Letters A **06** (1991) 1745 (cit. on p. 31).

[106] J. Ellis, S. Kelley and D. Nanopoulos, *Probing the desert using gauge coupling unification*, Phys. Lett. B **260** (1991) 131 (cit. on p. 31).

[107] U. Amaldi, W. de Boer and H. Fürstenau, *Comparison of grand unified theories with electroweak and strong coupling constants measured at LEP*, Phys. Lett. B **260** (1991) 447 (cit. on p. 31).

[108] P. Langacker and M. Luo, *Implications of precision electroweak experiments for m_t, ρ_0, $sin^2\theta W$, and grand unification*, Phys. Rev. D **44** (1991) 817 (cit. on p. 31).

[109] P. Fayet, *Supersymmetry and Weak, Electromagnetic and Strong Interactions*, Phys. Lett. B **64** (1976) 159 (cit. on p. 31).

[110] P. Fayet, *Spontaneously Broken Supersymmetric Theories of Weak, Electromagnetic and Strong Interactions*, Phys. Lett. B **69** (1977) 489 (cit. on p. 31).

[111] G. R. Farrar and P. Fayet, *Phenomenology of the Production, Decay, and Detection of New Hadronic States Associated with Supersymmetry*, Phys. Lett. B **76** (1978) 575 (cit. on p. 31).

[112] P. Fayet, *Relations Between the Masses of the Superpartners of Leptons and Quarks, the Goldstino Couplings and the Neutral Currents*, Phys. Lett. B **84** (1979) 416 (cit. on p. 31).

[113] S. Dimopoulos and H. Georgi, *Softly Broken Supersymmetry and SU(5)*, Nucl. Phys. B **193** (1981) 150 (cit. on p. 31).

[114] S. Heinemeyer, W. Hollik and G. Weiglein, *FeynHiggs: A Program for the calculation of the masses of the neutral CP even Higgs bosons in the MSSM*, Comput.Phys.Commun. **124** (2000) 76, arXiv: `hep-ph/9812320 [hep-ph]` (cit. on p. 32).

[115] S. Heinemeyer, W. Hollik and G. Weiglein, *The Masses of the neutral CP-even Higgs bosons in the MSSM: Accurate analysis at the two loop level*, Eur. Phys. J. C **9** (1999) 343, arXiv: `hep-ph/9812472 [hep-ph]` (cit. on p. 32).

[116] G. Degrassi, S. Heinemeyer, W. Hollik, P. Slavich and G. Weiglein, *Towards high precision predictions for the MSSM Higgs sector*, Eur. Phys. J. C **28** (2003) 133, arXiv: `hep-ph/0212020 [hep-ph]` (cit. on pp. 32, 33).

[117] M. Frank et al., *The Higgs boson masses and mixings of the complex MSSM in the Feynman-diagrammatic approach*, Journal of High Energy Physics **2007** (2007) 047 (cit. on p. 32).

[118] T. Hahn, S. Heinemeyer, W. Hollik, H. Rzehak and G. Weiglein, *High-Precision Predictions for the LightCP-Even Higgs Boson Mass of the Minimal Supersymmetric Standard Model*, Phys. Rev. Lett. **112** (2014) (cit. on p. 32).

[119] H. Bahl and W. Hollik, *Precise prediction for the light MSSM Higgs boson mass combining effective field theory and fixed-order calculations*, Eur. Phys. J. C **76** (2016) 499, arXiv: 1608.01880 [hep-ph] (cit. on p. 32).

[120] H. Bahl, S. Heinemeyer, W. Hollik and G. Weiglein, *Reconciling EFT and hybrid calculations of the light MSSM Higgs-boson mass*, Eur. Phys. J. C **78** (2018) 57, arXiv: 1706.00346 [hep-ph] (cit. on p. 32).

[121] A. Djouadi, J. Kalinowski and M. Spira, *HDECAY: A Program for Higgs boson decays in the Standard Model and its supersymmetric extension*, Comput. Phys. Commun. **108** (1998) 56, arXiv: hep-ph/9704448 [hep-ph] (cit. on p. 32).

[122] A. Djouadi, J. Kalinowski, M. Muehlleitner and M. Spira, *HDECAY: Twenty$_{++}$ years after*, Comput. Phys. Commun. **238** (2019) 214, arXiv: 1801.09506 [hep-ph] (cit. on p. 32).

[123] A. Bredenstein, A. Denner, S. Dittmaier and M. Weber, *Precise predictions for the Higgs-boson decay $H \to WW/ZZ \to 4$ leptons*, Phys. Rev. D **74** (2006) 013004, arXiv: hep-ph/0604011 [hep-ph] (cit. on p. 32).

[124] A. Bredenstein, A. Denner, S. Dittmaier and M. Weber, *Radiative corrections to the semileptonic and hadronic Higgs-boson decays $H \to WW/ZZ \to 4$ fermions*, JHEP **02** (2007) 080, arXiv: hep-ph/0611234 [hep-ph] (cit. on p. 32).

[125] R. V. Harlander, S. Liebler and H. Mantler, *SusHi: A program for the calculation of Higgs production in gluon fusion and bottom-quark annihilation in the Standard Model and the MSSM*, Comput. Phys. Commun. **184** (2013) 1605, arXiv: 1212.3249 [hep-ph] (cit. on p. 32).

[126] R. V. Harlander, S. Liebler and H. Mantler, *SusHi Bento: Beyond NNLO and the heavy-top limit*, Comput. Phys. Commun. **212** (2017) 239, arXiv: 1605.03190 [hep-ph] (cit. on p. 32).

[127] M. Spira, A. Djouadi, D. Graudenz and P. Zerwas, *Higgs boson production at the LHC*, Nucl. Phys. B **453** (1995) 17, arXiv: hep-ph/9504378 (cit. on p. 32).

[128] R. V. Harlander and W. B. Kilgore, *Next-to-next-to-leading order Higgs production at hadron colliders*, Phys. Rev. Lett. **88** (20 2002) 201801, arXiv: hep-ph/0201206 (cit. on p. 32).

[129] C. Anastasiou and K. Melnikov, *Higgs boson production at hadron colliders in NNLO QCD*, Nucl. Phys. B **646** (2002) 220, arXiv: hep-ph/0207004 (cit. on p. 32).

[130] V. Ravindran, J. Smith and W. L. van Neerven, *NNLO corrections to the total cross-section for Higgs boson production in hadron hadron collisions*, Nucl. Phys. B **665** (2003) 325, arXiv: hep-ph/0302135 (cit. on p. 32).

[131] R. V. Harlander and W. B. Kilgore, *Production of a pseudoscalar Higgs boson at hadron colliders at next-to-next-to leading order*, JHEP **10** (2002) 017, arXiv: hep-ph/0208096 [hep-ph] (cit. on p. 32).

[132] C. Anastasiou and K. Melnikov, *Pseudoscalar Higgs boson production at hadron colliders in NNLO QCD*, Phys. Rev. D **67** (2003) 037501, arXiv: hep-ph/0208115 [hep-ph] (cit. on p. 32).

[133] U. Aglietti, R. Bonciani, G. Degrassi and A. Vicini, *Two loop light fermion contribution to Higgs production and decays*, Phys. Lett. B **595** (2004) 432, arXiv: hep-ph/0404071 (cit. on p. 32).

[134] R. Bonciani, G. Degrassi and A. Vicini, *On the generalized harmonic polylogarithms of one complex variable*, Computer Physics Communications **182** (2011) 1253 (cit. on p. 32).

[135] C. Anastasiou et al., *Higgs Boson Gluon Fusion Production Beyond Threshold in N^3LO QCD*, JHEP **03** (2015) 091, arXiv: 1411.3584 [hep-ph] (cit. on p. 32).

[136] C. Anastasiou et al., *Soft expansion of double-real-virtual corrections to Higgs production at N^3LO*, JHEP **08** (2015) 051, arXiv: 1505.04110 [hep-ph] (cit. on p. 32).

[137] M. Bonvini, A. S. Papanastasiou and F. J. Tackmann, *Resummation and matching of b-quark mass effects in $b\bar{b}H$ production*, JHEP **11** (2015) 196, arXiv: 1508.03288 [hep-ph] (cit. on p. 32).

[138] M. Bonvini, A. S. Papanastasiou and F. J. Tackmann, *Matched predictions for the $b\bar{b}H$ cross section at the 13 TeV LHC*, JHEP **10** (2016) 053, arXiv: 1605.01733 [hep-ph] (cit. on p. 32).

[139] S. Forte, D. Napoletano and M. Ubiali, *Higgs production in bottom-quark fusion in a matched scheme*, Phys. Lett. B **751** (2015) 331, arXiv: 1508.01529 [hep-ph] (cit. on p. 32).

[140] S. Forte, D. Napoletano and M. Ubiali, *Higgs production in bottom-quark fusion: matching beyond leading order*, Phys. Lett. B **763** (2016) 190, arXiv: 1607.00389 [hep-ph] (cit. on p. 32).

[141] LHC Higgs XS WG for BSM Higgs, *MSSM Neutral Higgs LHCXSWG3 Twiki page*, tech. rep., URL: https://twiki.cern.ch/twiki/bin/view/LHCPhysics/LHCHXSWGMSSMNeutral (cit. on p. 33).

[142] B. Allanach, A. Djouadi, J. Kneur, W. Porod and P. Slavich, *Precise determination of the neutral Higgs boson masses in the MSSM*, Journal of High Energy Physics **2004** (2004) 044, ISSN: 1029-8479, URL: http://dx.doi.org/10.1088/1126-6708/2004/09/044 (cit. on p. 33).

[143] ATLAS Collaboration, *Search for Heavy Higgs Bosons Decaying into Two Tau Leptons with the ATLAS Detector Using pp Collisions at $\sqrt{s} = 13$ TeV*, Phys. Rev. Lett. **125** (2020) 051801, arXiv: 2002.12223 [hep-ex] (cit. on pp. 34, 35).

[144] ATLAS Collaboration, *Search for charged Higgs bosons decaying into a top-quark and a bottom-quark at $\sqrt{s}$ = 13 TeV with the ATLAS detector*, tech. rep. ATLAS-CONF-2020-039, CERN, 2020, URL: https://cds.cern.ch/record/2727860 (cit. on pp. 34, 35).